

SOLDER JOINT RELIABILITY IN ELECTRONICS UNDER SHOCK AND
VIBRATION USING EXPLICIT FINITE-ELEMENT SUB-MODELING

Except where reference is made to the work of others, the work described in this thesis is my own work or was done in collaboration with my advisory committee. This thesis does not include proprietary or classified information.

Sameep Gupte

Certificate of Approval:

Robert L. Jackson
Assistant Professor
Mechanical Engineering

Pradeep Lall, Chair
Thomas Walter Professor
Mechanical Engineering

George Flowers
Alumni Professor
Mechanical Engineering

Joe F. Pittman
Interim Dean
Graduate School

SOLDER JOINT RELIABILITY IN ELECTRONICS UNDER SHOCK AND
VIBRATION USING EXPLICIT FINITE-ELEMENT SUB-MODELING

Sameep Gupte

A Thesis

Submitted to

the Graduate Faculty of

Auburn University

in Partial Fulfillment of the

Requirements for the

Degree of

Master of Science

Auburn, Alabama
May 10, 2007

SOLDER JOINT RELIABILITY IN ELECTRONICS UNDER SHOCK AND
VIBRATION USING EXPLICIT FINITE-ELEMENT SUB-MODELING

Sameep Gupte

Permission is granted to Auburn University to make copies of this thesis at its discretion, upon the request of individuals or institutions at their expense. The author reserves all publication rights.

Signature of Author

Date of Graduation

THESIS ABSTRACT

SOLDER JOINT RELIABILITY IN ELECTRONICS UNDER SHOCK AND
VIBRATION USING EXPLICIT FINITE-ELEMENT SUB-MODELING

Sameep Gupte

Master of Science, May 10, 2007
(B.E., Mumbai University, 2003)

151 Typed Pages

Directed by Pradeep Lall

Solder joint failure in electronic devices subject to shock and drop environment is one of the key concerns for the telecommunications industry. The recent trend towards miniaturization and increased functional density has resulted in decreasing the I/O pitch, and thus increasing the chances of failure of the package under shock and vibration environments. Solder joint failure occurs due to a combination of printed circuit board (PCB) bending and mechanical shock during impact. Consequently, optimization of package design is necessary to minimize the effects of shock during impact on the solder interconnections.

In this present work, the modeling approaches for first-level solder interconnects in shock and drop of electronics assemblies have been developed without any assumptions of geometric or loading symmetry. The problem involves multiple scales

from the macro-scale transient-dynamics of electronic assembly to the micro-structural damage history of interconnects. Previous modeling approaches include, solid-to-solid sub-modeling [Zhu, et. al. 2001] using a half test PCB board and shell-to-solid sub-modeling technique using a quarter symmetry model [Ren, et. al. 2003, 2004]. Inclusion of model symmetry saves computational time but targets primarily symmetric mode shapes. The modeling approach proposed in this paper enables prediction of both symmetric and anti-symmetric modes. Approaches investigated include, smeared property models, Timoshenko-beam element models, explicit sub-models, and continuum-shell models. Transient dynamic behavior of the board assemblies in free and JEDEC drop has been measured using high-speed strain and displacement measurements. Model predictions have been correlated with experimental data. Two failure prediction models namely the Timoshenko-Beam Failure Model and the Cohesive Zone Failure Model have also been developed to predict the location and mode of failure in the solder interconnections in PCB assemblies subject to drop impact.

ACKNOWLEDGEMENTS

I would like to thank my advisor, Dr. Pradeep Lall, for his guidance, patience and constant encouragement. Completion of the thesis would not have been possible without his help. I would also like to acknowledge and thank the National Science Foundation for their financial support. I also wish to extend my gratitude to Dr. George Flowers and Dr. Robert Jackson for serving on my thesis committee and examining my thesis.

I would also like to thank all my friends and colleagues for their support and understanding. Finally, many thanks go to Sanket, Pradnya and my parents for their unwavering encouragement and love.

Style manual or journal used Graduate School: Guide to Preparation and Submission of Theses and Dissertations

Computer software used Microsoft Office 2003, Ansys 9.0, Altair Hyperworks 7.0, Abaqus 6.6

TABLE OF CONTENTS

LIST OF FIGURES	x
LIST OF TABLES	xv
CHAPTER 1 INTRODUCTION	1
CHAPTER 2 LITERATURE REVIEW	5
2.1 Experimental Techniques	5
2.2 Finite Element Simulations	10
CHAPTER 3 MODELING METHODOLOGY FOR DROP SIMULATIONS	18
3.1 Overview	18
3.2 Drop Simulation Methodology	27
3.3 Choice of Time Integration Formulation	29
3.4 Element Formulations and Characteristics	34
CHAPTER 4 FINITE ELEMENT MODELS FOR DROP SIMULATION	41
4.1 Smearred Property Global Model	41
4.2 Conventional Shell-Beam Model	50
4.3 Continuum Shell-Beam Model	57
4.4 Correlation of Predicted Peak Relative Displacement and Strain Histories	65
4.5 Error estimation in incorporating symmetry based models	70

4.6	Solder Interconnect Strain Histories in the Global Model	70
4.7	Explicit Sub-model for Drop Simulation	72
4.8	Solder Interconnect Strain Histories in the Local Model	76
4.9	Susceptibility to Chip Fracture	87
CHAPTER 5 FAILURE PREDICTION MODELS		89
5.1	Overview	89
5.2	Timoshenko-Beam Failure Model	90
5.3	Cohesive Zone Failure Model	92
5.4	Modeling Approach and Modeling Correlations	103
CHAPTER 6 SUMMARY AND CONCLUSIONS		121
BIBLIOGRAPHY		123

LIST OF FIGURES

Figure 1 State of the art modeling techniques.	11
Figure 2 Modeling Methodology.	19
Figure 3 Interconnect array configuration for 95.5Sn4.0Ag0.5Cu and 63Sn37Pb Test Vehicles.	22
Figure 4 TABGA Test Board.	22
Figure 5 PCB assembly subject to 90-degree free vertical drop.	24
Figure 6 PCB assembly subject to 0-degree JEDEC drop.	24
Figure 7 Measurement of initial angle prior to impact.	25
Figure 8 Test board with target points to measure relative displacement.	25
Figure 9 High speed image analysis to capture displacement and velocity.	26
Figure 10 Transient-strain and continuity for determination of component failure.	26
Figure 11 90-degree free vertical drop.	28
Figure 12 Zero-degree horizontal JEDEC Drop.	28
Figure 13 Various element formulations employed to create the explicit models.	40
Figure 14 Typical architecture for TABGA package.	42
Figure 15 Schematic of 90-degree free vertical drop.	43
Figure 16 Schematic of Zero-Degree JEDEC Drop.	43
Figure 17 PCB modeled using shell (S4R) elements and CSP using smeared properties.	46

Figure 18 Correlation of Transient Mode-Shapes for Smeared Element Model during Free Vertical Drop.	51
Figure 19 Correlation of transient mode-shapes for Smeared Element Model during JEDEC Drop.	52
Figure 20 Solder interconnection layout modeled using Timoshenko Beam elements.	54
Figure 21 Printed-Circuit assembly with Timoshenko-Beam Element interconnects and Conventional Shell-Elements.	54
Figure 22 Correlation of transient mode-shapes for Conventional-Shell Timoshenko-Beam Model during free vertical drop.	58
Figure 23 Correlation of transient mode-shapes for Conventional-Shell Timoshenko-Beam Model during JEDEC Drop.	59
Figure 24 Solder interconnection layout modeled using Timoshenko Beam elements.	62
Figure 25 Printed-Circuit assembly with Timoshenko-Beam Element interconnects and Continuum Shell-Elements.	62
Figure 26 Correlation of transient mode-shapes for Continuum-Shell Timoshenko-Beam Model during free vertical drop.	63
Figure 27 Correlation of transient mode-shapes for Continuum-Shell Timoshenko-Beam Model during JEDEC Drop.	64
Figure 28 Correlation between experimental relative displacement of board assembly at 2.4 ms with model predictions under zero-degree JEDEC drop-test.	69
Figure 29 Correlation between experimental relative displacement of board assembly at 4.5 ms with Model Predictions under 90 ⁰ free drop-test.	69

Figure 30 Stress distribution in the Timoshenko-Beam solder interconnects subject to JEDEC drop for the Conventional Shell-Beam Model.	71
Figure 31 Representation of solder interconnection array.	73
Figure 32 Timoshenko-Beam Element with Conventional-Shell Model prediction of transient strain history at the package corner solder interconnects during 0° JEDEC-Drop.	74
Figure 33 Timoshenko-Beam Element with Conventional-Shell Model Prediction of transient strain history in the solder interconnects located in the die shadow region during 0° JEDEC-Drop.	74
Figure 34 Solder interconnection layout in Explicit Sub-model with a combination hexahedral-element corner interconnects and Timoshenko-Beam Element interconnects.	77
Figure 35 Local Explicit Sub-Model with hexahedral-element corner interconnects, Timoshenko-Beam Element interconnects and PCB meshed with hexahedral reduced integration-elements.	78
Figure 36 Strain histories in the local model corresponding to Conventional Shell Timoshenko-beam global model during JEDEC-drop at various time intervals.	80
Figure 37 Strain histories in the local model corresponding to Conventional Shell Timoshenko-beam global model during free vertical drop at various time intervals.	81

Figure 38 Global-Local explicit Sub-Model predictions of transient logarithmic shear strain, LE12, in the solder interconnect of one of the chip-scale packages on the printed circuit board assembly during JEDEC Drop.	82
Figure 39 Global-Local Explicit Sub-Model predictions of transient logarithmic shear strain, LE23, in the solder interconnect of one of the chip-scale packages on the printed circuit board assembly during JEDEC Drop.	83
Figure 40 Global-Local Explicit Sub-Model predictions of transient logarithmic shear strain, LE12, in the solder interconnect of one of the chip-scale packages on the printed circuit board assembly during Free Drop.	84
Figure 41 Global-Local Explicit Sub-Model predictions of transient logarithmic shear strain, LE23, in the solder interconnect of one of the chip-scale packages on the printed circuit board assembly during Free Drop.	85
Figure 42 Cross-section of corner solder interconnect in the failed samples showing higher susceptibility of the samples to fail at the package-to-solder interconnect interface or the solder-to-printed circuit board interface.	86
Figure 43 Transient stress history in the silicon chip.	88
Figure 44 Transient stress history in chip top and bottom surfaces.	88
Figure 45 Brittle interfacial failure observed in the solder interconnections at the package side and the PCB side.	89
Figure 46 Solder joint array tensile test configuration [Darveaux et al. 2006].	91
Figure 47 Stress-Strain response of solder ball sample subject to tensile loading at various strain rates [Darveaux et al. 2006].	91
Figure 48 Traction components at the interface.	96

Figure 49 Normal traction as a function of u_n with $u_t \equiv 0$ [Needleman 1990].	98
Figure 50 Different forms of Traction-Separation laws.	99
Figure 51 Linear Traction-Separation response for cohesive elements [Abaqus 2006].	102
Figure 52 Interconnect array configuration for Test Vehicle.	104
Figure 53 Printed-Circuit assembly with Timoshenko-Beam Element interconnects and Conventional Shell-Elements.	105
Figure 54 Explicit Sub-Model with hexahedral-element corner interconnects, Timoshenko-Beam Element interconnects and PCB meshed with hexahedral reduced integration-elements with layer of cohesive elements at the solder joint-copper pad interface at both PCB and package side.	106
Figure 55 Drop-orientation has been varied from 0° JEDEC-drop to 90° free-drop.	108
Figure 56 Correlation of transient mode shapes during Free Drop.	110
Figure 57 Correlation of transient mode shapes during JEDEC Drop.	111
Figure 58 Explicit Sub-modeling technique employed at all component locations.	114
Figure 59 Time History of the displacement at the boundary nodes of the global model and the explicit sub-model.	114
Figure 60 Number of drop to failure as a function of maximum peak strain in the cohesive element at different component locations for JEDEC Drop.	119

LIST OF TABLES

Table 1	Test Vehicle.	21
Table 2	Components modeled in the global model and their respective element types.	37
Table 3	Components modeled in the local model and their respective element types.	37
Table 4	Characteristics of element types used.	38
Table 5	Material properties for individual layers of TABGA package.	44
Table 6	Element types used in smeared property models.	47
Table 7	Dimensions and masses of individual layers in the package.	47
Table 8	Comparison of actual and simulated component masses using Smeared Property Models.	47
Table 9	Element types used in Conventional Shell-Beam Model.	55
Table 10	Comparison of actual and simulated component masses using Conventional Shell-Beam Model.	55
Table 11	Element types used in Continuum Shell-Beam Model.	61
Table 12	Comparison of actual and simulated component masses using Continuum Shell-Beam Model.	61
Table 13	Correlation of peak-strain values from model predictions versus experiments for 90-Degree Free-Drop.	66

Table 14 Correlation of peak relative displacement values between various explicit models.	67
Table 15 Computational efficiency for various explicit models subject to free drop.	68
Table 16 Computational efficiency for various explicit models subject to JEDEC drop.	68
Table 17 Estimated error in prediction of solder interconnect stress in using diagonal symmetry model for Conventional Shell Beam Model subject to JEDEC drop.	71
Table 18 Estimated error in prediction of solder interconnect stress in using half symmetry model for Continuum Shell-Beam Model subject to free drop.	71
Table 19 Element types used in the Explicit Sub-Model.	77
Table 20 Test Vehicle.	104
Table 21 Correlation of peak-strain values from Timoshenko-Beam Failure Model predictions versus experiments for 90-Degree free-drop.	112
Table 22 Correlation of peak relative-displacement values with high-speed experimental data on zero-degree JEDEC Drop (mm).	112
Table 23 Correlation of peak-strain values from model predictions versus experiments for zero-degree JEDEC-Drop.	113
Table 24 Correlation of Timoshenko-Beam Failure Model predictions with experimental data for solder interconnect failure location for JEDEC Drop.	115
Table 25 Correlation of Timoshenko-Beam Failure Model predictions with experimental data for solder interconnect failure location for Free Drop.	116
Table 26 Correlation of explicit cohesive Sub-Model predictions with experimental data for solder interconnect failure location for Free Drop.	117

CHAPTER 1

INTRODUCTION

Solder joint failure in electronic products subject to shock and vibration is a dominant failure mechanism in portable electronics. Increase product-functionality concurrent with miniaturization has placed electronic interconnects in close proximity of the external impact surfaces of electronic products. Transient mechanical shock and vibration may be experienced during shipping, transportation, and normal usage.

Presently, product-level evaluation of drop and shock reliability depends heavily on experimental methods. System-level reliability response is influenced by various factors such as the drop height, orientation of drop, and variations in product design [Lim 2002, 2003]. The complex physical architecture typical of electronic products, makes it expensive, time-consuming and difficult to test solder joint reliability and dominant failure interfaces in each shock-orientation. Faster-cycle times cost and time-to-market constraints limit the number of configurations that can be fabricated and tested. Additionally, the small size of the solder interconnections makes it difficult to mount strain gages at the board-joint interface in order to measure field quantities and derivatives of field quantities such as displacement, and strain. Currently, the JEDEC drop-test [JESD22-B111 2003] is used to address board-level reliability of components,

which involves subjecting the board to a 1500g, 0.5 ms pulse in the horizontal orientation. It is often difficult to extrapolate product level performance from the board level JEDEC test since, product boundary conditions and impact orientation may be different from the test configuration.

In this research effort, the use of beam-failure models and cohesive-zone failure models for predicting first-level interconnect reliability has been investigated. Multi-scale nature of the shock model requires capture of transient dynamics at system level simultaneously with transient stress histories in the metallization interconnect pad and chip-interconnects. Previous approaches include, solid-to-solid sub-modeling [Zhu 2001, 2003] using a half test PCB board, shell-to-solid sub-modeling technique using a quarter symmetry model [Ren et al. 2003, 2004]. Inclusion of model symmetry saves computational time but targets primarily symmetric mode shapes. Use of equivalent layer models [Gu et al. 2005a, b], smeared property models [Lall et al. 2004, 2005], Conventional shell with Timoshenko-beam Element Model and the Continuum Shell with Timoshenko-Beam Element Model [Lall 2006] has been made to represent the solder joints and study their response under drop impact in an attempt to achieve computational efficiency.

Reliability of BGA packages greatly depends upon strength with which the solder joint is attached to the package. Ball shear and ball pull testing methods are currently used to determine the solder joint strength. Ductile-brittle transition from bulk solder to IMC failure was observed in the miniature Charpy test [Date et al. 2004] on increasing the shear speed from 0.2 mm/s to 1 m/s. The study of interface failures between the solder joint and the package or PCB side at high strain rates was studied by carrying out

tensile tests of solder joint arrays [Darveaux et al. 2006]. Strain rates used in these tests were from 0.001/s to 1/s.

In this work, the Conventional shell-Timoshenko Beam Element Model and the Global-Local Explicit Sub-model have been used to simulate the drop phenomenon, without any assumptions of symmetry to predict the transient dynamic behavior and interconnect stresses. In the first approach, drop simulations of printed circuit board assemblies in various orientations have been carried out using beam-shell modeling methodologies without any assumptions of symmetry. This approach enables the prediction of full-field stress-strain distribution in the system over the entire drop event. The modeling approach proposed in this study enables prediction of both symmetric and anti-symmetric modes without the penalty of decreased time-step size. A Timoshenko-Beam failure model based on the critical equivalent plastic strain value is used as a failure proxy to predict the failure mechanisms in the solder interconnections. The proposed method's computational efficiency and accuracy has been quantified with data obtained from the actual drop-test. Transient dynamic behavior of the board assemblies in free and JEDEC drop has been measured using high-speed strain and displacement measurements. Relative displacement and strain histories predicted by modeling have been correlated with experimental data. Failure data obtained by solder joint array tensile tests on ball grid array packages is used as a failure proxy to predict the failure in solder interconnections modeled using Timoshenko beam elements in the global model.

In the second approach, cohesive elements [Towashiraporn 2005, 2006] have been incorporated in the local model at the solder joint-copper pad interface at both the PCB and package side. Cohesive elements have been incorporated in the local model at

the solder joint-copper pad interface on the PCB and package side. Use of cohesive zone modeling enabled the detection of failure initiation and propagation leading to IMC brittle failure in PCB assemblies subject to drop impact. Data on solder interconnect failure has been obtained from free-drop and JEDEC-drop tests. Strains, accelerations and other relevant data have been analyzed using high speed data acquisition systems. Ultra high-speed video at 50,000 frames per second has been used to capture the deformation kinematics.

CHAPTER 2

LITERATURE REVIEW

Solder joint failure in electronic assemblies subject to shock and vibration is of major concern to the portable electronics industry. Recently, significant research has been focused to predict the solder joint reliability in electronic packages under harsh mechanical environments. Experimental techniques, analytical modeling and simulations are primarily used to evaluate the dynamic response of the system subject to drop impact. A thorough study of the literature published in this area is necessary to understand the various methodologies that have been employed to address the reliability issues.

2.1 Experimental Techniques

Solder joint reliability performance in electronic products in harsh mechanical environments such as drop impact is generally conducted using experimental techniques at the board level and the product level. Product level drop tests on completed products provide a more realistic scenario of the level of shock experienced by the solder interconnections. Product level evaluation of drop and shock reliability depends heavily on experimental methods. Board level drop testing mimics the real-life drop impact conditions and are more controllable as compared to product level drop tests. However, board level testing does not take into account the interaction between the PCB, plastic casing and other internal components of the product. Also the standardized JEDEC drop

tests do not take into account the various drop orientations with which the product may strike the impacting surface or multiple impacts due to rebounding. Shock response experienced by the PCB in product level drop can be used to set up the board level drop to reproduce the real time conditions that the package components and solder joints undergo during actual drop. In order to address these issues, extensive experimental tests are carried out to understand the variations in the dynamic responses of the PCB subject to board or product level drop.

Lim et al. [2003] carried out product level and board level drop tests on a mobile phone and its PCB respectively. In these tests, the test vehicle was gripped in various orientations and allowed to strike the impacting surface under gravity forces from desired heights using a drop tower. Results indicated additional levels of deformation of the PCB in case of product level drop due to severe rebound impact. Also, drop impact responses of various mobile phones and personal digital assistants (PDAs) were carried out at various orientations from a drop height of one meter and accelerations, strains and impact forces were measured. Maximum PCB strains and accelerations were recorded in product level drop in the horizontal direction Wu et al. [1998] carried out product level drop tests on a customized drop tester equipped with a drop control mechanism to control drop orientation and achieve a high degree of reliability. Xie et al. [2003] performed free fall board level and product level drops of area array LGA packages and measured the accelerations at the board and package side. It was found that the accelerations obtained in case of phone drop were much lower than those in the corresponding board level drop. However, FEA results showed higher values for PCB warpage and maximum plastic strain in the solder joints in case of product level drop. Dynamic shock testing of test

boards [Geng 2005] was carried out on a four point bend like shock test fixture at fixed and incremental shock levels and in-situ continuity monitoring of the solder joints was carried out to detect failure. In order to replicate the shock experienced by the PCB inside an actual PC motherboard, experimental modal analysis was carried out on the motherboard and its fundamental frequency was obtained. The test setup was then adjusted to match the fundamental frequencies of the system with the tested motherboard.

Tee et al. [2004] conducted board level drop test in accordance with the JEDEC test standards [2003] by mounting a TFBGA package in the centre of the PCB. Comprehensive dynamic responses of the PCB and the solder joints such as accelerations, strains and resistances were measured and analyzed using a multi-channel real-time electrical monitoring system. The study suggested a correlation between the dynamic strains in the PCB caused by the multiple flexing of the PCB and mechanical shock and the resulting solder joint fatigue failure. Similarly, Mishiro et al. [2002] showed correlation between the PCB strains and solder bump stresses by performing drop tests of BGA packages mounted on a motherboard. The study also showed the dependence of solder joint stress on package design and structure and stress reduction by including underfills. Lall et al. [2004, 2005] performed controlled drop tests of BGA and CSP packages from different heights in the vertical direction. Strain gages were mounted at the various component locations at both at PCB side and the package side. Strain and continuity data were obtained during the drop event with the help of a high-speed data acquisition system which recorded data at the rate of around 5 million samples per second. In addition, the drop test was monitored with ultra-high speed video camera at 40,000 frames per second. Various experimental parameters such as relative

displacements, strains, velocities, accelerations etc were acquired simultaneously. Failure analysis of the failed test specimen showed solder joint failures at the package and board interfaces and copper-trace cracking.

Shah et al. [2004] conducted displacement controlled board level bend tests on BGA packages at displacement rates corresponding to dynamic loading using a servo-hydraulic mechanical test system. The electrical connectivity of the solder joints was monitored using a daisy chained structure. Flip chip on board (FCOB) assemblies were subjected to vibration fatigue tests [Pang et al. 2004] for constant and varying G-level vibration tests to predict solder joint fatigue life. Clamped-clamped boundary conditions were imposed on the board and the tests were carried out on an electrodynamic shaker. Wang et al. [2003] performed free-fall board drop test analysis in the horizontal direction on FCOB assemblies using a shock test machine providing the half sine pulse for impact excitation. Three-point bending and four-point bending tests [Shetty et al. 2003] were carried out to investigate the fatigue failure of solder interconnects due to excessive cyclic PCB bending and flexure which may occur due to drop impact. The tests were carried out on a servo-hydraulic machine and the daisy-chained packages are continuously monitored to detect failure.

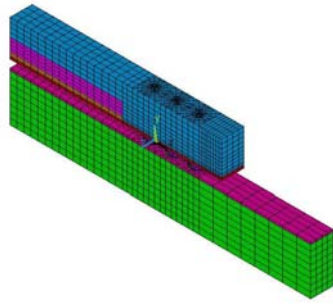
Reliability of Ball Grid Array (BGA) packages greatly depends upon strength with which the solder joint is attached to the package. Ball shear and ball pull testing methods are currently used to determine the solder joint strength. Erich et al. [1999] carried out shear tests on an Instron MTS at a shear rate of 0.5mm/min to study the interfacial failure mechanisms of BGA solder joints. The various failure mechanisms observed included pad peel, ductile bulk solder shearing and brittle fracture between the

solder and the pad. However, in actual drop events, the strain rate experienced by the solder joints is of a much higher magnitude. Ductile-brittle transition from bulk solder to IMC failure was observed in the miniature Charpy test [Date et al. 2004] on increasing the shear speed from 0.2 mm/s to 1 m/s. Solder joint integrity was tested by subjecting them to high speed impact using an Instron Micro Impactor [Wong et al., 2004] to obtain fracture characteristics such as fracture strength and fracture energy upon impact. Various solder materials with different pad finishes and mask designs were tested at static and impact shear speeds of 50 and 600 micrometers/second. It was seen that the fracture strength of the ductile bulk solder increased with shear speed while that of the brittle inter-metallic compound (IMC) decreased with shear speed. This might explain the IMC failures in solder joints subject to high strain rates during impact. Ong et al. [2004] carried out testing of eutectic solder using Split Hopkinson Pressure Bars (SHPB) to show the effect of higher strain rates on the dynamic properties of solder. Bansal et al. [2005] performed high speed four point bend tests with strain rates greater than 5000 micro strains per second in accordance with IPC/JEDEC 9702 [2004] to mimic to brittle fractures of flip chip BGA packages during PCB assembly operations with both leaded and lead-free solder alloys and ENIG pad finishes. Results indicate that the strains to failure decrease with increase in the strain rates. Shear tests at high strain rates similar to those experienced by the solder joint during drop impact were carried out on BGA and LGA packages to determine the package to board interconnection shear strength [Hanabe et al. 2004]. The tests were performed on a servo hydraulic uniaxial MTS at low and high cross-head speeds of 0.0033 mm/s and 0.5 mm/s to approximately replicate the shear forces acting on the solder joints during thermal cycling and mechanical drop. The study

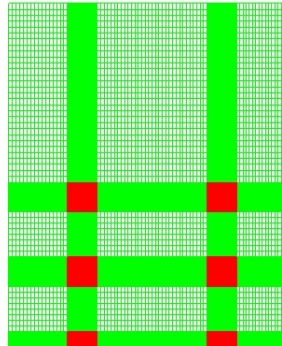
of interface failures between the solder joint and the package or PCB side at high strain rates was studied by carrying out tensile tests of solder joint arrays [Darveaux et al. 2006]. Strain rates used in these tests were from 0.001/s to 1/s. The ductile to brittle transition mode of failure at higher strain rates justifies the occurrence of the IMC failures under impact loading.

2.2 Finite Element Simulations

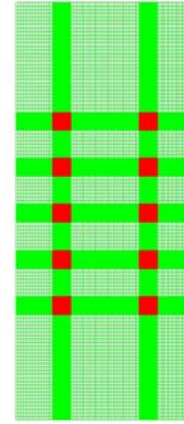
Modeling and simulation of IC packages subject to shock and vibration are very efficient tools for design analysis and optimization. Additionally, they are inexpensive, less time consuming and require much less manpower as compared to actual experimental techniques. They are very useful during the early prototype development stages where it is not possible to test every design modification. Simulation techniques are also needed to determine the potential PCB assembly failure modes as it is very difficult to measure the stresses and strains developed in the solder joints during drop test. A validated drop test model exhibiting relatively good correlation of dynamic responses of the PCB with the experimental data can be very beneficial in design enhancement and qualification of the electronic packages. Figure 1 shows the state of the art modeling techniques employed to model the PCB assemblies.



Slice Model



Symmetry Model



Full PCB Assembly

Figure 1 State of the art modeling techniques.

Tee et al. [2004] performed board level drop test simulations of 0.75 pitch TFBGA packages using a three-dimensional quarter symmetry model on the basis of symmetry to reduce the model size. The Input-G method [Tee et al. 2004] was used in the explicit finite element solver ANSYS/LS-DYNA to simulate the drop impact by applying the input acceleration pulse measured during the actual drop test to the corner screws of the PCB. Solder joint failure at the solder-PCB pad interface using maximum normal peeling stress as the failure proxy was predicted by the simulation results and was correlated with experimental observations and failure analysis. A life prediction model was proposed for QFN packages to estimate the number of drops to failure by Tee et al. [2003]. The effects of various testing parameters such as drop orientation, drop height, and PCB bending on the number of cycles to failure were studied. Pang et al. [2004] conducted finite element analysis for the vibration tests of Flip Chip On Board (FCOB) assemblies to determine the natural frequencies and mode shapes of the system under dynamic loading conditions. The global-local beam model was incorporated in this analysis by modeling the PCB and the chip with shell elements and the solder interconnections were represented by two-node beam elements with equivalent solder joint stiffness. Quasi-static analysis and dynamic drop test simulations using sub-modeling technique were modeled to predict the fatigue life of the solder joints. Three-point bending simulations [Shetty et al. 2003] of CSP packages were conducted using the global-local modeling methodology in ANSYS to predict the effect of repetitive PCB bending on solder joint failure. A quarter symmetry model was employed and appropriate boundary conditions were applied to simulate the actual test. A reliability model was developed to predict the cycles to failure based on the value of the average strain energy density in the critical solder joint in the local model.

Carroll et al. [2005] performed static and dynamic four point bending simulations to study the relationship between PCB and solder joint strains and showed a higher accumulation of plastic strain in the solder joints in case of dynamic bending tests as compared to static bending tests. Solder joints were modeled using beam elements to achieve computational efficiency and this approach was combined with the sub-modeling technique to obtain detailed stress and strain values in the critical solder joints. Wang et al. [2003] conducted two finite element analyses of the FCOB assemblies using the full and the hybrid models respectively. The full model consisted of the FCOB assembly, drop table, fixtures etc. and simulated the actual drop event. On the other hand, the hybrid model consisted of only the PCB and the IC chips and the experimentally measured displacement histories at the clamped edges of the PCB were applied as boundary conditions in the simulation. The hybrid model exhibited better correlation than the full model with respect to the experimental displacement and acceleration magnitudes. Detailed modeling of every solder joint in the PCB assembly is computationally challenging and expensive. Therefore, some methodologies need to be developed to include all the solder joints in the simulation at no computational expense. Gu et al. [2004, 2005] used equivalent layer models to represent the solder joints and simulate their behavior under drop impact. The full equivalent layer model consisted of a single three-dimensional continuum layer to represent all the individual solder joints. The hybrid model consisted of combination of the continuum layer in the non-critical areas and solder columns representing the solder interconnections in the critical areas. The equivalent material properties for the continuum layer such as the elastic modulus, density, Poisson's ratio etc were determined by numerical three-point bending, torsion

and tension tests. These equivalent layers models showed a good level of accuracy with the detailed global model and computational efficiency. Lall et al. [2004, 2005] simulated the vertical free drop of CSP packages mounted on a PCB from a height of 6 feet. In order to save processing time, the velocity of the board just before impact was calculated based on the drop height and applied to all the nodes in the model as initial conditions. The PCB was modeled using shell as well as solid elements while the components were modeled using solid elements. Smear property [Clech 1996, 1998] approach based on the volumetric averaging method was used to derive the elastic properties for the components. The simulation was carried out in ABAQUS/Explicit since explicit formulation is suitable for modeling dynamic events occurring within a short time interval. Good correlation was obtained with respect to the mode shapes, relative displacement and strain time histories. Wong et al. [2002] illustrated the fundamental mechanics and physics of a board level drop impact and the propagation of the stress wave through the assembly. A quarter symmetry model was used to simulate the drop impact of a PCB assembly. The global-local modeling methodology was incorporated in which the global beam-shell model was run in Abaqus/Explicit while the sub-model representing the critical solder ball was run in Abaqus/Standard based on the results of the global model. Differential flexing between the PCB and the package and inertia forces of the packages were found to be the dominant causes of failure. Shell-to-solid sub-modeling applied to a quarter symmetry model under impact and other loading conditions [Ren et al. 2003, 2004] was used in Abaqus/Explicit to reduce the computational time required for simulation. To validate the global-local modeling technique, Tan, et. al. [2005] modeled the PCB, solder interconnections and packages

with varying levels of detail to determine the deviation of results and its effect on computational efficiency. Comparisons of reduced models namely the shell-beam model and the shell-solid model with the detailed finely meshed solid model show reasonable comparison in terms of displacement. However, the solder ball stress comparisons in the reduced models showed poor correlation with the detailed model. Wu et al. [1998] performed product-level drop simulations to study effects of drop impact such as housing break, LCD cracking and structural disconnection. Free drop and ball bearing drop simulations were carried out for cell phones and radios to predict the LCD cracking and housing break based on the plastic strain values and validated with test results. Drop test modeling of Fairchild 6 lead Micropak mounted on a board and end product casing was carried out using implicit time formulation in ANSYS [Irving et al. 2004]. The propagation of the stress wave generated due to impact travels from the product casing to the PCB and finally to the solder joints resulting in failure. Piterassi et al. [2004] simulated the response of PC motherboards to shock loads using the simple block modeling and global property smearing approaches. Simplified block modeling involves replacing the components having significant mass and stiffness concentrations with simple homogeneous rectangular blocks. The global smeared approach involved replacing the entire motherboard with an equivalent flat plate. The equivalent mass and stiffness of the simplified blocks was determined by experimental or numerical three point bending of the individual components. Shock response spectrum (SRS) and implicit direct integration methods were used to evaluate the response due to shock loading and correlated with experimental drop testing performed on a drop table or a shaker system. Zhu et al. [2001] employed a global-local modeling technique to evaluate the reliability

of PCB assemblies subject to mechanical loading. A quarter symmetry global model is used to simulate the three-point bending and the deformation and stress-strain distribution of the PCB is obtained. The location of the critical package and solder joint is determined from these results and is modeled as the local model with a fine mesh to obtain the detailed stresses in the solder joint. Average strain energy density criterion is used to estimate the number of cycles to failure. Syed et al. [2005] simulated a three point bending test of a component level model to evaluate the equivalent stiffness of the component. This model was built using solid elements and included all the layers of the package along with the solder interconnections and the PCB and the effective modulus of the board-package combination is obtained. The global model of the board is then created with the components of equivalent mass and density and analyzed using the Input G method. Damage initiation and progression in electronic assemblies subject to mechanical shock was monitored using statistical pattern recognition, closed-form models and leading indicators of damage prediction [Lall et al. 2006]. This alternate approach to quantify damage does not require the continuous monitoring of the electrical continuity to detect failure and can be applied to any generic electronic structure. Zhu et al. [2004] performed board and product level drop simulations using the sequential explicit-implicit and sub-modeling techniques and validated with experimental tests. Effective plastic strain was chosen to be the failure criteria to determine the BGA solder joint failure since it is accumulative in nature and not oscillatory as is the case with the Von Mises stress. Towashiraporn et al. [2006] incorporated cohesive zone methodology to model the brittle fracture failure at the solder joint-copper pad interface during drop impact in ABAQUS/Explicit. Cohesive elements were placed at the solder joint-copper

pad interfaces at both the PCB and package side. The constitutive response of the cohesive elements was based on a traction-separation behavior derived from fracture mechanics. Damage initiation and evolution criteria are specified to ensure progressive degradation of the material stiffness leading to cohesive element failure.

CHAPTER 3

MODELING METHODOLOGY FOR DROP SIMULATIONS

3.1 Overview

Board level drop simulation of electronic packages using finite element analysis has proven to be a very useful qualitative tool to understand the transient dynamic behavior of these assemblies under mechanical shock loading. This research project focused on predicting the solder joint reliability in printed circuit board assemblies subject to drop impact in various orientations from varying heights. Various element formulations have been employed to model the individual components of the assembly. Approaches investigated include smeared property models, conventional shell elements with Timoshenko-beam elements, continuum shell elements with Timoshenko-beam elements and the explicit sub-models. The explicit time integration formulation has been used to simulate the drop event. The sub-modeling technique has been employed to study the stress-strain distribution in the critical solder interconnection in detail. Shell-to-solid sub-modeling technique has been employed to transfer the time history response of the global model to the local model wherein displacement degrees of freedom from the global model are interpolated to the local model and applied as boundary conditions. Transient dynamic behaviors of the board assemblies in free vertical drop and horizontal

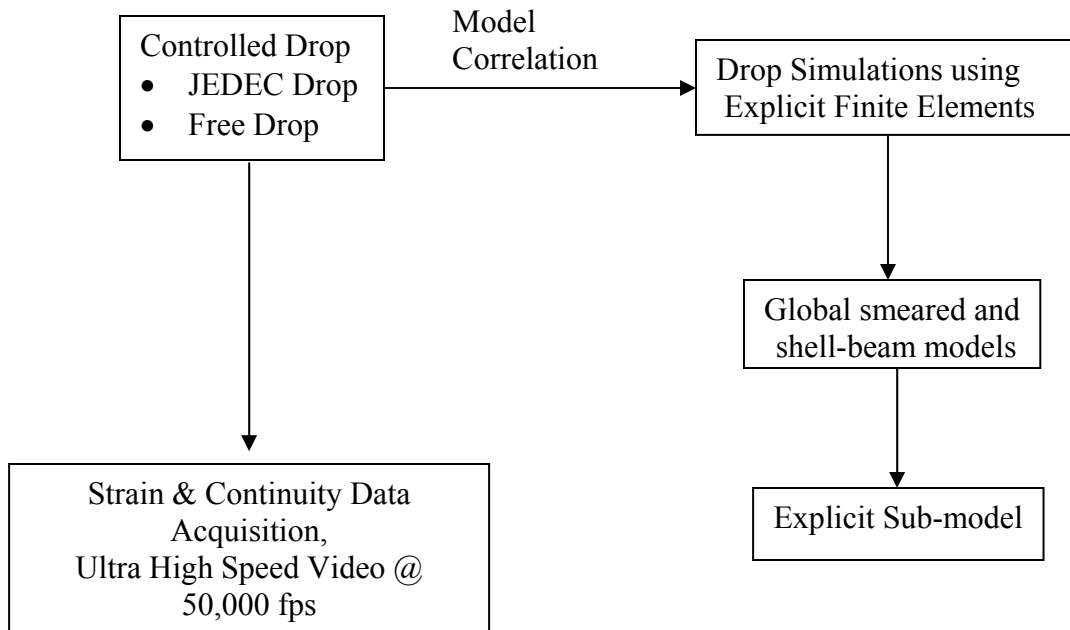
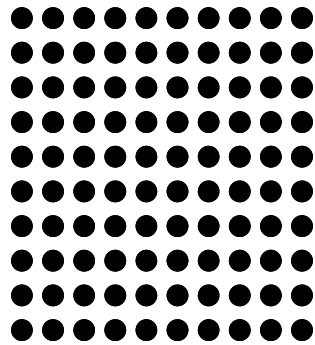


Figure 2 Modeling Methodology.

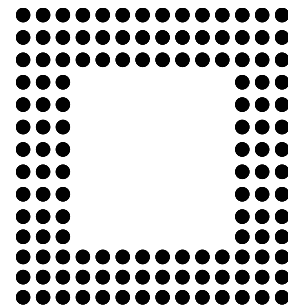
JEDEC drops have been measured using high-speed strain and displacement measurements. Models predictions have been correlated with experimental data such as relative displacement and strain histories. The modeling approach used is briefly summarized in Figure 2. Test boards were subjected to a controlled drop in both 0-degree JEDEC drops and 90-degree free vertical drops at varying heights. Table 1 shows the package attributes for the test vehicle. The test board employed was the 8 mm flex-substrate chip scale packages, with 0.5 pitch and 132 solder interconnections. The layout of the solder interconnections is shown in Figure 3. The printed circuit board was made of FR-4 and its dimensions were 2.95 inches by 2.95 inches by 0.042 inches. There were 10 components mounted on the printed circuit board as illustrated in Figure 4. All the components are on one side of the board. For the 8 mm CSP, conventional eutectic solder, 63Sn/37Pb and lead-free solder balls 95.5Sn4.0Ag0.5Cu have been studied. In the case of free drop in the 90-degree vertical orientation, a single weight was attached at the top edge of the board to simulate the batteries generally located at the top of the device. In case of horizontal drop, the board assemblies were subjected to the zero-degree orientation JEDEC drop in accordance with the JESD22-B111 standard [2003] provided by the JEDEC solid state technology association. The test board is mounted on a rigid steel base plate using four connecting screws. The components mounted on the board are facing downwards to ensure maximum deflection. The rigid base plate is then fixed to the drop table and care is taken to ensure that there is no relative motion between them. The drop table can be dropped from prescribed heights along two guide rails to strike the impacting surface.

Table 1 Test Vehicle.

	10mm 63Sn37Pb	8mm 62Sn36Pb2Ag	8mm 95.5Sn4.0Ag 0.5Cu
Ball Count	100	132	132
Ball Pitch	0.8 mm	0.5 mm	0.5 mm
Die Size	5 x 5	3.98 x 3.98	3.98 x 3.98
Substrate Thickness	0.5 mm	0.1 mm	0.1 mm
Substrate Pad Dia.	0.3 mm	0.28 mm	0.28 mm
Substrate Pad Type	SMD	Thru-Flex	Thru-Flex
Ball Dia.	0.46 mm	0.3 mm	0.3 mm



10 mm, 100 I/O BGA



8mm 132 I/O BGA

Figure 3 Interconnect array configuration for 95.5Sn4.0Ag0.5Cu and 63Sn37Pb Test Vehicles.

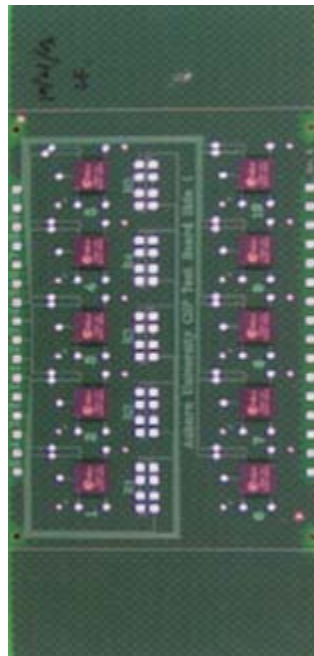


Figure 4 TABGA Test Board.

The test board was subjected to a controlled drop from heights of 6 feet and 0.5 feet for free drop (Figure 5) and JEDEC drop (Figure 6) respectively using a drop tower. Strain gages were mounted at all the component locations at both the PCB and the package sides to record the strain histories during the drop event. Strain and continuity data during the drop event was acquired using a high speed data acquisition system at a sampling rate of 5 million samples per second to detect the component failure (Figure 7). The components are daisy chained to monitor the failure of the interconnection during drop test. In-situ monitoring of the failure detection is necessary because cracks that appear in the material due to the flexing of the PCB during the drop event may close up when the PCB returns to its original shape. In addition, the drop event was simultaneously monitored using a high speed camera at 50,000 frames per second to study the deformation kinematics of the assembly. The transient mode shapes captured using this camera are used for correlation with the mode shapes obtained with simulation. Target points were attached at various points on the edge of the board to facilitate the high speed measurement of relative displacement (Figure 8). An image tracking software package was used to quantitatively measure displacements during the drop event. The target point at the top edge of the board was fixed as the reference and the relative displacements of the other target points were calculated with respect to the reference. Significant effort was put into ensuring a repeatable drop setup since small variations in the drop orientation cause large variations in the dynamic response of the board. In case of free drop, the inclination of the board with respect to a stationary vertical reference before and after impact was measured to monitor the repeatability (Figure 10). The velocity of the board

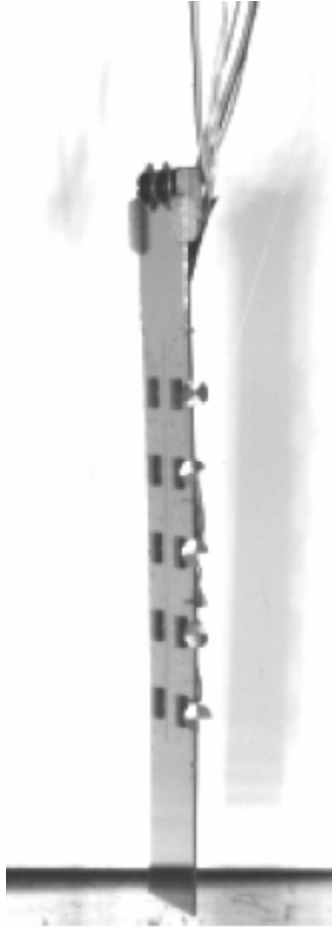


Figure 5 PCB assembly subject to 90-degree free vertical drop.

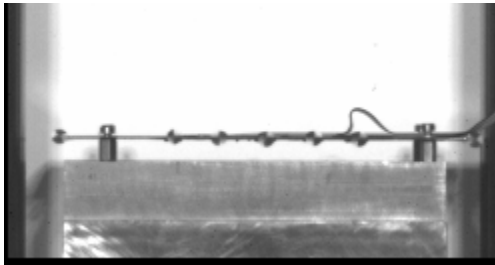


Figure 6 PCB assembly subject to 0-degree JEDEC drop.

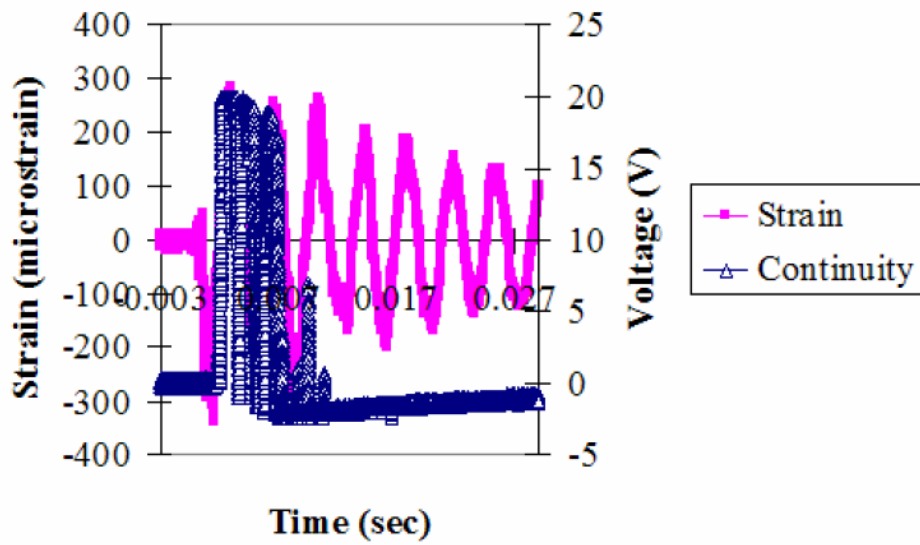


Figure 7 Measurement of initial angle prior to impact.

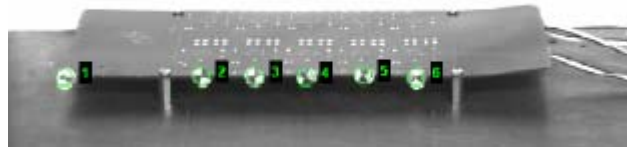


Figure 8 Test board with target points to measure relative displacement.

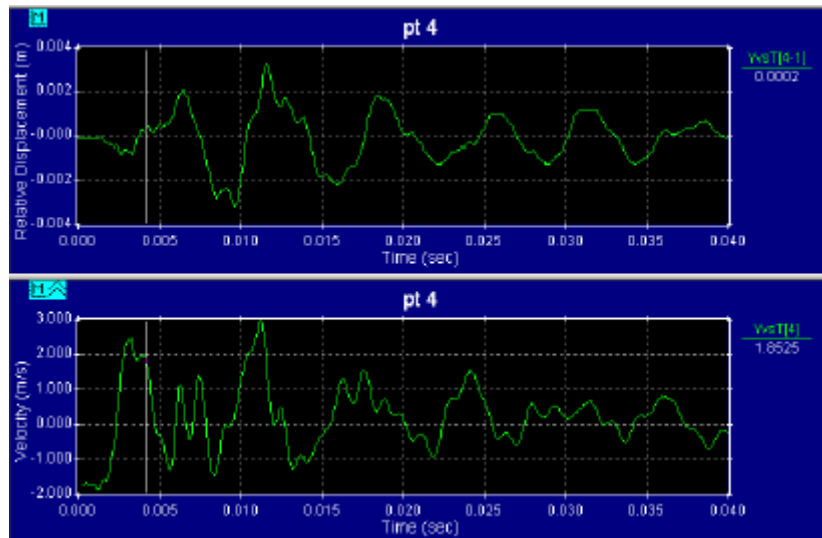


Figure 9 High Speed Image Analysis to Capture Displacement and Velocity.

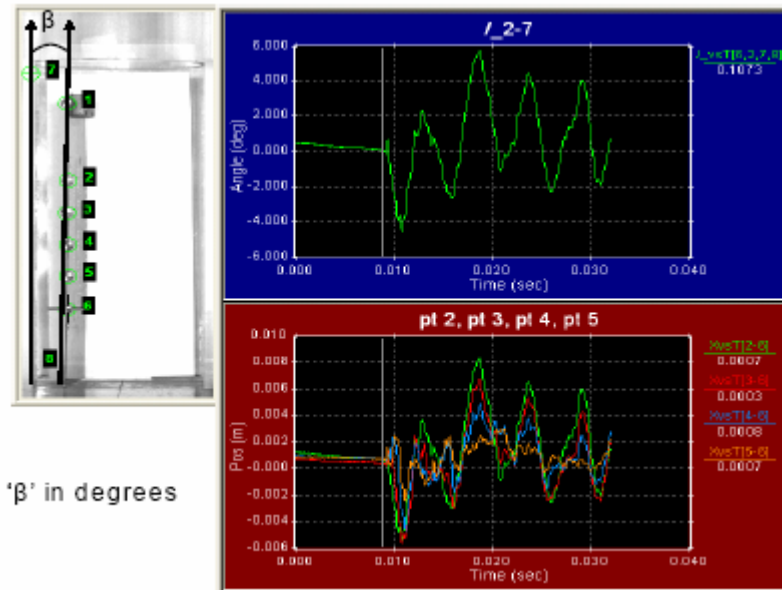


Figure 10 Transient-Strain and Continuity for Determination of Component Failure.

prior to impact was measured to correlate the controlled drop height to the free drop height.

3.2 Drop Simulation Methodology

Board level drop simulations were carried out in the 0-degree horizontal JEDEC drop and the 90-degree free vertical drop orientations. Modeling approaches employed included the smeared property models, conventional shell models with Timoshenko beam elements and the continuum shell model with Timoshenko beam elements. The analysis was carried out in the FEA commercial software ABAQUS using the explicit time integration scheme. Various element formulations such as continuum solid elements, conventional shell elements, continuum shell elements, Timoshenko beam elements and rigid elements were used to create the global models. The printed circuit board assemblies were dropped from corresponding drop heights of 0.5 feet and 6 feet for JEDEC drop and free vertical drop respectively. Figure 11 and Figure 12 show the schematic representation of the drop simulation of the PCB assemblies in free vertical drop and JEDEC drop respectively. The impact event has been modeled for the total time duration of 6 milliseconds. Time history of the relative displacement of nodes at target points located at the PCB edge was output to correlate with the experimental data. Strain histories of printed circuit board elements at the various component locations were also output to correlate with experimental data. The location of the critical package as well as the critical solder joint can also be located based on the stress and/or strain distribution obtained from the global model predictions. Then the critical package is modeled as a

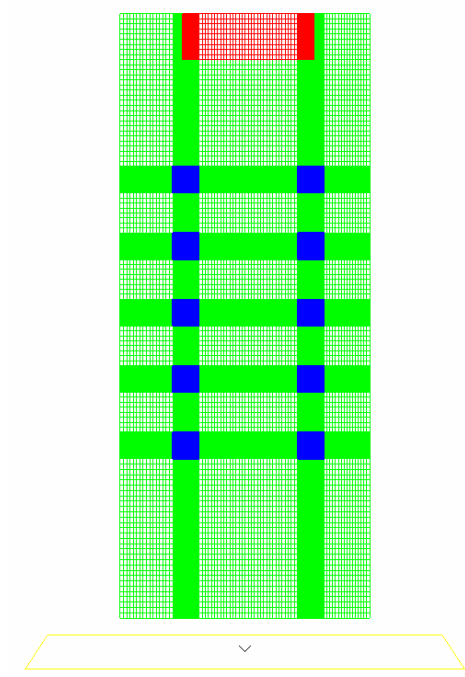


Figure 11 90-Degree Free Vertical Drop.

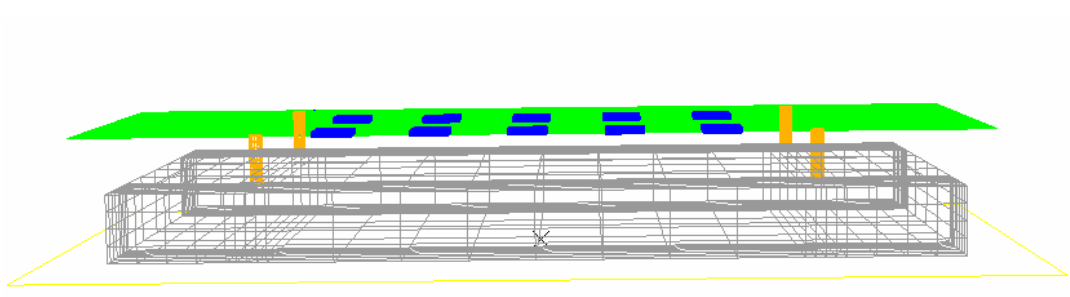


Figure 12 Zero-Degree Horizontal JEDEC Drop.

local model with a fine mesh to capture the detailed distribution of stresses and strains of interconnects and the various individual layers.

3.3 Choice of Time Integration Formulation

The transient dynamic response of a printed circuit board under drop impact has been investigated in the finite element domain with step-by-step direct integration in time for both explicit and implicit formulations. Direct integration of the system is generally used to study the nonlinear dynamic response of systems. The governing differential equation of motion for a dynamic system can be expressed as,

$$[M]\{\ddot{D}\}_n + [C]\{\dot{D}\}_n + \{R^{int}\}_n = \{R^{ext}\}_n \quad (1)$$

For a linear problem, $\{R^{int}\}_n = [K]\{D\}_n$

where $[M]$, $[C]$ and $[K]$ are the mass, damping and stiffness matrices respectively and $\{D\}_n$ is the nodal displacement vector at various instants of time.

Methods of direct integration calculate the dynamic response at time step $n+1$ from the equation of motion, a central difference formulation and known conditions at one or more preceding time steps. An explicit algorithm uses a difference expression of the general form

$$\{D\}_{n+1} = f(\{\dot{D}\}_n, \{\ddot{D}\}_n, \{D\}_{n-1}, \dots) \quad (2)$$

and is combined with the equation of motion at time step n .

An implicit algorithm uses a difference expression of the general form

$$\{D\}_{n+1} = f(\{\dot{D}\}_{n+1}, \{\ddot{D}\}_{n+1}, \{D\}_n, \{\dot{D}\}_n, \{\ddot{D}\}_n, \dots) \quad (3)$$

and is combined with the equation of motion at time step $n+1$.

In case of the explicit method, the displacements and velocities are computed based on quantities that are known at the beginning of each time step. All the terms on the right hand side of Equation(2) are known and have already been calculated at earlier time steps which is not the case for equation (3). It can be concluded that the solution of the equation of motion in one time step is much simpler using the explicit algorithm as compared to the implicit algorithm.

Explicit Formulation

For the explicit formulation, $\{D\}_{n+1}$ and $\{D\}_{n-1}$ can be expanded using the Taylor series to obtain:

$$\{D\}_{n+1} = \{D\}_n + \Delta t \{\dot{D}\}_n + \frac{\Delta t^2}{2} \{\ddot{D}\}_n + \frac{\Delta t^3}{6} \{\dddot{D}\}_n + \dots \quad (4)$$

$$\{D\}_{n-1} = \{D\}_n - \Delta t \{\dot{D}\}_n + \frac{\Delta t^2}{2} \{\ddot{D}\}_n - \frac{\Delta t^3}{6} \{\dddot{D}\}_n + \dots \quad (5)$$

Subtracting Equation(5) from Equation(4) and neglected terms with orders of Δt greater than two, the velocity and acceleration at time step n can be approximated by the central difference equations as :

$$\{\dot{D}\}_n = \frac{1}{2\Delta t} (\{D\}_{n+1} - \{D\}_{n-1}) \quad (6)$$

$$\{\ddot{D}\}_n = \frac{1}{\Delta t^2} (\{D\}_{n+1} - 2\{D\}_n + \{D\}_{n-1}) \quad (7)$$

Substituting Equations (6) and (7) in the equation of motion, equation (1) written at time step n and solving for $\{D\}_{n+1}$, we get:

$$\left[\frac{1}{\Delta t^2} M + \frac{1}{2\Delta t} C \right] \{D\}_{n+1} = \{R^{ext}\}_n - \{R^{int}\}_n + \frac{2}{\Delta t^2} [M] \{D\}_n - \left[\frac{1}{\Delta t^2} M - \frac{1}{2\Delta t} C \right] \{D\}_{n-1} \quad (8)$$

Implicit Formulation

The equations for the displacement and velocity vectors at time step n+1 using the Newmark relations can be expressed as:

$$\{\dot{D}\}_{n+1} = \{\dot{D}\}_n + \Delta t \left[\gamma \{\ddot{D}\}_{n+1} + (1-\gamma) \{\ddot{D}\}_n \right] \quad (9)$$

$$\{D\}_{n+1} = \{D\}_n + \Delta t \{\dot{D}\}_n + \frac{1}{2} \Delta t^2 \left[2\beta \{\ddot{D}\}_{n+1} + (1-2\beta) \{\ddot{D}\}_n \right] \quad (10)$$

where γ and β are numerical factors that control the characteristics of the algorithm, such as accuracy, numerical stability and amount of algorithmic damping.

Solving equation (10) for $\{\ddot{D}\}_{n+1}$ and substituting it into equation (9) we obtain the following equation:

$$\{\ddot{D}\}_{n+1} = \frac{1}{\beta \Delta t^2} (\{D\}_{n+1} - \{D\}_n - \Delta t \{\dot{D}\}_n) - \left(\frac{1}{2\beta} - 1 \right) \{\ddot{D}\}_n \quad (11)$$

$$\{\dot{D}\}_{n+1} = \frac{\gamma}{\beta \Delta t} (\{D\}_{n+1} - \{D\}_n) - \left(\frac{\gamma}{\beta} - 1 \right) \{\dot{D}\}_n - \Delta t \left(\frac{\gamma}{2\beta} - 1 \right) \{\ddot{D}\}_n \quad (12)$$

Substituting equations (11) and (12) into the equation of motion, equation (1) written at time step n+1 and solving for $\{D\}_{n+1}$, we get :

$$\begin{aligned}
\left[\mathbf{K}^{\text{eff}} \right] \{ \mathbf{D} \}_{n+1} &= \left\{ \mathbf{R}^{\text{ext}} \right\}_{n+1} + [\mathbf{M}] \left\{ \frac{1}{\beta \Delta t^2} \{ \mathbf{D} \}_n + \frac{1}{\beta \Delta t} \{ \dot{\mathbf{D}} \}_n + \left(\frac{1}{2\beta} - 1 \right) \{ \ddot{\mathbf{D}} \}_n \right\} \\
&+ [\mathbf{C}] \left\{ \frac{\gamma}{\beta \Delta t} \{ \mathbf{D} \}_n + \left(\frac{\gamma}{\beta} - 1 \right) \{ \mathbf{D} \}_n + \Delta t \left(\frac{\gamma}{2\beta} - 1 \right) \{ \dot{\mathbf{D}} \}_n \right\} \quad (13)
\end{aligned}$$

where

$$\left[\mathbf{K}^{\text{eff}} \right] = \frac{1}{\beta \Delta t^2} [\mathbf{M}] \frac{\gamma}{\beta \Delta t} [\mathbf{C}] + [\mathbf{K}]$$

Considering the equation of motion for the explicit formulation, equation (8), if $[\mathbf{M}]$ is made diagonal using the lumped approach, each time step is executed very quickly since the solution of simultaneous equations is not required. It can also be shown that using the lumped mass approach increases the allowable step time and provides better accuracy. Also, the computer storage space required is reduced to a large extent. However, this approach can be implemented only in the explicit formulation with great accuracy. For the implicit formulation, considering equation (13), we can say that $[\mathbf{K}^{\text{eff}}]$ cannot be a diagonal matrix since it contains $[\mathbf{K}]$. As a result, the computational time required to solve each time step is much higher as compared to explicit formulations. Therefore, a diagonal mass matrix provides very little computational economy. Furthermore, the implicit method is usually more accurate when $[\mathbf{M}]$ is the consistent mass matrix, thus increasing the computational time and storage space. Explicit time integration formulations are more suitable to solve wave propagation problems such as drop or impact loading wherein the response of the system to the impact lasts only for a small time interval. Implicit methods on the other hand are better suited to solve structural dynamics problems where the response of the system needs to be analyzed for a longer

period of time. The explicit algorithm is conditionally stable i.e. there is a critical value for the time step which must not be exceeded to avoid instability and error accumulation in the time integration process. Element size in the explicit model has been limited due to the conditional stability of the explicit time-integration, which influences the critical value for the time step. This value of the critical step is given by:

$$\Delta t \leq \frac{2}{\omega_{\max}} \left(\sqrt{1 - \xi^2} - \xi \right) \quad (14)$$

where ξ is the damping ratio in the ω_{\max} mode.

This limiting criterion increases the number of time steps required to span the time duration of an analysis. The critical time step is also closely related to the time required for a stress wave to cross the smallest element dimension in the model given by:

$$\Delta t = l \sqrt{\frac{\rho}{E}} \quad (15)$$

where l is the characteristic element length, ρ is the density and E is the elastic modulus.

As a result, a very finely meshed model can result in a higher time increment or if the stress wave speed in the material is very high. This makes the method computationally attractive for problems in which the total dynamic response time that must be modeled is only a few orders of magnitude longer than the critical time step. Explicit time-integration is well suited to wave propagation problems including drop impact, because the dynamic response of the board decays within a few multiples of the longest period. Most implicit formulations are unconditionally stable, which means that the process is stable regardless of the size of the time step, thus allowing a fewer number of time steps as compared to the explicit method. However, high deformation rates involved in impact,

using the implicit formulation with a large time step might introduce too much strain increase in a single time-step, causing divergence in a large deformation analysis. A large time-step may cause the contact force, which is proportional to the penetration of the contact bodies, to be very large at the contact causing local distortion and failure. Advantage of being able to use a larger time step with implicit methods can only be used in a limited manner for impact analysis. The explicit formulation is better suited to accommodate material and geometric non-linearity without any global matrix manipulation. For these reasons, the explicit time integration formulation is used in this analysis.

3.4 Element Formulations and Characteristics

Various modeling approaches have been employed to create the global and local PCB assembly models. Three explicit model approaches have been investigated including, smeared property models, Timoshenko beam element interconnect models with continuum shell element, Timoshenko-beam element interconnect models with conventional shell-element, and the explicit sub-models with a combination of Timoshenko-beam elements and reduced integration hexahedral element corner interconnects. The PCB in the global model has been modeled using reduced integration shell elements (S4R) and continuum shell elements (SC8R). For each different type of element used for the PCB, the various component layers such as the substrate, die attach, silicon die and mold compound have been modeled with reduced integration solid elements (C3D8R). Smeared properties have been derived for all the individual components based on volumetric averaging and have been modeled using C3D8R

elements. The concrete floor has been modeled using rigid R3D4 elements. The solder interconnections have been modeled with two-node Timoshenko beam elements (B31). In the case of the local model, the PCB and the various layers of the package, namely the substrate, die attach, silicon die, copper pad and mold compound have been modeled using reduced integration solid elements (C3D8R). The four corner solder interconnections were modeled using C3D8R elements while the remaining solder interconnections are modeled using Timoshenko beam elements (B31). Table 2 and Table 3 show the element types used to model the various components in the global and local models. Table 4 briefly summarizes the various element formulations used to create the global models. Characteristics of these element types are discussed in detail in the following literature.

1) Reduced Integration Solid (Continuum) Elements (C3D8R): General purpose solid elements in ABAQUS can be used in linear and non-linear analyses involving contact, plasticity and large deformations. Solid elements allow for finite strains and rotations in large displacement analysis. C3D8R is a first order, eight node linear interpolation, hexahedral element with reduced integration and hourglass control. It has three translational degrees of freedom at each of its corner nodes. First order hexahedral solid elements are generally preferred over first order triangular and tetrahedral elements in stress analysis cases since the latter elements are extremely stiff and show slow convergence with mesh refinement. Reduced integration schemes use a lower order integration to form the element stiffness matrix, thus reducing the computational time which is a significant consideration in dynamic analysis. First-order elements are recommended when large strains or very high strain gradients are expected as in the case

of impact. They are better suited to tackling complex contact conditions and severe element distortions. Higher order elements have higher frequencies than lower order elements and tend to produce noise when stress waves move across an FE mesh. Therefore, lower order elements are better than higher order elements at modeling a shock wave front.

2) Timoshenko Beam Element (B31): Beam elements are one-dimensional approximations of three-dimensional continuum based on the approximation that the cross-sectional dimensions are small compared to the dimensions along the beam axis. Timoshenko (shear flexible) beam elements (B31) available in ABAQUS are three-dimensional beams in space. They use linear interpolation schemes and are useful in dynamic problems such as impact. They have six degrees of freedom at each node including, three translational degrees of freedom (1–3) and three rotational degrees of freedom (4–6). The beam is modeled with a circular cross-section with an equivalent radius so that it has the same mass as that of an actual solder interconnection. The rotary inertia is calculated from the cross-sectional geometry. The Timoshenko beam elements use a lumped mass formulation. The rotational degrees-of-freedom have been constrained to model interconnect behavior. The B31 elements allow for shear deformation, i.e., the cross-section may not necessarily remain normal to the beam axis. [Abaqus 2005^b]. Shear deformation is useful for first-level interconnects, since it is anticipated that the shear flexibility may be important. It is assumed throughout the simulation that, the radius of curvature of the beam is large compared to distances in the cross-section and that the beam cannot fold into a tight hinge.

Table 2 Components modeled in the global model and their respective element types.

Component	Element Type
PCB	S4R, SC8R
CSP	C3D8R
Solder Interconnections	B31
Rigid Floor	R3D4
Attached Weight (Free Drop)	C3D8R
Base and Screws (JEDEC Drop)	C3D8R

Table 3 Components modeled in the local model and their respective element types.

Component	Element Type
PCB	C3D8R
CSP(Substrate, Silicon Die, Die Attach, Mold Compound, Copper Pad)	C3D8R
4 Corner Solder Interconnections	C3D8R
Remaining Solder Interconnections	B31

Table 4 Characteristics of element types used.

Element Type	Number of Nodes	Characteristics	Degrees of Freedom
C3D8R	8	First order, linear interpolation, hexahedral element with reduced integration and hourglass control.	Translational (1,2,3)
S4R	4	Quadrilateral shell element, linear interpolation with reduced integration and a large-strain formulation.	Translational and Rotational (1,2,3,4,5,6)
SC8R	8	Hexahedral, first-order interpolation, continuum shell element with reduced integration, finite membrane strain	Translational (1,2,3)
B31	2	Timoshenko beam, linear interpolation formulation.	Translational and Rotational (1,2,3,4,5,6)

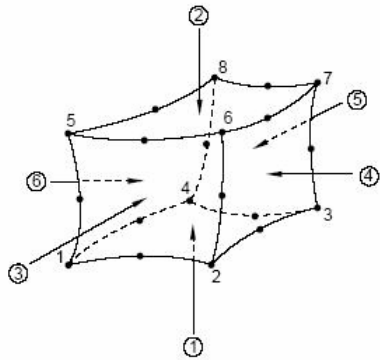
It is also assumed that the strain in the beam's cross-section is the same in any direction in the cross-section and throughout the section. For fine pitch solder interconnects, with very low stand-off heights, the constant cross-section assumption is a fairly good approximation. These elements are well suited for situations involving contact and dynamic impact.

3) Shell Elements: Two types of shell elements are available in Abaqus™ including conventional shell elements (S4R) and continuum shell elements (SC8R). The use of both elements has been investigated for modeling transient-dynamic events.

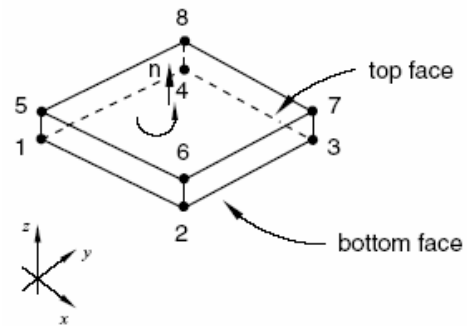
a) Conventional Shell Elements (S4R): S4R is a quadrilateral shell element, linear interpolation with reduced integration and a large-strain formulation. The conventional shell elements discretize the surface by defining the element's planar dimensions, its surface normal, and its initial curvature. Surface thickness is defined through section properties. Shell elements are used for printed circuit board since, the thickness dimension is significantly smaller than the other dimensions and the stresses in the thickness direction are smaller than in the in-plane directions. The conventional shell-element is a four-node reduced integration element which accounts for large strains and large rotations. It has six degrees of freedom- 3 translational and 3 rotational degrees of freedom per node.

b) Continuum Shell Elements (SC8R): SC8R is a hexahedral, first-order interpolation, continuum shell element with reduced integration. Continuum shell elements (SC8R) resemble three-dimensional solid elements and discretize the entire three-dimensional body. The continuum shell elements are formulated such that their kinematic and constitutive behavior is similar to conventional shell elements. The continuum shell

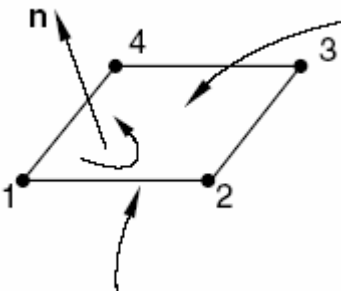
element (SC8R) has three-translational degrees of freedom at each node and the element accounts for finite membrane strains and arbitrarily large rotations [Abaqus 2005^a]. Continuum shell elements provide a refined response through the thickness and are more accurate in modeling contact than conventional shell elements.



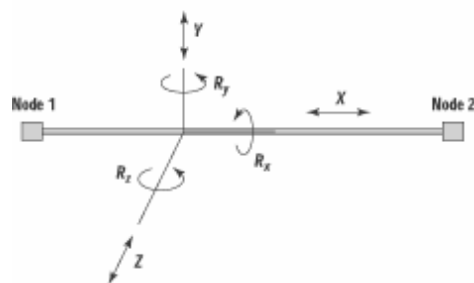
Solid (Continuum) Elements



Continuum Shell Elements



Conventional Shell Elements



Timoshenko Beam Element

Figure 13 Various element formulations employed to create the explicit models.

CHAPTER 4

FINITE ELEMENT MODELS FOR DROP SIMULATION

Various finite element models were developed to predict the transient dynamic behavior of printed circuit board assemblies subject to drop in the 90-degree free vertical direction and the horizontal direction in accordance with the JEDEC standard, JESD22-B11. Models developed to simulate free and JEDEC drop included smeared property models, conventional shell elements with Timoshenko beam elements and continuum shell elements with Timoshenko beam elements. The board-level assembly consisted of 10 components mounted on the printed circuit board. Figure 14 shows the typical architecture for the tape array ball grid array (TABGA) packages investigated in this study. Figure 15 and Figure 16 shows the schematic for the 90-degree free vertical drop and zero-degree horizontal JEDEC simulation of the TABGA board. The linear elastic material properties for the various individual layers of the package are listed in Table 5.

4.1 Smeared Property Global Model

The smeared property approach is based on the principle of volumetric averaging. This approach was proposed by Clech [1996, 1998] for the development of closed form models for solder joints subjected to thermal fatigue. In this method, the various individual layers of the chip scale package (CSP) namely the substrate, die attach, silicon

Flex BGA & TABGA

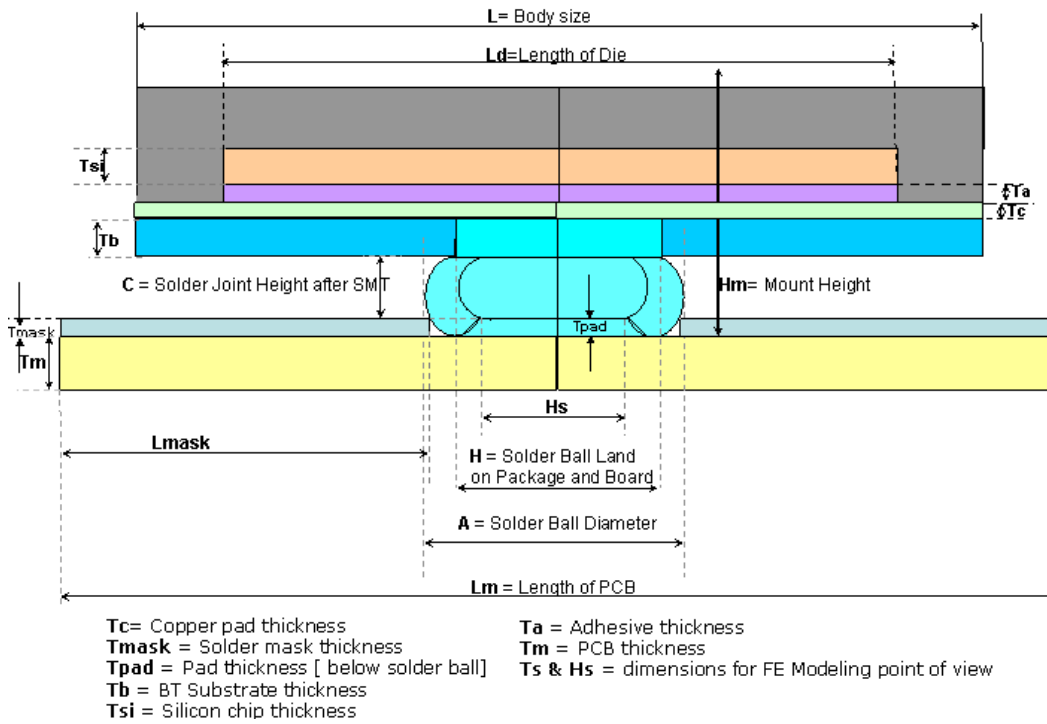


Figure 14 Typical architecture for TABGA package.

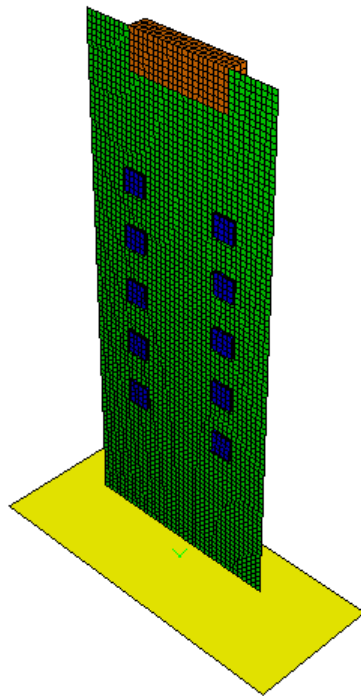


Figure 15 Schematic of 90-Degree Free Vertical Drop.

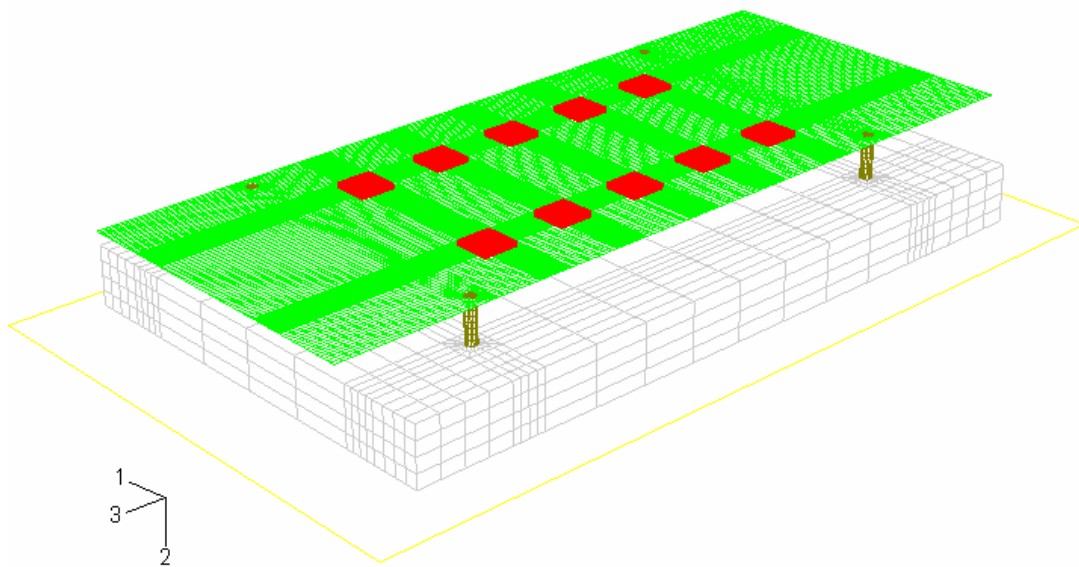


Figure 16 Schematic of Zero-Degree JEDEC Drop.

Table 5 Material Properties for individual layers of TABGA package.

Component	Elastic Modulus, E (Pa)	Poisson's Ratio (ν)	Density, ρ (kg/m^3)
Printed Circuit Board	1.6e9	0.33	1730
Solder(63Sn/37Pb)	3.2e10	0.38	8400
Silicon Die	1.124e11	0.28	2329
Copper Pad	1.29e11	0.34	8900
Die Attach	2.758e9	0.35	2200
Substrate	2.4132e10	0.30	1400
Mold Compound	1.5513e10	0.25	1970

die, mold compound and the solder interconnections are represented by a homogeneous block of elements such that it has the equivalent mass as that of the original package. The printed circuit board is modeled using first order reduced integration conventional shell elements (S4R) while the smeared property elements are modeled using first order reduced integration continuum solid elements (C3D8R). In case of free drop, the weight attached at the top edge of the board is also modeled using C3D8R elements. In case of JEDEC drop, the connecting screws and the steel base are modeled using C3D8R elements. The impacting concrete floor was modeled with R3D4 elements. Figure 17 shows the components modeled using smeared property elements. Table 6 summarizes the various element formulations employed to create the components of the smeared model. In order to ensure that the CSP represented by smeared elements closely represents the actual component, it is necessary to accurately calculate the equivalent material properties of the smeared elements. The method to obtain these parameters is explained below. Table 7 shows the masses, volumes and the equivalent layer thicknesses of the various layers considered for the calculation of the smeared properties. The equivalent thickness of each individual layer is calculated by considering each layer to have an 8mm square cross-section which is the size of each individual component.

The nomenclature used in the equations used below is as follows:

ν_c – *Poisson's Ratio of smeared element.*

ν_k – *Poisson's Ratio of individual components.*

h_k – *Layer Thickness of individual components.*

E_c – *Elastic Modulus of smeared element.*

E_k – *Elastic Modulus of individual components.*

v_k – *Volume of individual components.*

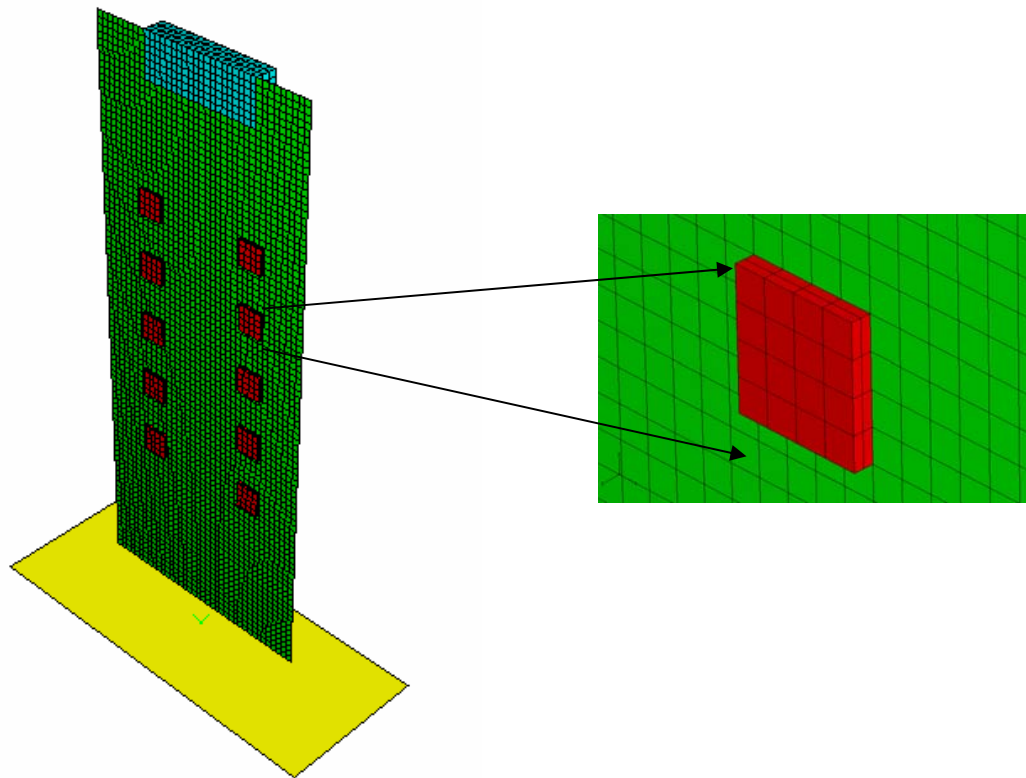


Figure 17 PCB modeled using shell (S4R) elements and CSP using smeared properties.

Table 6 Element types used in smeared property models.

Component	Element Type
PCB	S4R
CSP (Smeared Elements)	C3D8R
Rigid Floor	R3D4

Table 7 Dimensions and masses of individual layers in the package.

Component	Volume (m ³)	Mass(kg)	Equivalent Layer Thickness (m)
Solder	2.105e-9	1.769e-5	3.2891e-5
Die Attach	1.875e-9	4.125e-6	2.9297e-5
Silicon Die	7.250e-9	1.689e-5	1.132e-4
Mold Compound	6.019e-8	1.186e-4	9.4047e-4
Substrate	6.015e-8	8.421e-6	9.398e-5

Table 8 Comparison of Actual and Simulated Component Masses using Smeared Property Models.

Component	Actual (gm)	Smeared Model (gm)
PCB	28.15	28.65
8 mm CSP	0.14	0.142
Weight	31.8	31.8

Calculation of Equivalent Poisson's Ratio

$$\nu_c = \frac{\sum_{k=1}^n \nu_k h_k}{\sum_{k=1}^n h_k}$$

$$\nu_c = \frac{(0.38 \times 3.2891 \times 10^{-5}) + (0.35 \times 2.9297 \times 10^{-5}) + (0.28 \times 1.132 \times 10^{-4}) + (0.25 \times 9.4047 \times 10^{-4}) + (0.3 \times 9.398 \times 10^{-5})}{3.2891 \times 10^{-5} + 2.9297 \times 10^{-5} + 1.132 \times 10^{-5} + 9.4047 \times 10^{-4} + 9.398 \times 10^{-5}}$$

$$\nu_c = \frac{3.1776 \times 10^{-4}}{1.20984 \times 10^{-3}}$$

$$\nu_c = 0.2626$$

Calculation of Equivalent Elastic Modulus

$$\frac{E_c h_c^3}{12(1-\nu_c)} = \sum_{k=1}^n \frac{E_k h_k^3}{12(1-\nu_k)}$$

$$\frac{E_c \times (1.20984 \times 10^{-3})^3}{12(1-0.2626)} = \frac{3.2 \times 10^{10} \times (3.2891 \times 10^{-5})^3}{12(1-0.38)} + \frac{2.758 \times 10^9 \times (2.9297 \times 10^{-5})^3}{12(1-0.35)} + \frac{1.124 \times 10^{11} \times (1.132 \times 10^{-4})^3}{12(1-0.28)} + \frac{1.5513 \times 10^{10} \times (9.4047 \times 10^{-4})^3}{12(1-0.25)} + \frac{2.4132 \times 10^{10} \times (9.398 \times 10^{-5})^3}{12(1-0.3)}$$

$$E_c = 7.2725 \times 10^9 \text{ N/m}^2$$

Calculation of Equivalent Density

$$\rho_c = \frac{\sum_{k=1}^n \rho_k v_k}{\sum_{k=1}^n v_k}$$

$$\rho_c = \frac{(8400 \times 2.105 \times 10^{-9}) + (2200 \times 1.875 \times 10^{-9}) + (2329 \times 7.250 \times 10^{-9}) + (1970 \times 6.019 \times 10^{-8}) + (1400 \times 6.015 \times 10^{-9})}{2.105 \times 10^{-9} + 1.875 \times 10^{-9} + 7.250 \times 10^{-9} + 6.019 \times 10^{-8} + 6.015 \times 10^{-9}}$$

$$\rho_c = 2140 \text{ kg/m}^3$$

Table 8 shows the simulated weight of the smeared property model for all components and the test board and the actual weights. It can be seen that the simulated weight of the PCB assembly closely approximates the actual weight. The printed circuit board assemblies were dropped from a height of 6 feet in the vertical orientation for free drop and from a height of 0.5 feet in the horizontal orientation for JEDEC drop. To save computational time, the near-impact velocity of the test assembly, which is a function of drop height, is applied as an initial condition to the various components of the PCB assembly. The relation is given by:

$$V = \sqrt{2gH}$$

where V is the impact velocity corresponding to drop height H.

For free drop, the initial velocity corresponding to a height of 6 feet i.e. 1.8288 meters is given by:

$$V = \sqrt{2 \times 9.81 \times 1.8288}$$

$$V = 5.992 \text{ m/s.}$$

For JEDEC drop, the initial velocity corresponding to a height of 0.5 feet i.e. 0.1524 meters is given by:

$$V = \sqrt{2 \times 9.81 \times 0.1524}$$

$$V = 1.729 \text{ m/s.}$$

A weight was attached at the top edge of the board to control the drop orientation. A reference node was placed behind the rigid floor for application of constraints and all the degrees of freedom of that node were constrained. Node to surface contact was specified between the impacting edge of the PCB and the rigid floor for free drop simulation. Node

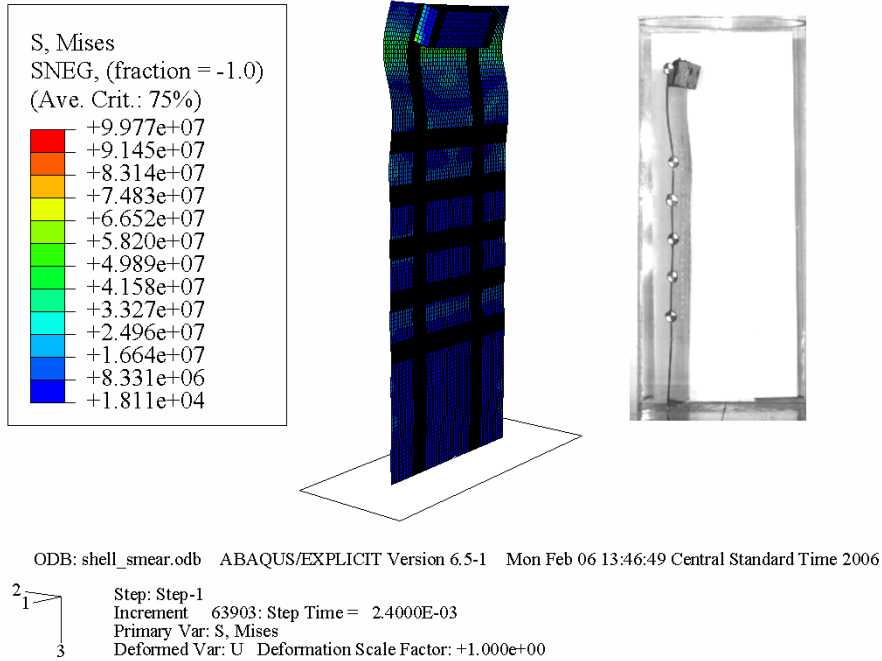
to surface contact was specified between the impacting bottom surface of the steel base and the rigid floor for JEDEC drop. The impact event was modeled for the total time duration of 6 milliseconds. Time history of the relative displacements of nodes at target points located at the PCB edge were output to correlate with the experimental data. Strain histories of printed circuit board elements at all the component locations were also output to correlate with experimental data.

Figure 18 shows the correlation between the predicted transient mode shapes of the PCB assembly and the experimental mode shapes which were obtained by recording the actual drop event using high-speed cameras at time intervals of 2.4 ms and 4.5 ms for free drop.

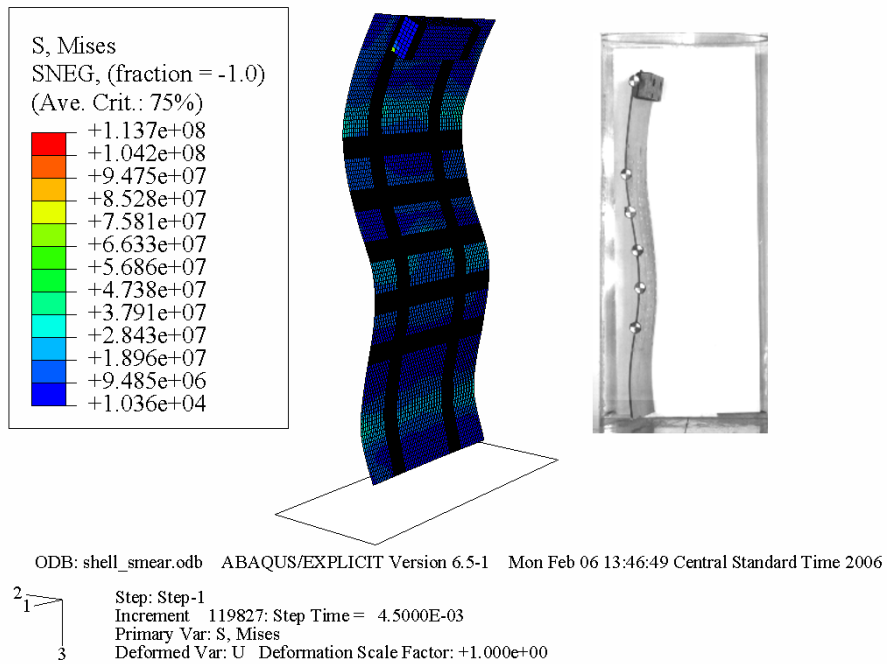
Figure 19 shows the correlation between the predicted transient mode shapes of the PCB assembly and the experimental mode shapes which were obtained by recording the actual drop event using high-speed cameras at time intervals of 2.4 ms and 4.8 ms for JEDEC drop. Good correlation has been achieved between the predicted and experimentally observed mode shapes. Correlation of peak relative displacements and strains with experimental data is discussed later in this chapter.

4.2 Conventional Shell-Beam Model

In this approach, the PCB has been modeled using first-order reduced integration four-node conventional shell elements (S4R) and each solder interconnection is represented by three-dimensional Timoshenko beams in space (B31) with six degrees of freedom. S4R is a quadrilateral shell element, linear interpolation with reduced integration and a large-strain formulation. Shell elements are used for printed circuit board since the thickness dimension is significantly smaller than the other dimensions. Beam elements are one-

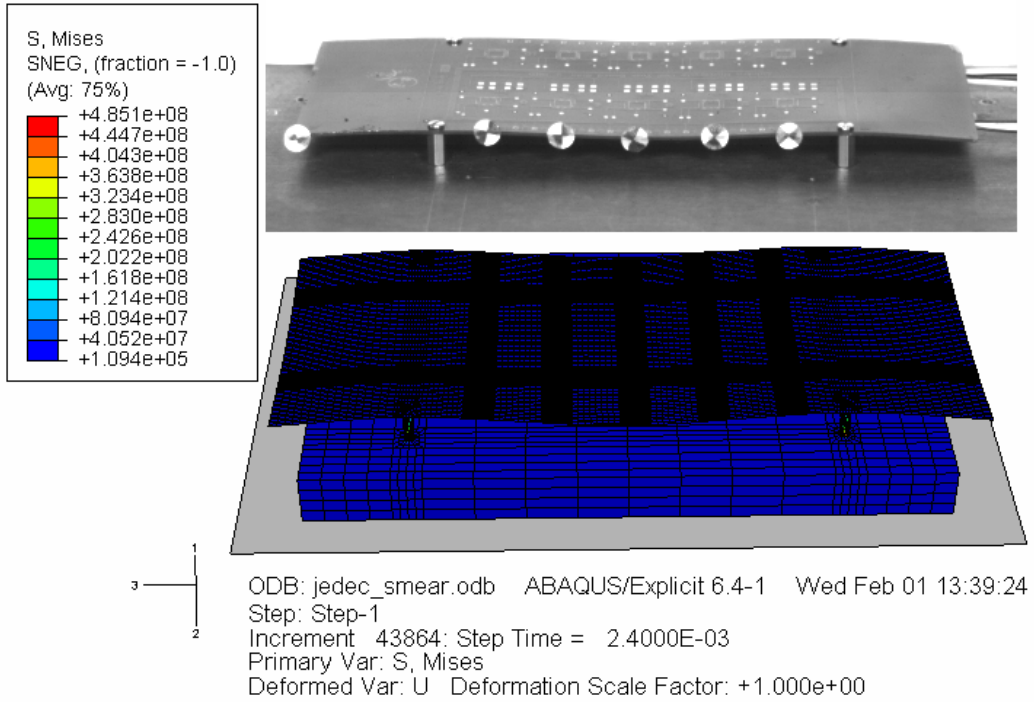


$t = 2.4 \text{ ms}$

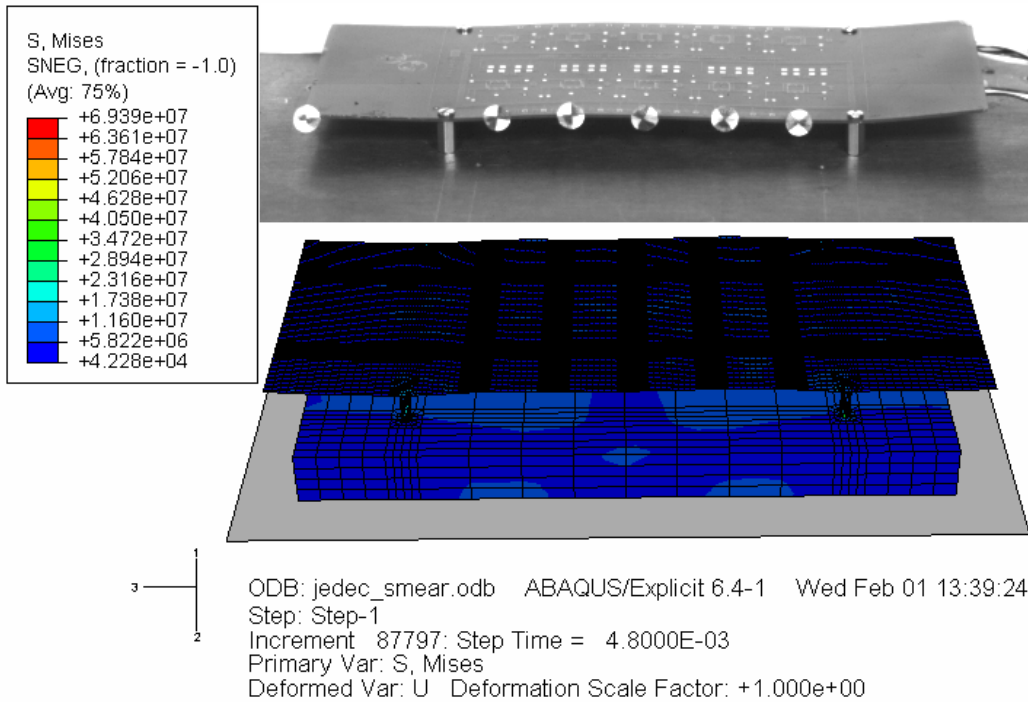


$t = 4.5 \text{ ms}$

Figure 18 Correlation of Transient Mode-Shapes for Smeared Element Model during Free Vertical Drop.



t = 2.4 ms



t = 4.8 ms

Figure 19 Correlation of Transient Mode-Shapes for Smeared Element Model during JEDEC Drop.

dimensional approximations of three-dimensional continuum based on the approximation that the cross-sectional dimensions are small compared to the dimensions along the beam axis. The beam is modeled with a circular cross-section with an equivalent radius so that it has the same mass and volume as that of an actual solder interconnection. The dimensions of the solder joint were measured by observing a cross-sectional sample of the package under an electron microscope. Using those dimensions, the solder joint was modeled as a linear elastic material and its volume and mass were calculated. The Timoshenko beam was then given an equivalent radius to define its cross-section such that it had the same mass and volume as that of the original solder joint as shown below:

$$\text{Volume of single solder joint} = 1.59510^{-11} m^3$$

$$\text{Height of solder joint (h)} = 0.2 \times 10^{-3} m$$

Considering the beam to be cylindrical in volume, we have :

$$\text{Volume of single solder beam} = \pi r^2 h$$

$$\text{Therefore, } \pi r^2 h = 1.59510^{-11}$$

$$\Rightarrow r = 1.5933 \times 10^{-4} m$$

All the individual layers of the package such as the substrate, die attach, silicon die and the mold compound have been modeled in detail using first order reduced integration continuum solid elements (C3D8R). The weight attached at the top edge of the board is also modeled using C3D8R elements. The impacting concrete floor was modeled with R3D4 elements. The connecting screws and the steel base were modeled using solid elements (C3D8R). Element types to model the various components of the models are listed in Table 9. Table 10 shows the simulated weight of the various components of the conventional shell-beam model and the actual weights. It can be seen that the simulated weight of the PCB assembly closely approximates the actual weight. The impacting

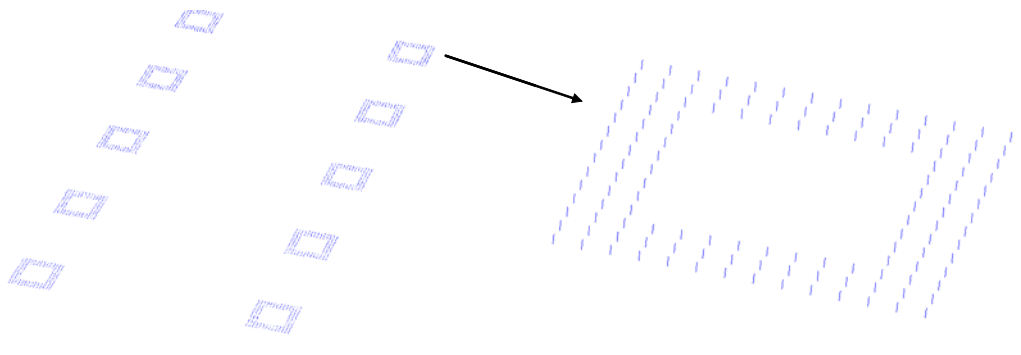


Figure 20 Solder Interconnection Layout Modeled Using Timoshenko Beam elements.

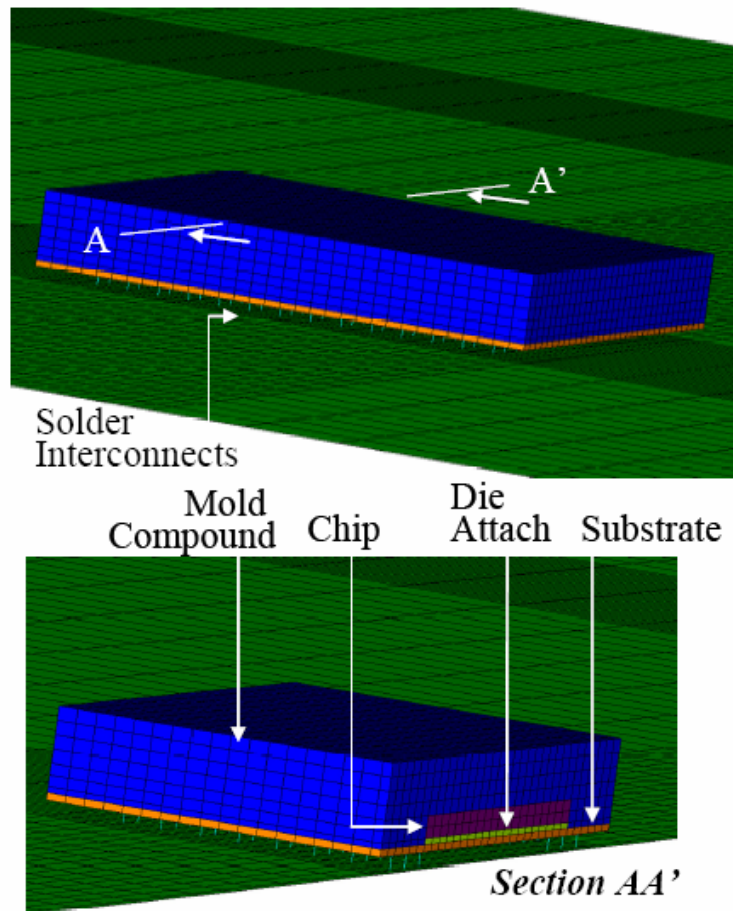


Figure 21 Printed-Circuit Assembly with Timoshenko-Beam Element Interconnects and Conventional Shell-Elements.

Table 9 Element types used in Conventional Shell-Beam model.

Component	Element Type
PCB	S4R
Solder Interconnections	B31
Substrate	C3D8R
Silicon Die	C3D8R
Die Attach	C3D8R
Mold Compound	C3D8R
Rigid Floor	R3D4

Table 10 Comparison of Actual and Simulated Component Masses using Conventional Shell-Beam Model.

Component	Actual (gm)	Smearred Model (gm)
PCB	28.15	28.65
8 mm CSP	0.14	0.148
Weight	31.8	31.8

concrete floor was modeled with R3D4 elements. Figure 20 shows the layout of the solder interconnections modeled using the Timoshenko beam elements. Figure 21 shows the close-up of one of the packages with the PCB modeled using S4R elements and its cross-sectional view with all the individual layers. Drop simulation of the PCB assembly was carried out from a height of 6 feet in the vertical orientation for free drop and a height of 0.5 feet in the horizontal orientation. To save computational time, initial velocities of 5.992 m/s and 1.729 m/s corresponding to heights of 6 feet and 0.5 feet were applied to the nodes of all the components in the assembly for free vertical drop and JEDEC drop respectively. The rotational degrees of freedom of the Timoshenko beam elements were constrained to model interconnect behavior. Node to surface contact was specified between the impacting edge of the PCB and the reference node of the rigid floor for free drop simulation. Similarly, node to surface contact was specified between the impacting surface of the base and the reference node of the rigid floor which was constrained in all degrees of freedom for JEDEC drop. The impact event was modeled for the total time duration of 6 milliseconds. Time history of the relative displacement of nodes at target points located at the PCB edge and the PCB strain histories at various component locations were output to correlate with the experimental data.

Figure 22 shows the correlation between the predicted transient mode shapes of the PCB assembly and the experimental mode shapes which were obtained by recording the actual drop event using high-speed cameras at time intervals of 2.4 ms and 4.2 ms for free drop. Figure 23 shows the correlation between the predicted transient mode shapes of the PCB assembly and the experimental mode shapes which were obtained by recording the actual drop event using high-speed cameras at time intervals of 2.4 ms and 4.8 ms in

case of JEDEC drop. Good correlation has been achieved between the predicted and experimentally observed mode shapes. Correlation of peak relative displacements and strains with experimental data has been discussed later in this chapter.

4.3 Continuum Shell-Beam Model

In this approach, the PCB has been modeled using first-order reduced integration eight-node continuum shell elements (SC8R) and each solder interconnection is represented by three-dimensional Timoshenko beams in space (B31) with six degrees of freedom. SC8R is a hexahedral, first-order interpolation, continuum shell element with reduced integration. Continuum shell elements (SC8R) resemble three-dimensional solid elements and discretize the entire three-dimensional body. Beam elements are modeled with a circular cross-section with an equivalent radius so that it has the same mass and volume as that of an actual solder interconnection as shown below:

$$\text{Volume of single solder joint} = 1.59510^{-11} m^3$$

$$\text{Height of solder joint (h)} = 0.2 \times 10^{-3} m$$

Considering the beam to be cylindrical in volume, we have :

$$\text{Volume of single solder beam} = \pi r^2 h$$

$$\text{Therefore, } \pi r^2 h = 1.59510^{-11}$$

$$\Rightarrow r = 1.5933 \times 10^{-4} m$$

All the individual layers of the package such as the substrate, die attach, silicon die and the mold compound have been modeled in detail using first order reduced integration continuum solid elements (C3D8R). The impacting concrete floor was modeled with R3D4 elements.

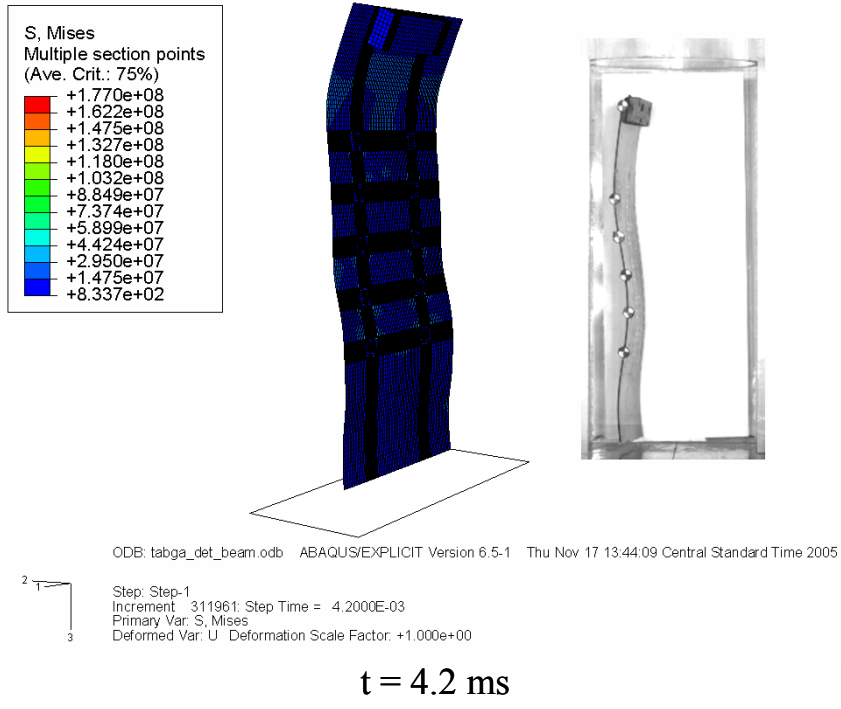
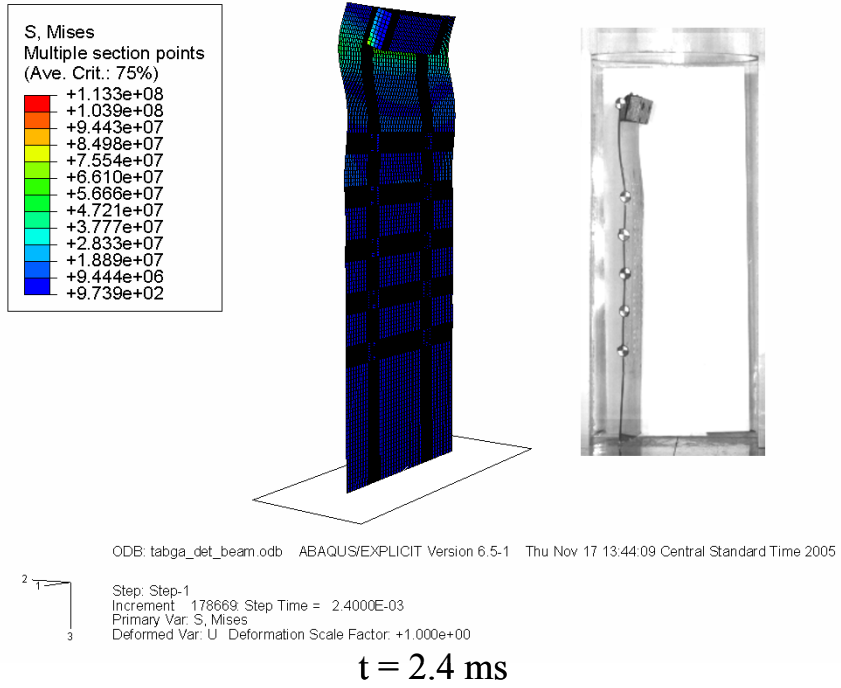
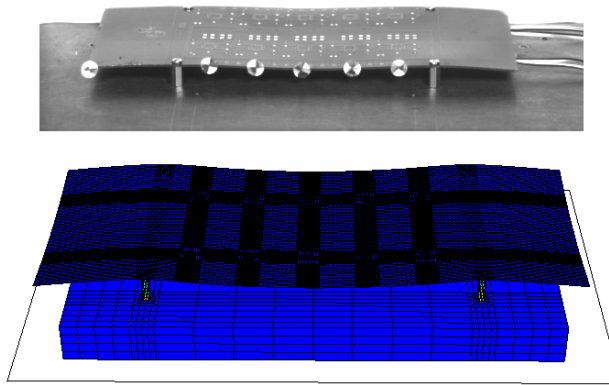
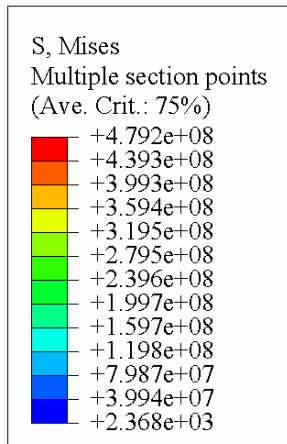


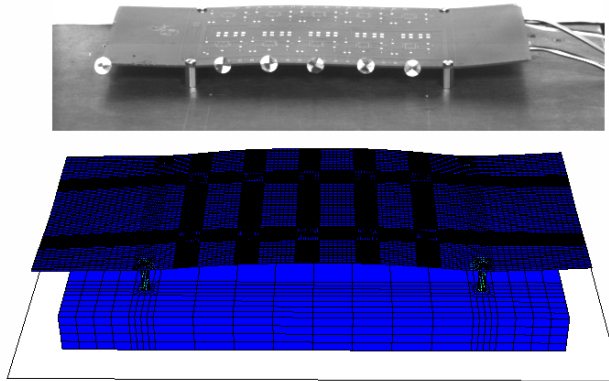
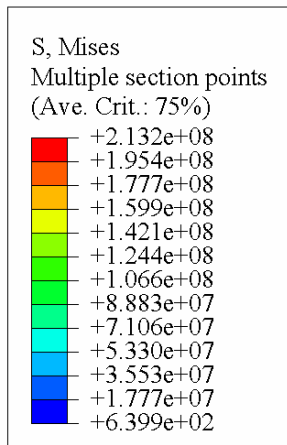
Figure 22 Correlation of Transient Mode-Shapes for Conventional-Shell Timoshenko-Beam Model during Free Vertical Drop.



ODB: jedec_detail.odb ABAQUS/EXPLICIT Version 6.5-1 Thu Feb 02 15:45:02

Step: Step-1
Increment 178669: Step Time = 2.4000E-03
Primary Var: S, Mises
Deformed Var: U Deformation Scale Factor: +1.000e+00

t = 2.4 ms



ODB: jedec_detail.odb ABAQUS/EXPLICIT Version 6.5-1 Thu Feb 02 15:45:02

Step: Step-1
Increment 356392: Step Time = 4.8000E-03
Primary Var: S, Mises
Deformed Var: U Deformation Scale Factor: +1.000e+00

t = 4.8 ms

Figure 23 Correlation of Transient Mode-Shapes for Conventional-Shell Timoshenko-Beam Model during JEDEC Drop.

Element types to model the various components of the models are listed in Table 11. Table 12 shows the simulated weight of the various components of the continuum shell-beam model and the actual weights. It can be seen that the simulated weight of the PCB assembly closely approximates the actual weight. Figure 24 shows the layout of the solder interconnections modeled using the Timoshenko beam elements. Figure 25 shows the close-up of one of the packages with the PCB modeled using SC8R elements and its cross-sectional view with all the individual layers. Drop simulation of the PCB assembly was carried out from a height of 6 feet in the vertical orientation for free drop and a height of 0.5 feet in the horizontal orientation. To save computational time, initial velocities of 5.992 m/s and 1.729 m/s corresponding to heights of 6 feet and 0.5 feet were applied to the nodes of all the components in the assembly for free vertical drop and JEDEC drop respectively. The rotational degrees of freedom of the Timoshenko beam elements were constrained to model interconnect behavior. Node to surface contact was specified between the impacting edge of the PCB and the reference node of the rigid floor for free drop simulation. Similarly, node to surface contact was specified between the impacting surface of the base and the reference node of the rigid floor which was constrained in all degrees of freedom for the JEDEC drop. The impact event was modeled for the total time duration of 6 milliseconds. Time history of the relative displacement of nodes at target points located at the PCB edge and the PCB strain histories at various component locations were output to correlate with the experimental data. Figure 26 shows the correlation between the predicted transient mode shapes of the PCB assembly and the experimental mode shapes which were obtained by recording the

Table 11 Element types used in Continuum Shell-Beam model.

Component	Element Type
PCB	SC8R
Solder Interconnections	B31
Substrate	C3D8R
Silicon Die	C3D8R
Die Attach	C3D8R
Mold Compound	C3D8R
Rigid Floor	R3D4
Attached Weight (Free Drop)	C3D8R
Connecting Screws (JEDEC Drop)	C3D8R
Steel Base (JEDEC Drop)	C3D8R

Table 12 Comparison of Actual and Simulated Component Masses using Continuum Shell-Beam Model.

Component	Actual (gm)	Smeared Model (gm)
PCB	28.15	28.65
8 mm CSP	0.14	0.148
Weight (Free Drop)	31.8	31.8



Figure 24 Solder Interconnection Layout Modeled Using Timoshenko Beam elements.

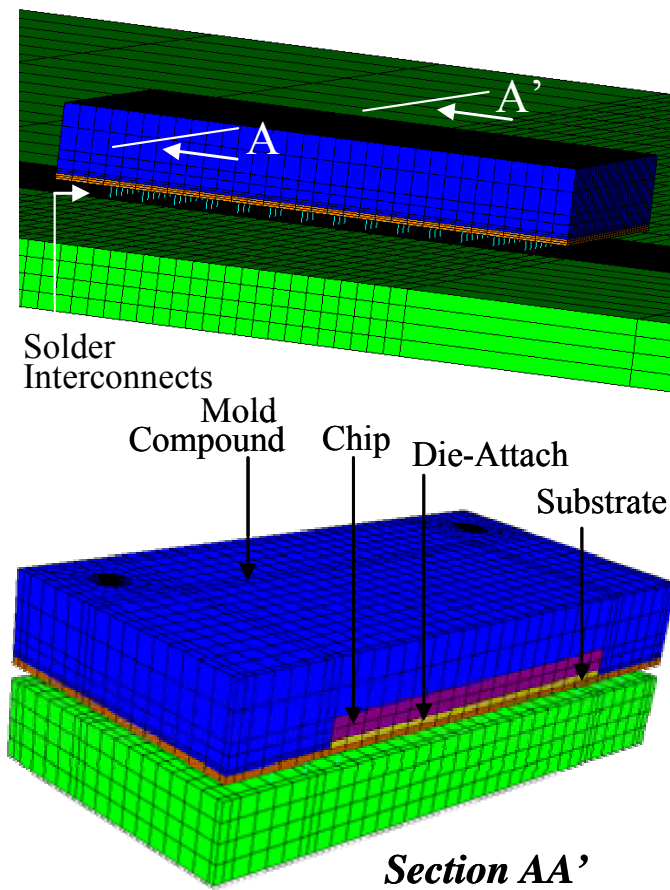
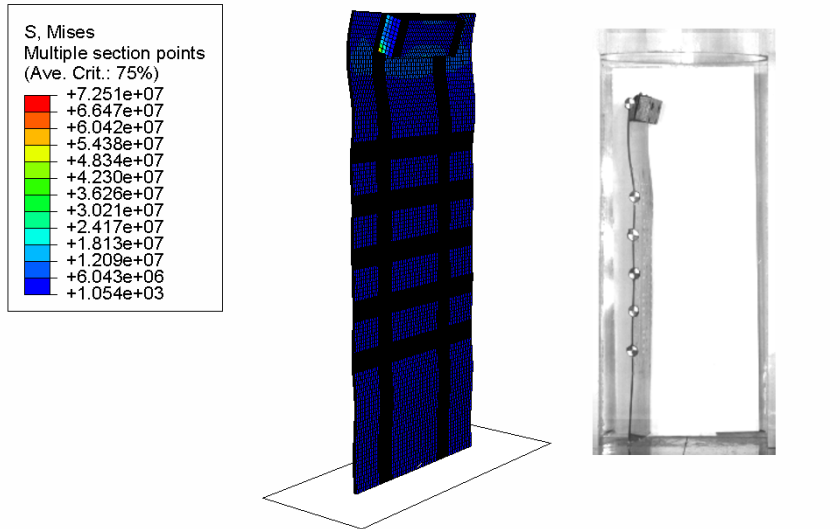
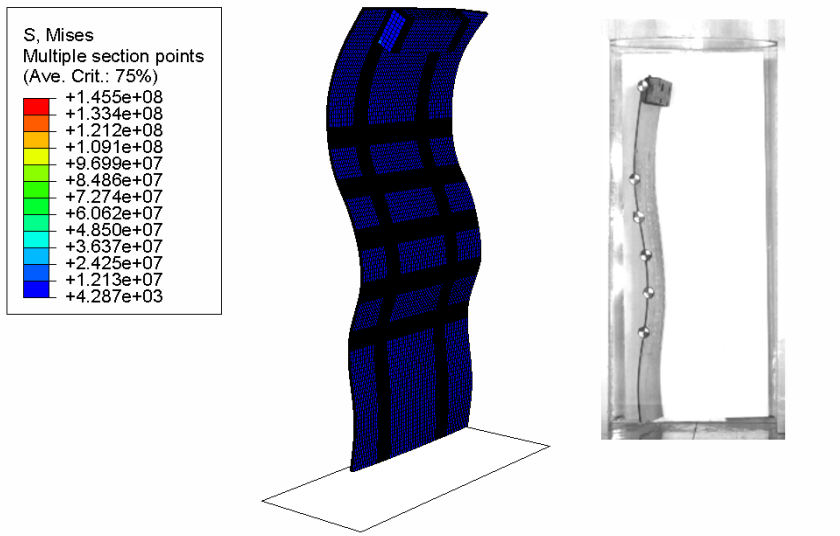


Figure 25 Printed-Circuit Assembly with Timoshenko-Beam Element Interconnects and Continuum Shell-Elements.



Step: Step-1
Increment: 178669 Step Time = 2.4000E-03
Primary Var: S, Mises
Deformed Var: U Deformation Scale Factor: +1.000e+00

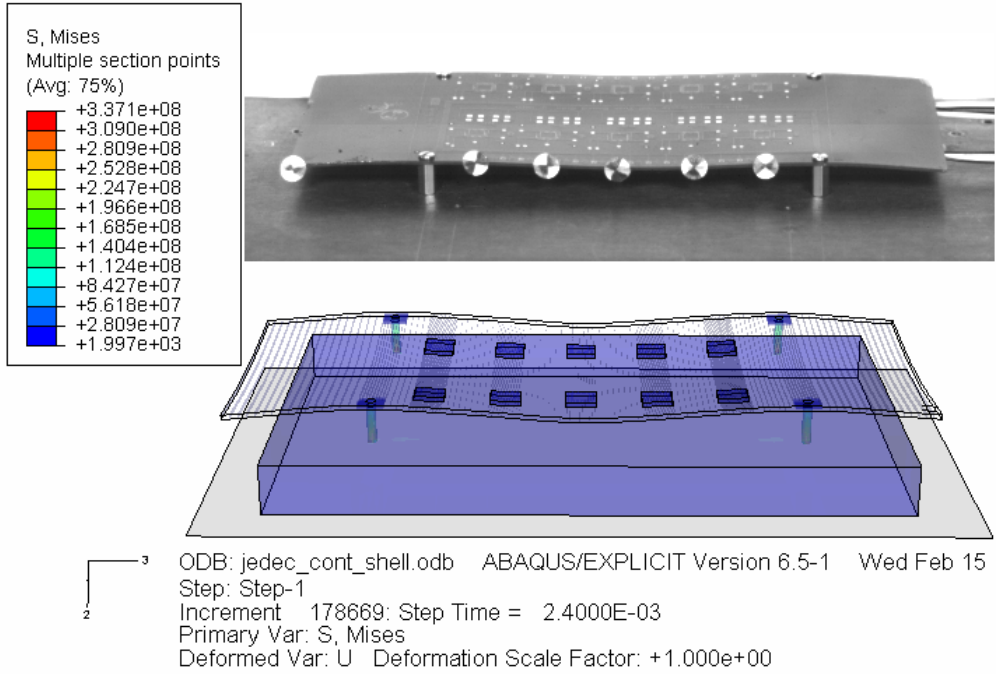
t = 2.4 ms



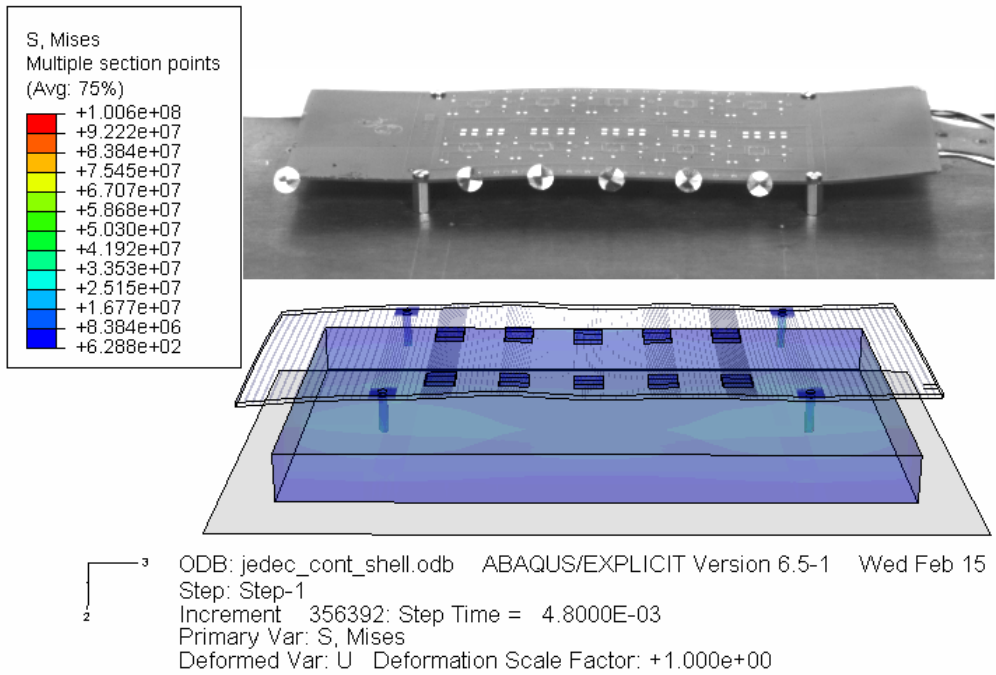
Step: Step-1
Increment: 334176 Step Time = 4.5000E-03
Primary Var: S, Mises
Deformed Var: U Deformation Scale Factor: +1.000e+00

t = 4.5 ms

Figure 26 Correlation of Transient Mode-Shapes for Continuum-Shell Timoshenko-Beam Model during Free Vertical Drop.



t = 2.4 ms



t = 4.8 ms

Figure 27 Correlation of Transient Mode-Shapes for Continuum-Shell Timoshenko-Beam Model during JEDEC Drop.

actual drop event using high-speed cameras at time intervals of 2.4 ms and 4.5 ms for free drop. Figure 27 shows the correlation between the predicted transient mode shapes of the PCB assembly and the experimental mode shapes which were obtained by recording the actual drop event using high-speed cameras at time intervals of 2.4 ms and 4.8 ms for JEDEC drop. Good correlation has been achieved between the predicted and experimentally observed mode shapes.

4.4 Correlation of Predicted Peak Relative Displacement and Strain Histories

In this section, the field quantities and derivatives of field quantities namely relative displacement and strain from both various explicit finite element models and experimental data have been compared for both free drop and JEDEC drop. Specifically, peak relative displacement and peak strain values have been correlated for the models versus experimental data. The peak strain values exhibit error in the range of 10-30 % as observed in Table 13. All the three modeling approaches including smeared properties, conventional-shell with beam elements, and continuum-shell with beam elements exhibit similar results. The peak relative displacement values as shown in Table 14 exhibit error in the neighborhood of 8-28%. Table 15 and Table 16 list the computational efficiency versus number of elements and nodes for all the global models for free and JEDEC drop respectively. Figure 28 and Figure 29 show the correlation of the board relative displacement 2.4 ms and 4.5 ms after impact, from high-speed image analysis with the model predictions from smeared, continuum-shell with Timoshenko-beam, conventional-shell with Timoshenko-beam models for JEDEC drop and free drop respectively.

Table 13 Correlation of Peak-Strain Values from Model Predictions Versus Experiments for 90-degree Free-Drop.

	Loc 1	Loc 3	Loc 5
Experiment	1417	2248	1667
Smeared Property	1603	1563	1424
Error (%)	-13.15	30.48	14.56
Timoshenko-Beam with Continuum Shell	1820	1990	1960
Error (%)	-28.47	11.49	-17.60
Timoshenko-Beam with Conventional Shell	1760	1630	2070
Error (%)	-24.24	27.50	-24.20

Table 14 Correlation of peak relative displacement values between various explicit models.

	Loc 1	Loc 3	Loc 5
Experiment (mm)	3.61	4.47	4.58
Smeared Property	3.86	3.35	3.39
Error (%)	-7.03	24.93	25.86
Timoshenko-Beam, Continuum Shell	3.80	4.16	3.26
Error (%)	-5.17	6.97	28.73
Timoshenko-Beam, Conventional Shell	4.43	4.85	4.15
Error (%)	-22.8	-8.62	9.21

Table 15 Computational efficiency for various explicit models subject to free drop.

Model	Number of elements	Number of nodes	Computational time(sec)
Smeared Model	75809	79126	59400
Conventional Shell-Beam Model	118089	133576	219600
Continuum Shell-Beam Model	214857	264124	568800

Table 16 Computational efficiency for various explicit models subject to JEDEC drop.

Model	Number of elements	Number of nodes	Computational time
Smeared Model	77825	82135	43200
Conventional Shell-Beam Model	120105	136585	226800
Continuum Shell-Beam Model	218026	268480	584580

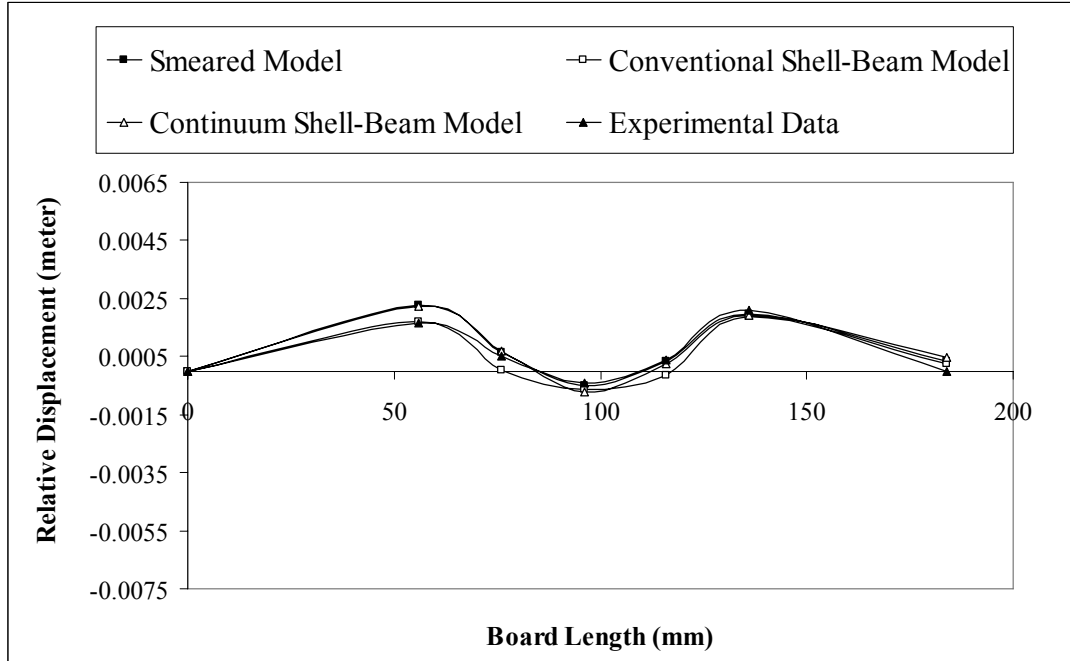


Figure 28 Correlation Between Experimental Relative Displacement of Board Assembly at 2.4 ms with Model Predictions under zero-degree JEDEC drop-test.

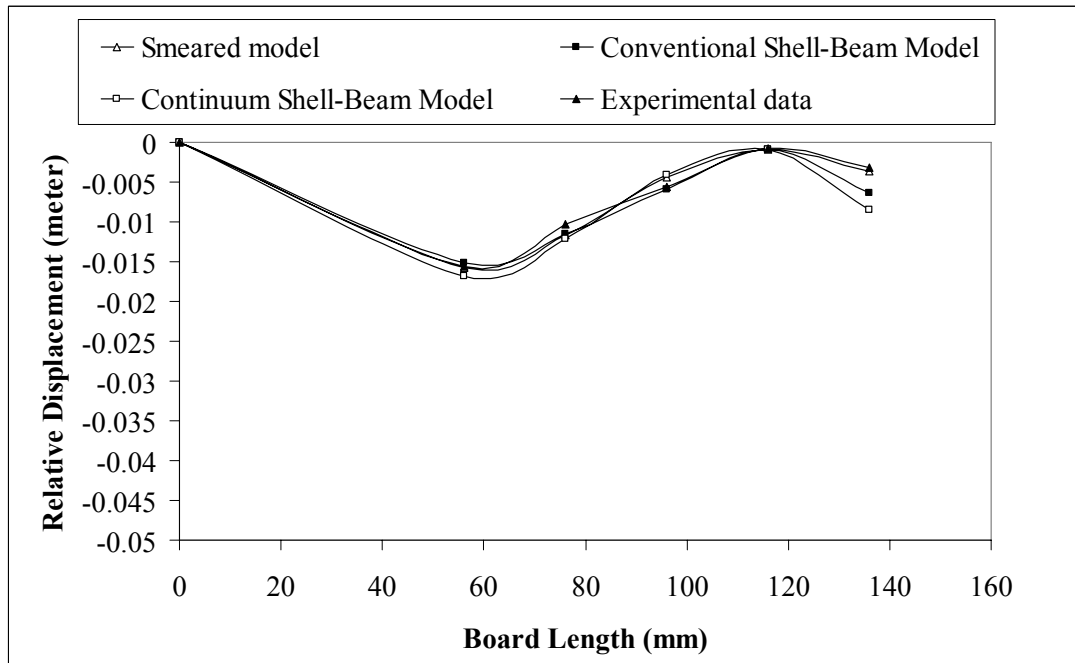


Figure 29 Correlation Between Experimental Relative Displacement of Board Assembly at 4.5 ms with Model Predictions under 90° free drop-test.

4.5 Error estimation in incorporating symmetry based models

When any electronic product is subject to drop impact, the orientation in which it may strike the impacting surface varies with each scenario. The use of symmetry-based models to represent this free drop would not account for the primary critical anti-symmetric mode shapes that dominate during impact. In case of the free vertical drop and the JEDEC drop simulations modeled in this paper, the stress and strain distributions experienced by the various solder interconnections in any package is not symmetrical. Figure 30 shows the variations in the stress distribution in the array of solder interconnections in the conventional shell-beam model subject to a JEDEC drop. If a diagonal slice model was used considering only the solder joints above Section AA based on the symmetry boundary conditions, the stresses in the top left and bottom right solder interconnections would be considered equal which is not true. This would result in an error of around 121% in the predicted value of the stress as shown in Table 17. Table 18 shows an error of about 107% in predicting the stresses in the solder interconnection in the continuum shell-beam model subject to free drop while incorporating a half symmetry model. The magnitude of errors clearly suggests that the use of diagonal slice models and half symmetry models for modeling drop simulations would be an inaccurate representation of the actual drop event.

4.6 Solder Interconnect Strain Histories in the Global Model

The strain distribution in the solder interconnections in both the conventional shell-Timoshenko beam model and the continuum shell-Timoshenko beam model for both free and JEDEC drop varies with the location of the interconnects in the assembly.

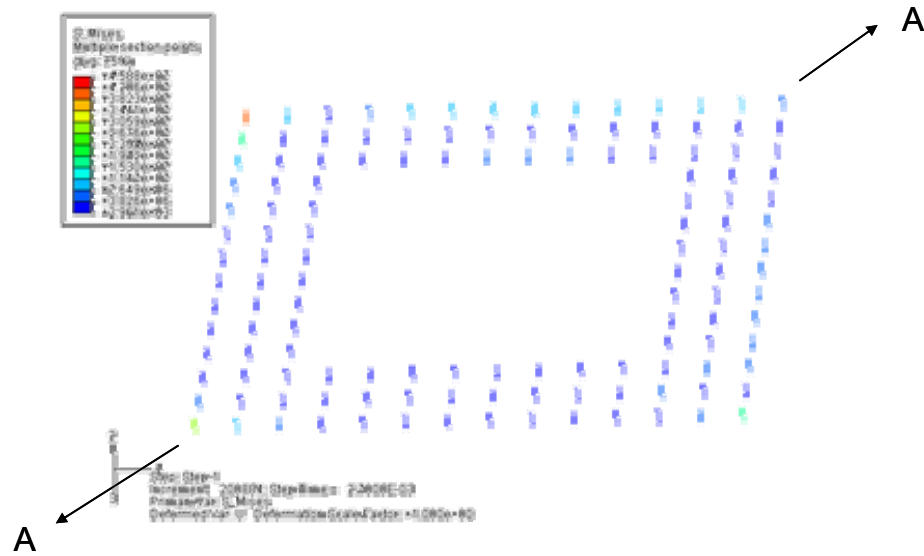


Figure 30 Stress distribution in the Timoshenko-beam solder interconnects subject to JEDEC drop for the conventional shell-beam model.

Table 17 Estimated error in prediction of solder interconnect stress in using diagonal symmetry model for conventional shell beam model subject to JEDEC Drop.

Model Prediction	Von Mises Stress (Pa) in Solder Interconnect	Error (%)
Full Model	1.887×10^7	-121.25
Diagonal Symmetry Model	4.175×10^7	

Table 18 Estimated error in prediction of solder interconnect stress in using half symmetry model for continuum shell-beam model subject to Free Drop.

Model Prediction	Von Mises Stress (Pa) in Solder Interconnect	Error (%)
Full Model	1.66098×10^7	-107
Half Symmetry Model	3.438×10^7	

Figure 32 and Figure 33 show the strain plots from the Timoshenko-Beam Element with Conventional-Shell model prediction for the solder interconnection located at the outermost corner of the package and in the solder interconnect located at the corner of the fourth-row from the outside, during a 90° free vertical drop.

Plots indicate that the transient strain history is very different at the four-corners of the chip-scale package. Therefore, the susceptibility of the solder interconnects to failure may be different in different corners. A comparison of transient strain histories in the solder interconnections at the corner of the package and the die shadow region reveals that, a large portion of the strain is carried by the outside row of the solder interconnects. This phenomenon can be observed at all the component locations for both conventional shell-Timoshenko beam model and the continuum shell-Timoshenko beam model for both free and JEDEC drops.

4.7 Explicit Sub-model for Drop Simulation

Sub-modeling can be described as a technique to study a local part of a model with a refined mesh based on interpolation of the solution of a relatively coarse, global model. It is generally used to obtain an accurate, detailed solution of a local region. Employing the sub-modeling technique includes running the global model and saving the results in the vicinity of the location of the sub-model boundary. The results from the global model are then interpolated onto the nodes on the appropriate parts of the boundary of the sub-model. The sub-model is then analyzed based on the solution of the global model to obtain the detailed response of the local region.

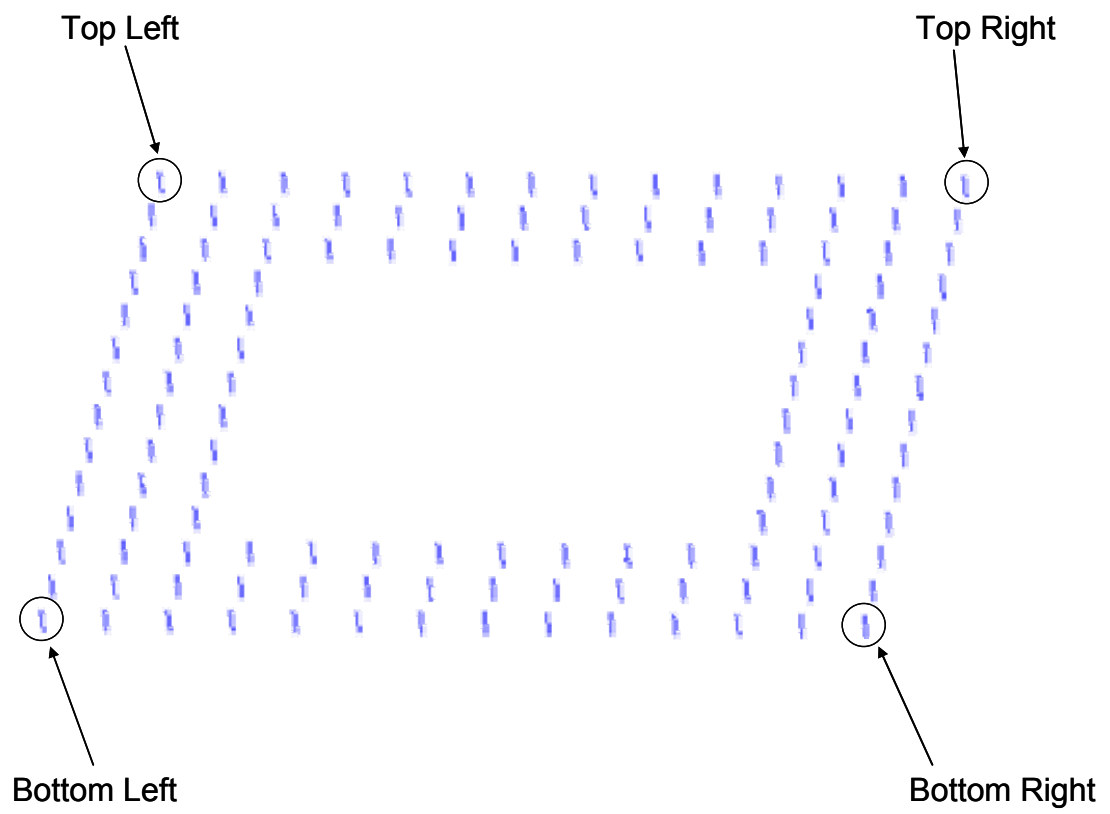


Figure 31 Representation of solder interconnection array.

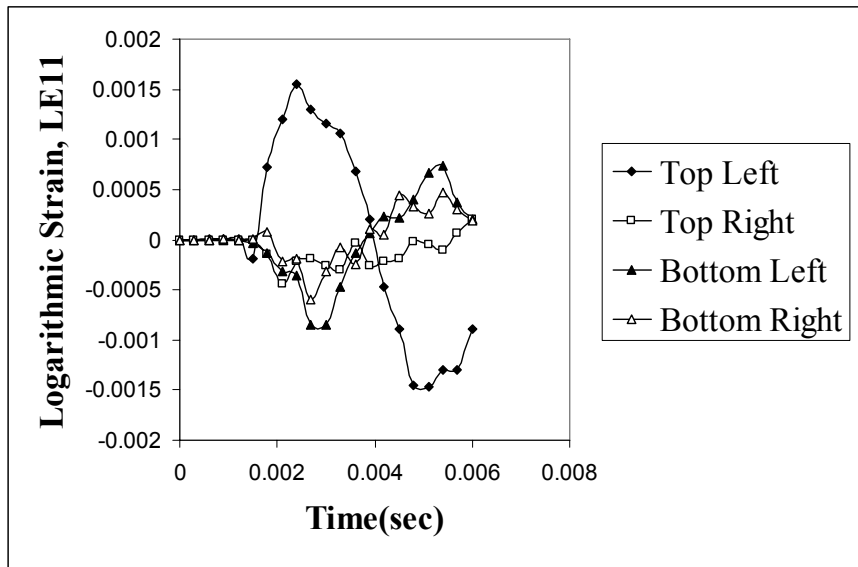


Figure 32 Timoshenko-Beam Element with Conventional-Shell Model Prediction of Transient Strain History at the Package Corner Solder Interconnects during 0° JEDEC-Drop.

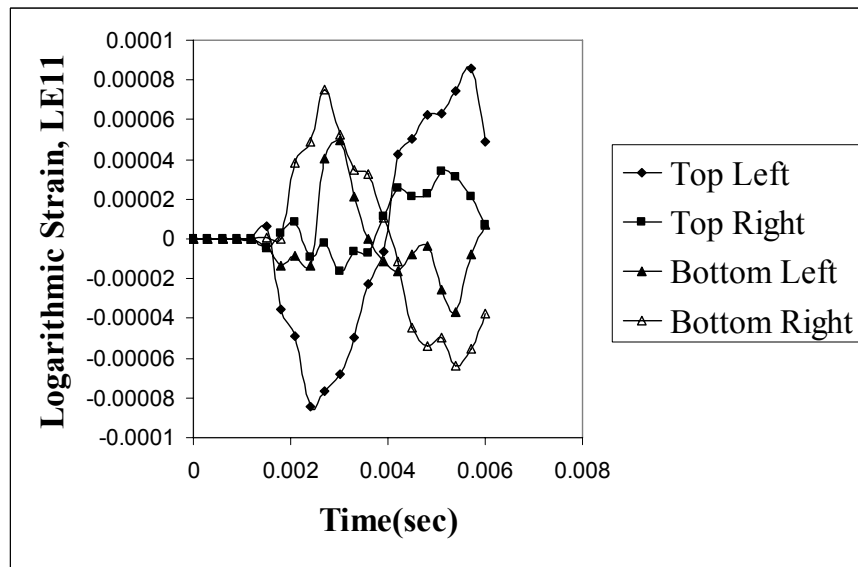


Figure 33 Timoshenko-Beam Element with Conventional-Shell Model Prediction of Transient Strain History in the Solder Interconnects Located in the Die Shadow region during 0° JEDEC-Drop.

The printed circuit board assembly consists of various layers such as the copper pad, solder interconnections, solder mask, silicon die etc. with multiple scale differences in their dimensions. Studying the stress/strain variations in the solder interconnections for failure prediction while at the same time capturing the dynamic response of the assembly would result in a very finely meshed model thereby increasing the computational time. To overcome these difficulties and achieve computational efficiency with reasonable accuracy, a global local or sub-modeling technique is employed to study the local critical part of the model with a refined mesh based on interpolation of the solution from an initial, relatively coarse global model. The advantage of this technique is that both the global and local models can be maintained sufficiently small in size thus requiring less computational time with reasonable accuracy. The sub-model consists of a detailed model located at the position of the critical package which is determined by the solution of the global model. It consists of the part of the printed circuit board modeled using first order reduced integration continuum solid elements (C3D8R), the individual layers of the package namely the copper pads, die attach, silicon die, substrate and the mold compound modeled using C3D8R elements and the solder interconnections modeled using a combination of Timoshenko beam elements (B31) and solid elements (C3D8R). The four corner solder interconnections, being the most critical, are modeled using the hexahedral solid elements (C3D8R) in order to obtain the detailed response in terms of stresses and strains for these interconnections. The remaining solder interconnections are modeled using the Timoshenko beam elements. Table 19 shows the various element formulations employed to model the explicit sub-model. Figure 34 shows the solder interconnection layout in the explicit sub-model with a combination of hexahedral-element corner

interconnects and Timoshenko-beam element interconnects. Figure 35 shows the cross-section of the explicit sub-model with the various individual layers such as the PCB, substrate, copper pad etc. Initial velocities are assigned to all the nodes of the various components of the local model. The location of the critical package as well as the critical solder joint can also be located based on the stress and/or strain distribution obtained from the global model prediction. Then the critical package is modeled as a local model with a fine mesh to capture the detailed distribution of stresses and strains of interconnects and the various individual layers.

4.8 Solder Interconnect Strain Histories in the Local Model

The global beam-shell model predictions indicate that a large portion of the strain is carried by the outside row of the solder interconnects. Therefore, the four corner solder interconnections, being the most critical, are modeled using the hexahedral solid elements (C3D8R) in order to obtain the detailed response in terms of stresses and strains for these interconnections. The remaining solder interconnections are modeled using the Timoshenko beam elements. Figure 36 and Figure 37 show the strain distributions in the solder joints in the local model at various time intervals. These local models were analyzed based on the global responses of the Conventional Shell-Timoshenko beam model subject to JEDEC drop and free vertical drop respectively. Both figures show that the strain distributions in the solder interconnections are not equal or symmetrical justifying the use of the full models.

Table 19 Element types used in the explicit sub-model.

Component	Element Type
PCB	C3D8R
Four Corner Solder Interconnections	C3D8R
Remaining Solder Interconnections	B31
Substrate	C3D8R
Copper Pad	C3D8R
Silicon Die	C3D8R
Die Attach	C3D8R
Mold Compound	C3D8R

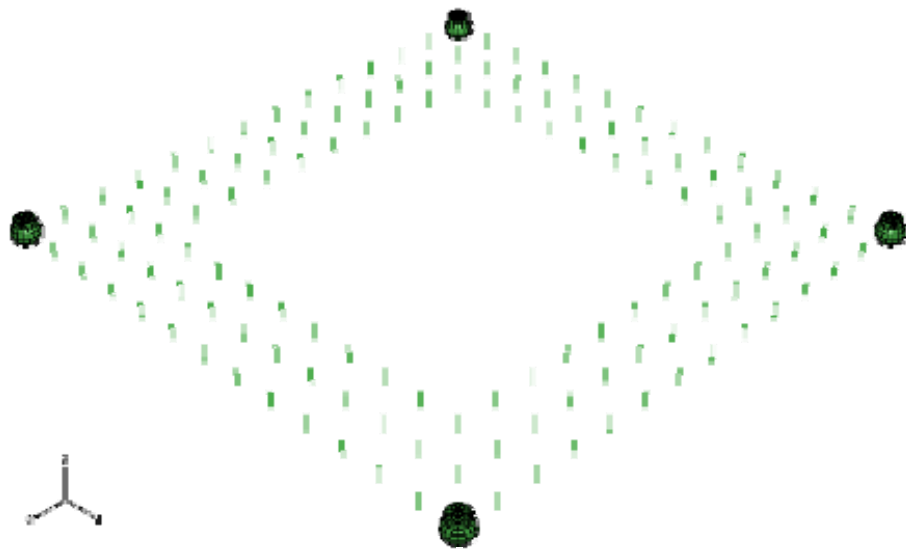


Figure 34 Solder Interconnection Layout in Explicit Sub-model with a combination Hexahedral-Element Corner Interconnects and Timoshenko-Beam Element Interconnects.

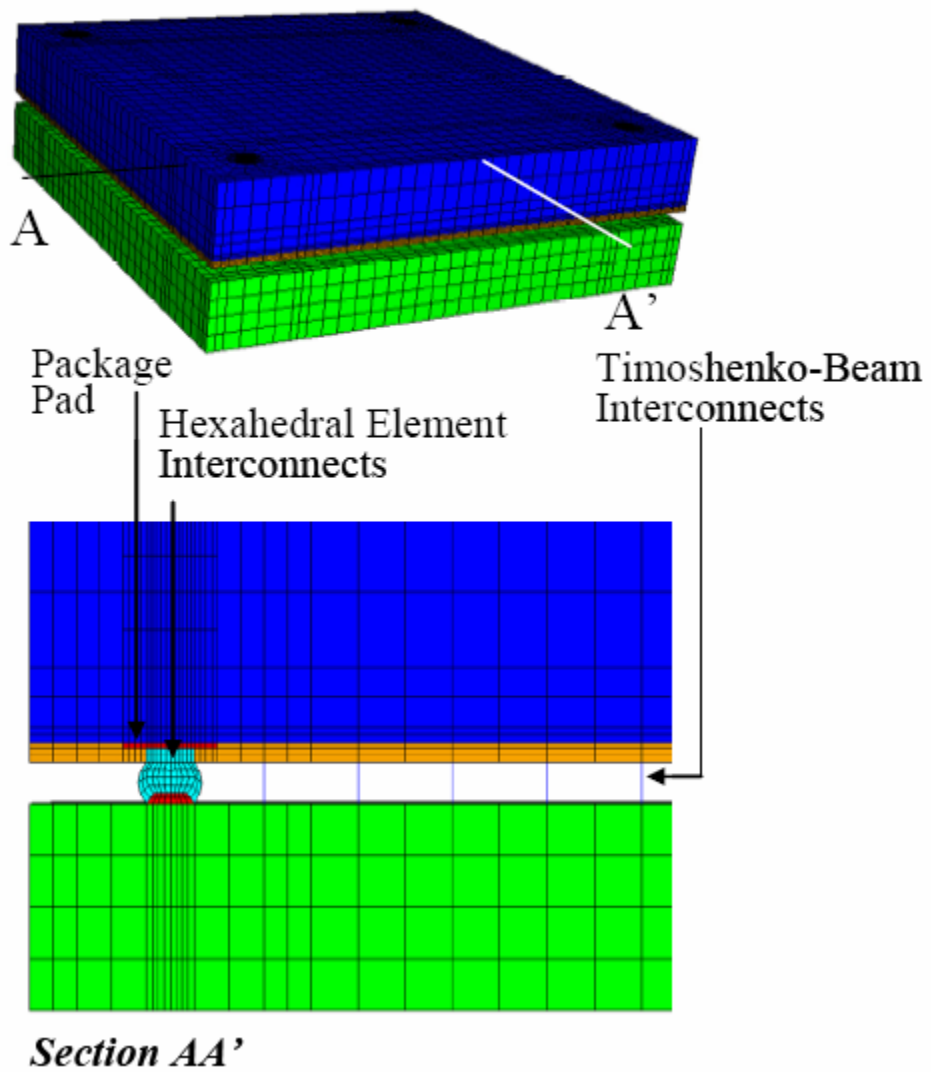


Figure 35 Local Explicit Sub-Model with Hexahedral-Element Corner Interconnects, Timoshenko-Beam Element Interconnects and PCB meshed with Hexahedral Reduced Integration-Elements.

The hexahedral element mesh solder interconnects provide insight into the logarithmic strain distributions in the solder interconnects. Figure 38 and Figure 39 show the explicit sub-model predictions of transient logarithmic shear strains, LE12 and LE23, in the solder interconnect of one of the chip-scale packages on the printed circuit board assembly corresponding to the Conventional Shell-Timoshenko Beam global model subject to JEDEC drop. Figure 40 and Figure 41 show the explicit sub-model predictions of transient logarithmic shear strains, LE12 and LE23, in the solder interconnect of one of the chip-scale packages on the printed circuit board assembly corresponding to the Continuum Shell-Timoshenko Beam global model subject to free drop. Model results indicate that the strains are maximum at the solder-joint to package interface and the solder-joint to printed circuit board interface, indicating a high probability of failure at these interfaces. Figure 42 shows the cross-section of corner solder interconnects in the failed samples showing higher susceptibility of the samples to fail at the package-to-solder interconnect interface or the solder-to-printed circuit board interface. Failure analysis of the samples reveals that the observed failure modes correlate well with the model predictions. Interface failure is generally observed in dynamic events such as drop impact due to the high strain rates experienced by the solder joints. The strength of the bulk solder increases with strain rate while that of the inter-metallic compounds decreases with strain rate. As a result, large stresses are developed at the solder joint interface leading to eventual failure.

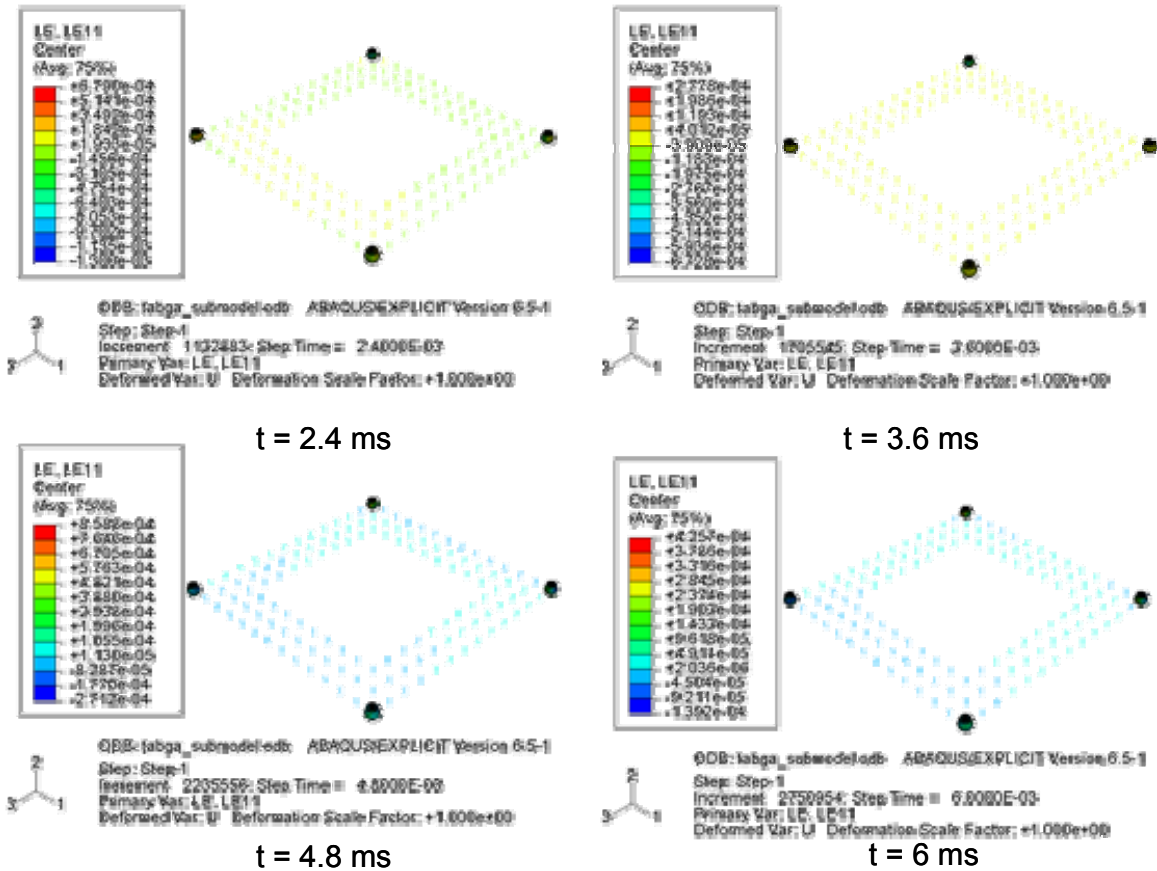


Figure 36 Strain histories in the local model corresponding to Conventional Shell Timoshenko-beam global model during JEDEC-drop at various time intervals.

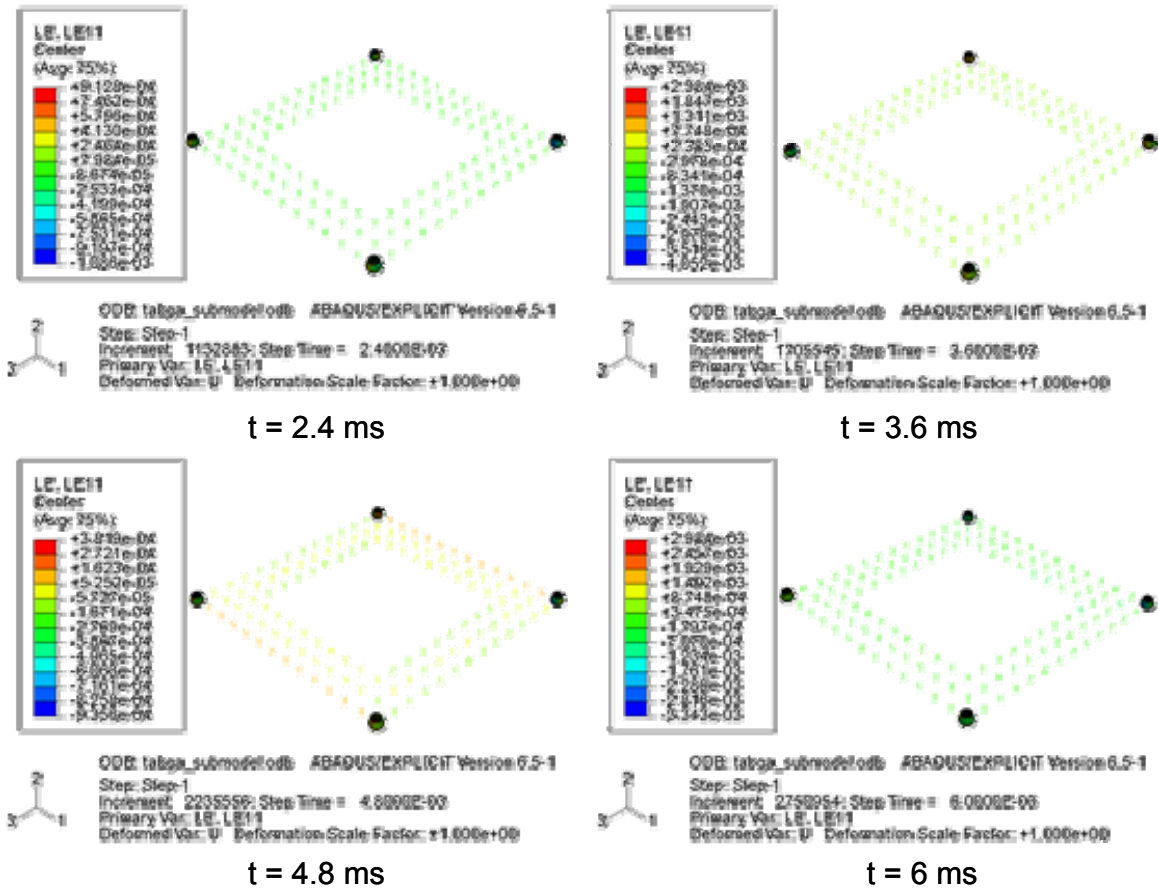


Figure 37 Strain histories in the local model corresponding to Conventional Shell Timoshenko-beam global model during free vertical drop at various time intervals.

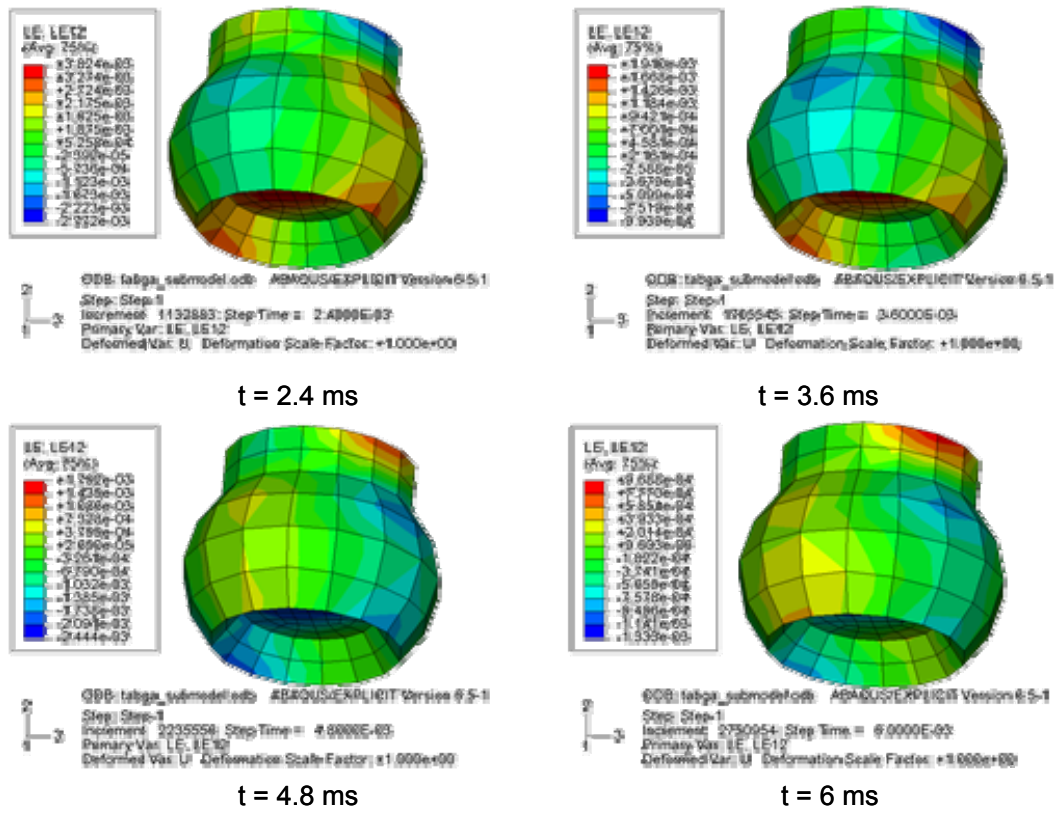


Figure 38 Global-Local Explicit Sub-Model Predictions of Transient Logarithmic Shear Strain, LE12, in the Solder Interconnect of one of the Chip-Scale Packages on the Printed Circuit Board Assembly during JEDEC Drop.

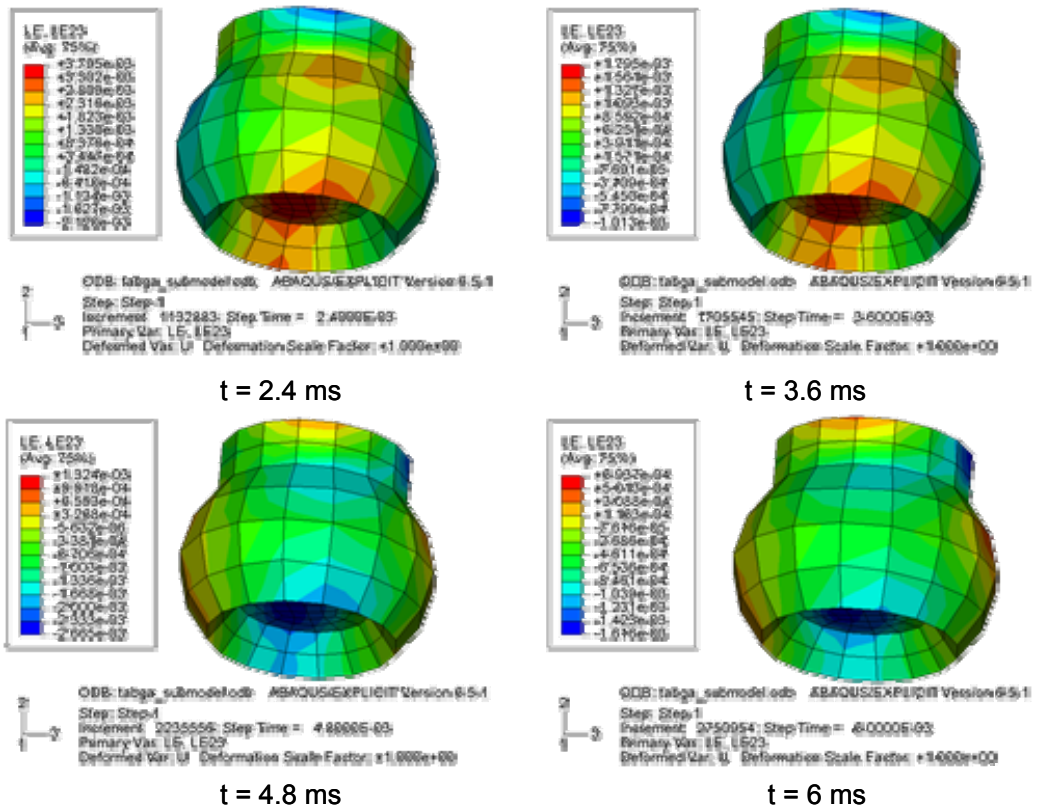


Figure 39 Global-Local Explicit Sub-Model Predictions of Transient Logarithmic Shear Strain, LE23, in the Solder Interconnect of one of the Chip-Scale Packages on the Printed Circuit Board Assembly during JEDEC Drop.

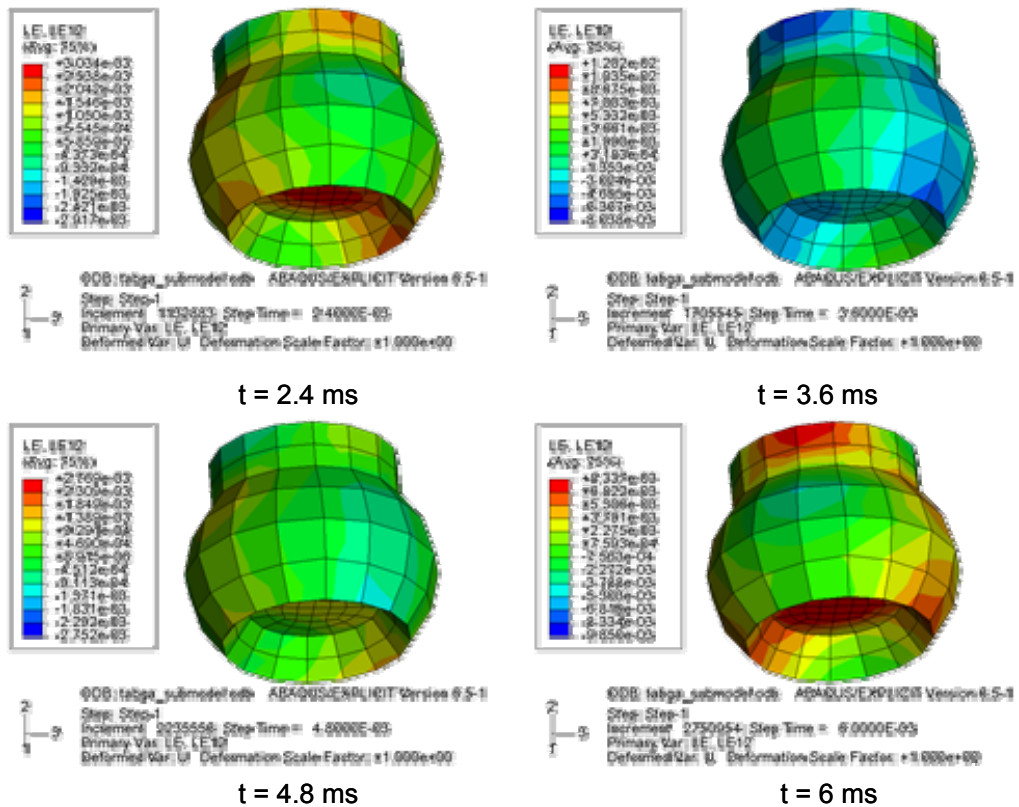


Figure 40 Global-Local Explicit Sub-Model Predictions of Transient Logarithmic Shear Strain, LE12, in the Solder Interconnect of one of the Chip-Scale Packages on the Printed Circuit Board Assembly during Free Drop.

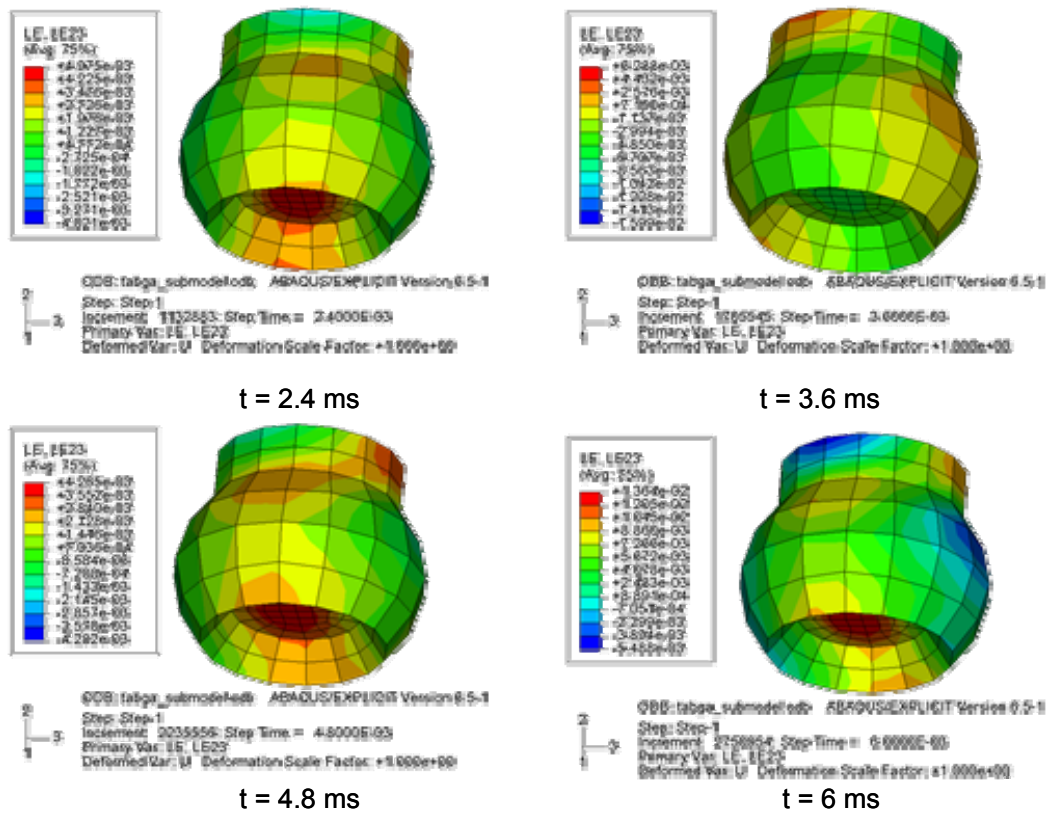


Figure 41 Global-Local Explicit Sub-Model Predictions of Transient Logarithmic Shear Strain, LE23, in the Solder Interconnect of one of the Chip-Scale Packages on the Printed Circuit Board Assembly during Free Drop.

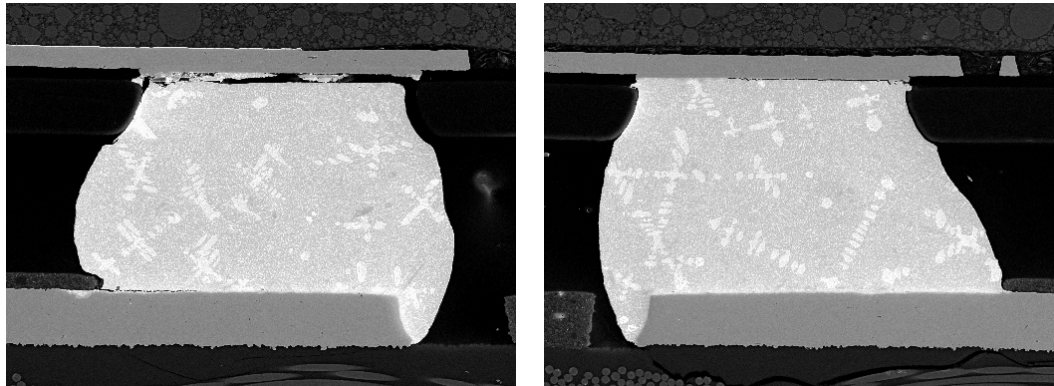


Figure 42 Cross-section of corner solder interconnect in the failed samples showing higher susceptibility of the samples to fail at the package-to-solder interconnect interface or the solder-to-printed circuit board interface.

4.9 Susceptibility to Chip Fracture

Figure 43 shows the contour plot of the stress, S_{33} in the silicon chip located in one of the components of the Conventional Shell-Timoshenko beam model subject to JEDEC drop at various time intervals. Figure 44 shows the transient stress history on the chip bottom-surface for chip-scale packages at two-locations on the test board. The stress, S_{33} varies in the range of 10 MPa. This is significantly smaller than the fracture stress of 7GPa published for silicon in [Petersen 1982, Pourahmadi et al. 1991], indicating a significant design margin of safety for chip-fracture during drop. In reality, the design margin can be reduced dramatically because of chip-surface imperfections.

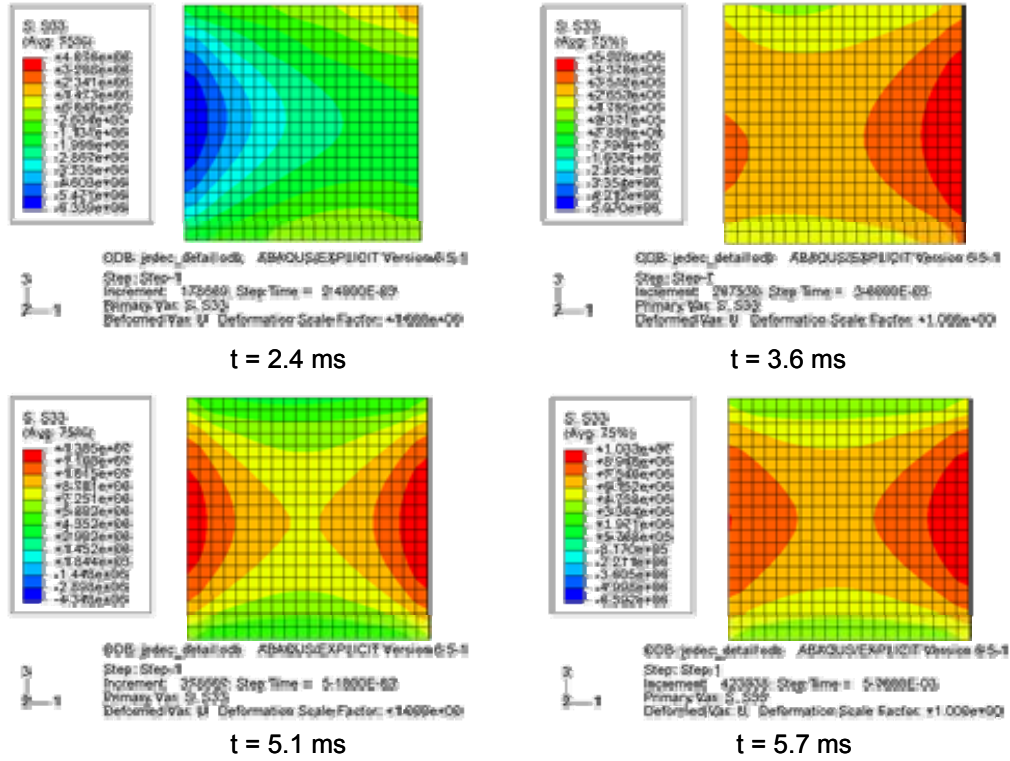


Figure 43 Transient stress history in the silicon chip.

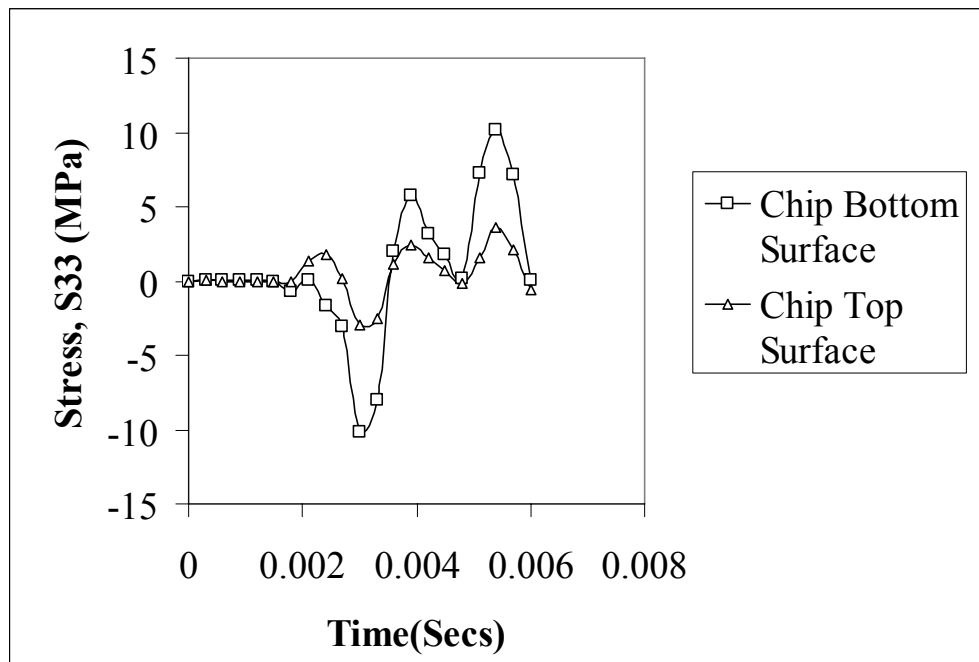


Figure 44 Transient Stress History in Chip Top and Bottom Surfaces.

CHAPTER 5
FAILURE PREDICTION MODELS

5.1 Overview

Brittle interfacial fracture failure at the solder joint-copper pad interface is commonly observed in first level solder interconnects of electronic products subject to high strain rates as in the case of impact loading. It has been observed that the fracture strength of the ductile bulk solder increases with increase in strain rate while that of the brittle inter-metallic compound (IMC) decreases with increase in strain rate. Two modeling approaches have been developed to investigate the failure mechanisms in the solder interconnections under drop impact namely the Timoshenko-Beam failure model and the cohesive zone modeling.

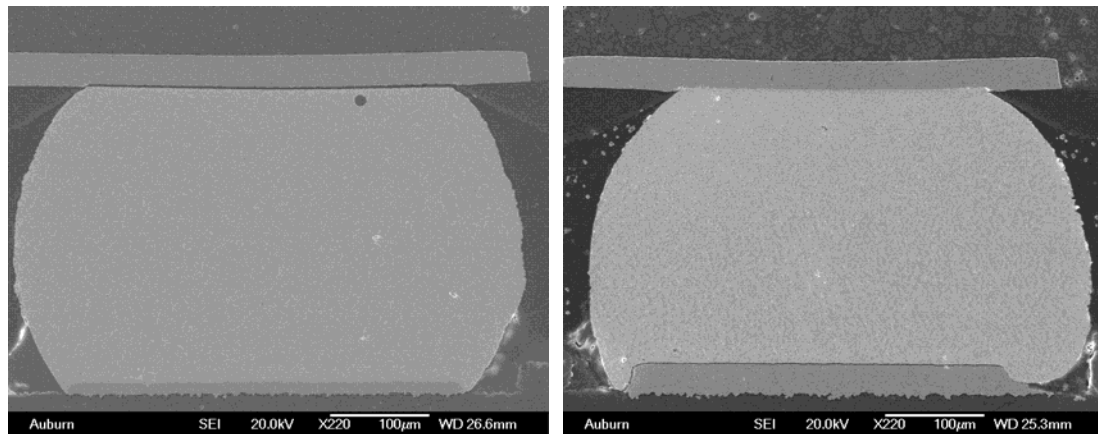


Figure 45 Brittle interfacial failure observed in the solder interconnections at the package side and the PCB side.

Tensile testing of solder joint arrays was carried out to study the interfacial failures in solder joints [Darveaux et al. 2006] on a mechanical testing machine as shown in Figure 46. Strain rates used in these tests ranged from 0.001/s to 1/s. Figure 47 shows the stress-strain response of the solder ball samples and the occurrence of both ductile and interface failures at various strain rates [Darveaux et al. 2006] For strain rates of 0.001/s and 0.01/s, the solder joint exhibits ductile behavior. The load reaches a peak, and then it decreases slowly as the joints start to neck down and the load bearing area is reduced. The value of the inelastic tensile strain at which interface failure occurs at a strain rate of 1.0/sec is around 0.1 [Darveaux et al. 2006]. The strain rate of 1.0/sec was considered to closely approximate the strain rates experienced by the solder joints during actual drop impact.

5.2 Timoshenko-Beam Failure Model

In the Timoshenko-Beam Failure model, a failure model available in commercial finite element code ABAQUS was used to predict the failure in the solder interconnections in the conventional shell-Timoshenko beam global model and the explicit sub-model. The solder joint constitutive behavior has been characterized with an elastic-plastic response with a yield stress of 60-95 MPa [Darveaux et al. 2006]. The failure model is based on the value of the equivalent plastic strain at element integration points and is suitable for high strain-rate dynamic problems. Failure is assumed to occur when the damage parameter exceeds 1.

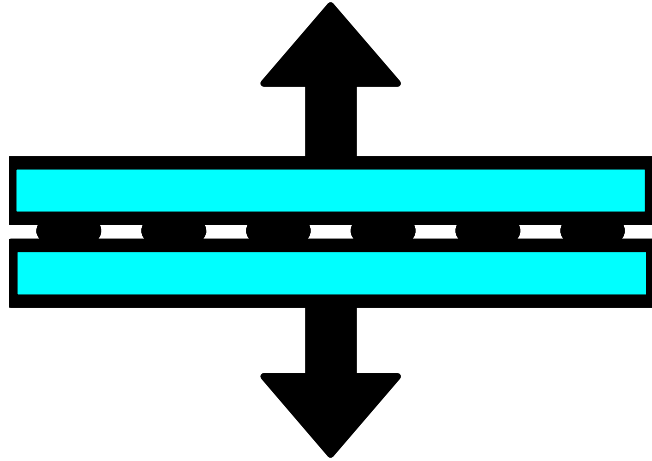


Figure 46 Solder joint array tensile test configuration [Darveaux et al. 2006].

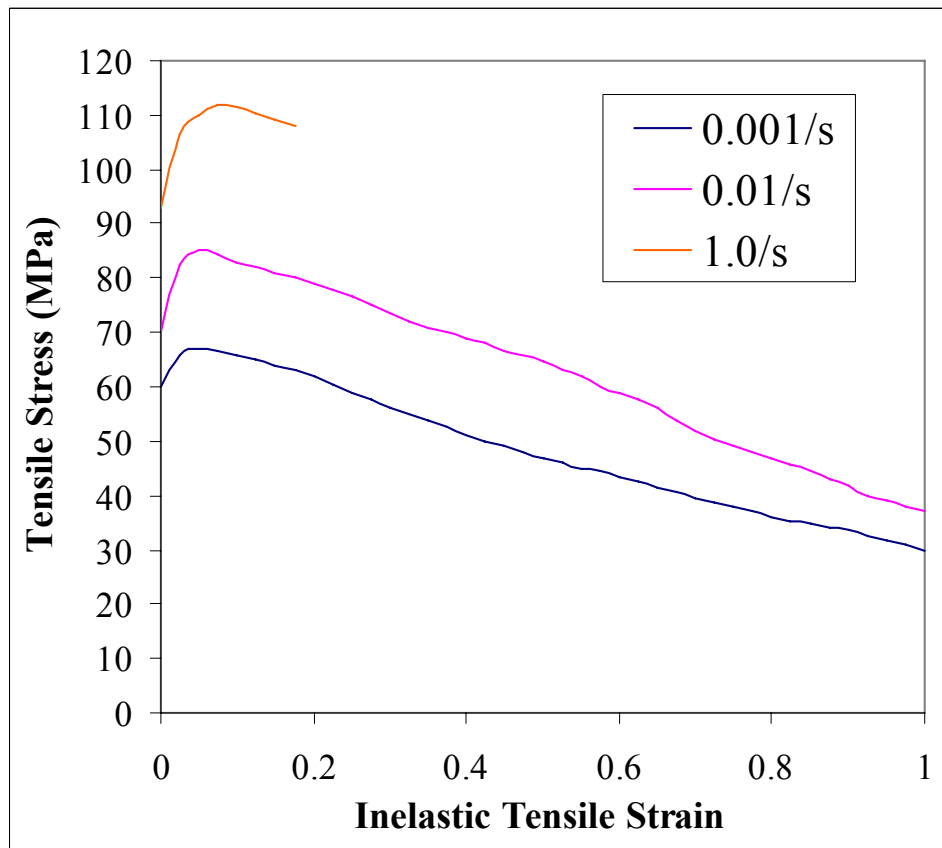


Figure 47 Stress-Strain response of solder ball sample subject to tensile loading at various strain rates [Darveaux et al. 2006].

The damage parameter is given by [Abaqus 2006a]:

$$\omega = \frac{\bar{\varepsilon}_0^{\text{pl}} + \sum \Delta \bar{\varepsilon}^{\text{pl}}}{\bar{\varepsilon}_f^{\text{pl}}}$$

where $\bar{\varepsilon}_0^{\text{pl}}$ is the initial value of equivalent plastic strain, $\Delta \bar{\varepsilon}^{\text{pl}}$ is an increment of the equivalent plastic strain, $\bar{\varepsilon}_f^{\text{pl}}$ is the strain at failure and the summation is performed over all increments in the analysis. The inelastic tensile strain value at interfacial failure for the tensile test carried out at 1.0/s was observed to be around 0.1 [Darveaux et al. 2006]. This critical strain value is specified as the equivalent plastic strain value at failure in the Timoshenko-Beam failure model and is used to simulate the failure of the solder interconnections most susceptible to failure. When the failure criterion is met at an integration point, all the stress components will be set to zero and that material point fails and the element is removed from the mesh. The critical plastic equivalent strain value is obtained by carrying out solder joint array tensile testing of BGA packages at high strain rates on a mechanical testing machine [Darveaux et al. 2006]. The failure model can be used to limit subsequent load-carrying capacity of the beam element once the prescribed stress limit is reached and result in deletion of the solder interconnection from the mesh.

5.3 Cohesive Zone Failure Model

Brittle interfacial fracture failure at the solder joint-copper pad interface at either component side or PCB side is commonly observed in solder interconnects of electronic products subject to high strain rates as in the case of impact loading [Tee et al. 2003, Chai et al. 2005]. The crack path for interface failure is usually in or very near the IMC layer formed between the solder alloy and the pad. It has been observed that the fracture

strength of the ductile bulk solder is proportional to strain rate while that of the brittle inter-metallic compound (IMC) decreases with increase in strain rate. Since the deformation resistance of the solder alloy increases with strain rate, high stresses are built up at the joint interfaces. Under these conditions, the solder joint interfaces can become the weakest link in the structure, and interface failure will occur [Bansal et al. 2005, Date et al. 2004, Wong et al., 2005, Newman 2005, Harada et al. 2003, Lall et al. 2005]. Abdul-Baqi [2005] simulated the fatigue damage process in a solder joint subjected to cyclic loading conditions using the cohesive zone methodology. A damage variable was incorporated to describe the constitutive behavior of the cohesive elements and supplemented by a damage evolution law to account for the gradual degradation of the solder material and the corresponding damage accumulation. Towashiraporn et. al. [2005] also predicted the crack propagation and fatigue life of solder interconnections subjected to temperature cycling. The cohesive zone modeling approach was also incorporated by Towashiraporn et. al. [2006] to predict solder interconnect failure during board level drop test in the horizontal direction.

In the present study, the cohesive zone modeling (CZM) methodology has been employed to study the dynamic crack initiation and propagation at the solder joint-copper pad interfaces leading to solder joint failure in PCB assemblies subject to drop impact. In this approach, the PCB drop is simulated in both horizontal zero-degree JEDEC drop and the ninety-degree free vertical drop orientations using the Conventional Shell-Timoshenko Beam global model. Based on the results of the global model, the critical package most susceptible to failure is determined and a detailed explicit sub-model is created at that location. A thin layer of cohesive elements is incorporated at the solder

joint-copper pad interfaces at both the component and PCB side of the solder interconnections in the explicit sub-model to study the interfacial fracture failure at these locations. Cohesive elements are placed between the continuum elements so that when damage occurs, they lose their stiffness at failure and the continuum elements are disconnected indicating solder joint failure. Elastic properties were assigned to the bulk solder material to relate stress and deformation without accounting for damage while the constitutive behavior of the cohesive elements was characterized by a traction-separation relationship derived from fracture mechanics to describe the mechanical integrity of the interface. The cohesive zone models are based on the relationship between the surface traction and the corresponding crack opening displacement. The traction-separation relations can be non-linear, based on Needleman's model [1987] or can be assumed to be linear in order to incorporate the cohesive elements available in ABAQUS [Abaqus 2006].

A) Needleman Model

The Needleman model [Needleman 1987] proposes a non-linear response of the cohesive zone embedded at the interface in terms of the traction separation relationship. The Needleman model has been successfully implemented [Scheider 2001] for crack propagation analyses of structures with elastic-plastic material behavior using cohesive zone models. The constitutive equation for the interface is such that, with increasing interfacial separation, the traction across the interface reaches a maximum, decreases, and eventually vanishes so that complete decohesion occurs. A similar response can be seen during the high strain rate tensile testing of solder joints [Darveaux 2006] where the tensile stress reaches the maximum value at the point of interfacial failure and then

decreases since there is no resistance to the force applied as a result of the decohesion of the solder joint-copper pad interface. Carroll, et. al. [2006] simulated the application of an uniaxial displacement to a solder joint at various strain rates and the stress-strain curves obtained show a similar response.

Consider an interface supporting a nominal traction field T which generally has both normal and shearing components. Two material points, A and B, initially on opposite sides of the interface, are considered and the interfacial traction is taken to depend only on the displacement difference across the interface, Δu_{AB} . At each point of the interface, we define the traction and the corresponding separation components as follows:

$$T = \begin{Bmatrix} T_n \\ T_t \\ T_b \end{Bmatrix}, \quad u = \begin{Bmatrix} u_n \\ u_t \\ u_b \end{Bmatrix}$$

such that [Needleman 1987]:

$$u_n = n \cdot \Delta u_{AB}, \quad u_t = t \cdot \Delta u_{AB}, \quad u_b = b \cdot \Delta u_{AB} \quad (1)$$

$$T_n = n \cdot T, \quad T_t = t \cdot T, \quad T_b = b \cdot T \quad (2)$$

The right-hand co-ordinate system comprising of the unit normal vectors n , t and b are chosen such that positive u_n corresponds to increasing interfacial separation and negative u_n corresponds to decreasing interfacial separation. The mechanical response of the interface is expressed in terms of a constitutive relation such that the tractions T_n , T_t and T_b depend on the separations u_n , u_t and u_b respectively. This response is specified in terms of a potential $\Phi(u_n, u_t, u_b)$ where [Needleman 1987]

$$\Phi(u_n, u_t, u_b) = - \int_0^u [T_n du_n + T_t du_t + T_b du_b] \quad (3)$$

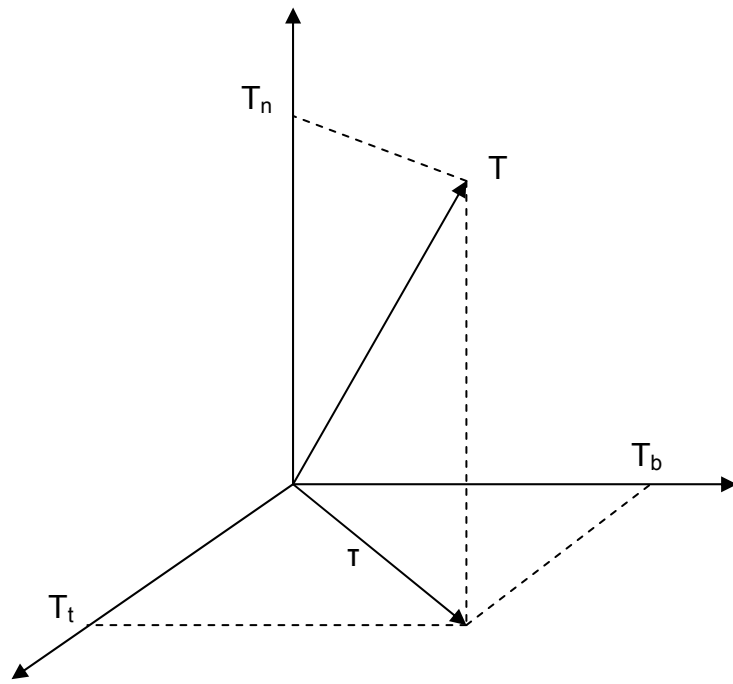


Figure 48 Traction components at the interface.

As the interface separates, the magnitude of the tractions increases, reaches a maximum, and ultimately falls to zero when complete separation occurs. Relative shearing across the interface leads to the development of shear tractions, but the dependence of the shear tractions on u_t and u_b is considered to be linear. The specific potential function used is

$$\Phi(u_n, u_t, u_b) = \frac{27}{4} \sigma_{\max} \delta \left\{ \begin{aligned} & \frac{1}{2} \left(\frac{u_n}{\delta} \right)^2 \left[1 - \frac{4}{3} \left(\frac{u_n}{\delta} \right) + \frac{1}{2} \left(\frac{u_n}{\delta} \right)^2 \right] \\ & + \frac{1}{2} \alpha \left(\frac{u_t}{\delta} \right)^2 \left[1 - 2 \left(\frac{u_n}{\delta} \right) + \left(\frac{u_n}{\delta} \right)^2 \right] + \\ & \frac{1}{2} \alpha \left(\frac{u_b}{\delta} \right)^2 \left[1 - 2 \left(\frac{u_n}{\delta} \right) + \left(\frac{u_n}{\delta} \right)^2 \right] \end{aligned} \right\} \quad (4)$$

for $u_n \leq \delta$, where σ_{\max} is the maximum traction carried by the interface undergoing a purely normal separation ($u_t \equiv 0$, $u_b \equiv 0$), δ is a characteristic length and α specifies the ratio of shear to normal stiffness of the interface. The interfacial tractions are obtained by differentiating Equation (4) with respect to u_n , u_t and u_b to get T_n , T_t and T_b respectively.

$$T_n = -\frac{27}{4} \sigma_{\max} \left\{ \begin{aligned} & \left(\frac{u_n}{\delta} \right) \left[1 - 2 \left(\frac{u_n}{\delta} \right) + \left(\frac{u_n}{\delta} \right)^2 \right] + \alpha \left(\frac{u_t}{\delta} \right)^2 \left[\left(\frac{u_n}{\delta} \right) - 1 \right] + \\ & \alpha \left(\frac{u_b}{\delta} \right)^2 \left[\left(\frac{u_n}{\delta} \right) - 1 \right] \end{aligned} \right\} \quad (5)$$

$$T_t = -\frac{27}{4} \sigma_{\max} \left\{ \alpha \left(\frac{u_t}{\delta} \right) \left[1 - 2 \left(\frac{u_n}{\delta} \right) + \left(\frac{u_n}{\delta} \right)^2 \right] \right\} \quad (6)$$

$$T_b = -\frac{27}{4} \sigma_{\max} \left\{ \alpha \left(\frac{u_b}{\delta} \right) \left[1 - 2 \left(\frac{u_n}{\delta} \right) + \left(\frac{u_n}{\delta} \right)^2 \right] \right\} \quad (7)$$

for $u_n \leq \delta$ and $T_n \equiv T_t \equiv T_b \equiv 0$ when $u_n \geq \delta$

Similarly, Needleman [1990] proposed a traction-separation law using an exponential potential of the form:

$$\phi(u_n, u_t) = \frac{9}{16} \sigma_{\max} \delta \left\{ 1 - \left[1 + z \left(\frac{u_n}{\delta} \right) - \frac{1}{2} \alpha z^2 \left(\frac{u_t}{\delta} \right)^2 \right] \right\} \exp \left[-z \left(\frac{u_n}{\delta} \right) \right] \quad (8)$$

where $z = 16e/9$ with $e = \exp(1)$

The interfacial tractions are given by:

$$T_n = -\sigma_{\max} e \left\{ z \left(\frac{u_n}{\delta} \right) - \frac{1}{2} \alpha z^2 \left(\frac{u_t}{\delta} \right)^2 \right\} \exp \left[-z \left(\frac{u_n}{\delta} \right) \right] \quad (9)$$

$$T_t = -\sigma_{\max} e \left\{ \alpha z \left(\frac{u_t}{\delta} \right) \right\} \exp \left[-z \left(\frac{u_n}{\delta} \right) \right] \quad (10)$$

Figure 49 shows the typical response of the normal traction across the interface as a function of u_n for both the polynomial potential and the exponential potential.

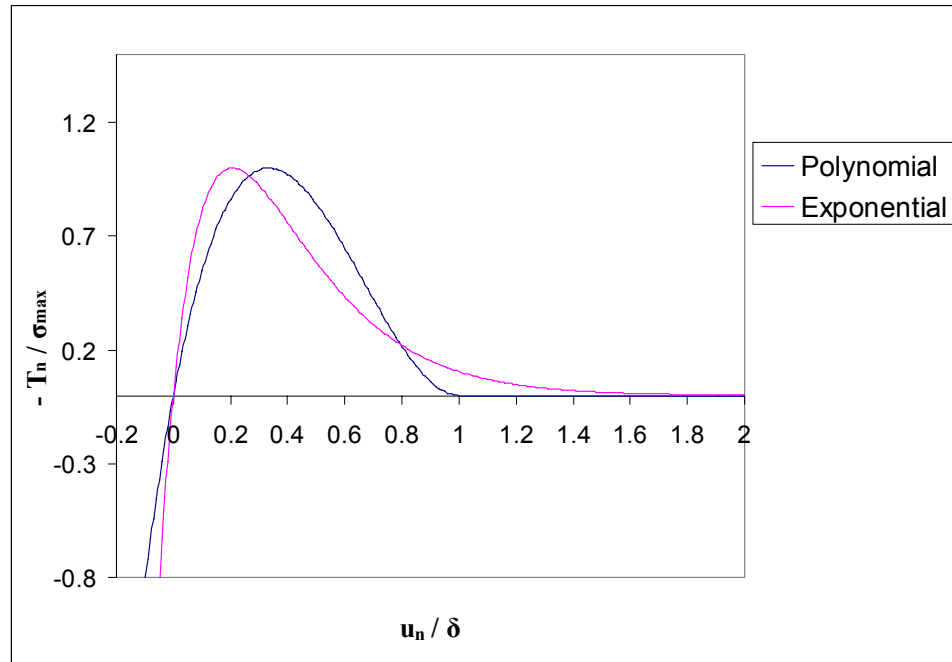


Figure 49 Normal traction as a function of u_n with $u_t \equiv 0$ [Needleman 1990].

Other traction-separation laws previously incorporated include the tri-linear traction-separation behavior proposed by Tvergaard & Hutchinson [1992] and the constant stress potential form [Schwalbe & Cornec, 1994] as shown in Figure 50.

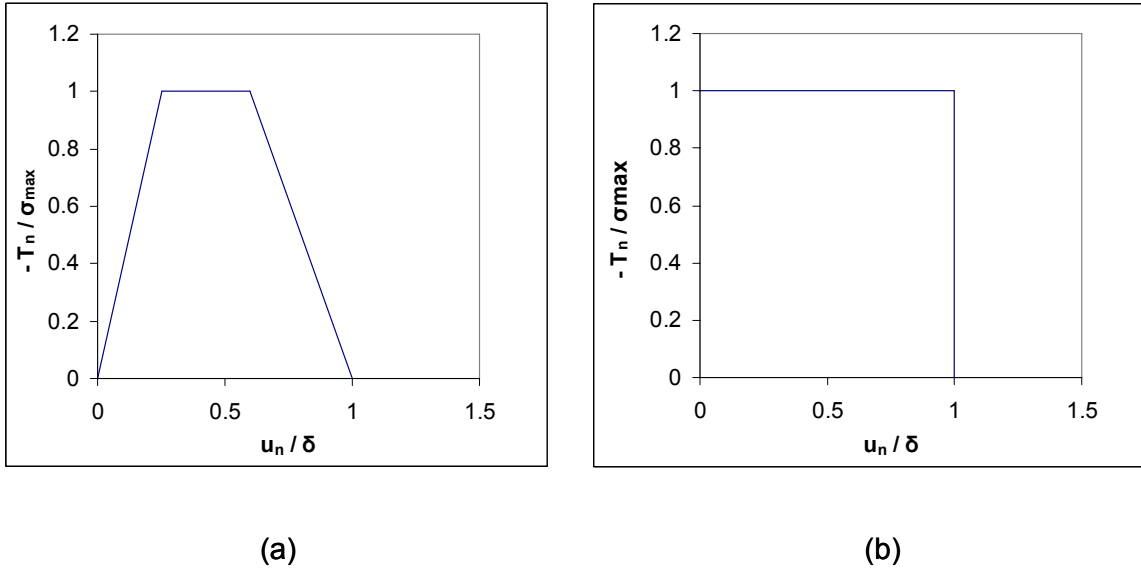


Figure 50 Different forms of Traction-Separation laws.

The polynomial potential of the Needleman model is generally preferred over the exponential form since it provides an analytically convenient traction-separation response such that the traction vanishes at a finite separation so that there is a well-defined decohesion point i.e. $T_n \equiv 0$ for $u_n \geq \delta$. The exponential potential, on the other hand, gives a continually decaying normal traction that vanishes in the limit $u_n \rightarrow \infty$. However, the work of separation done between $u_n = 0$ and $u_n = \delta$ for the exponential form is almost 95 % of work of separation for the polynomial form and hence there is no significant difference between the two forms.

The stiffness matrix for the cohesive element can be written as [Abdul-Baqi, et. al. 2005]:

$$K = \int_s [N]^T \left\{ \frac{\partial T}{\partial u} \right\} [N] dS \quad (11)$$

The nodal forces at the cohesive element are given as [Abdul-Baqi, et. al. 2005]:

$$f = \int_s [N]^T \{T\} dS \quad (12)$$

where N is the shape function and S is the cohesive zone area for the cohesive elements.

The cohesive zone model incorporated in this paper assumes a linear elastic traction-separation behavior is assumed at the interface before damage initiation occurs as shown in Figure 51. The cohesive zone parameters are provided to model include, the initial loading, damage initiation, damage propagation and eventual failure of the cohesive elements. Element failure is characterized by progressive degradation of the material stiffness driven by a damage process. Damage initiation refers to the beginning of degradation of the response of a material point. Damage initiation occurs when the stresses satisfy the specified quadratic nominal stress criterion given by [Abaqus 2006],

$$\left\{ \frac{(t_n)}{t_0^n} \right\}^2 + \left\{ \frac{(t_s)}{t_0^s} \right\}^2 + \left\{ \frac{(t_t)}{t_0^t} \right\}^2 = 1 \quad (13)$$

where t_0^n , t_0^s and t_0^t are the peak values of the nominal stress when the deformation is either purely normal to the interface or purely in the first or the second shear direction respectively.

The softening behavior of cohesive zone after the damage initiation criterion is satisfied is defined with the damage evolution law. The damage evolution law describes the rate at which the material stiffness is degraded once the corresponding initiation criterion is reached. The evolution of damage under a combination of normal and shear deformations can be expressed in terms of an effective displacement given by, [Abaqus 2006]

$$\delta = \sqrt{\delta_n^2 + \delta_s^2 + \delta_t^2} \quad (14)$$

The degradation of the material stiffness is specified in terms of the damage variable, D given by [Abaqus 2006]

$$D = \frac{\delta^f (\delta^{\max} - \delta^0)}{\delta^{\max} (\delta^f - \delta^0)} \quad (15)$$

where δ^{\max} is the maximum effective displacement achieved during the loading history and $\delta^f - \delta^0$ is the effective displacement at failure relative to the effective displacement at damage initiation. The scalar damage variable, D monotonically evolves from 0 to 1 upon further loading after the initiation of damage. When all the material points in the cohesive element reach the maximum damage variable, the traction between the surfaces no longer exists and the elements are deleted.

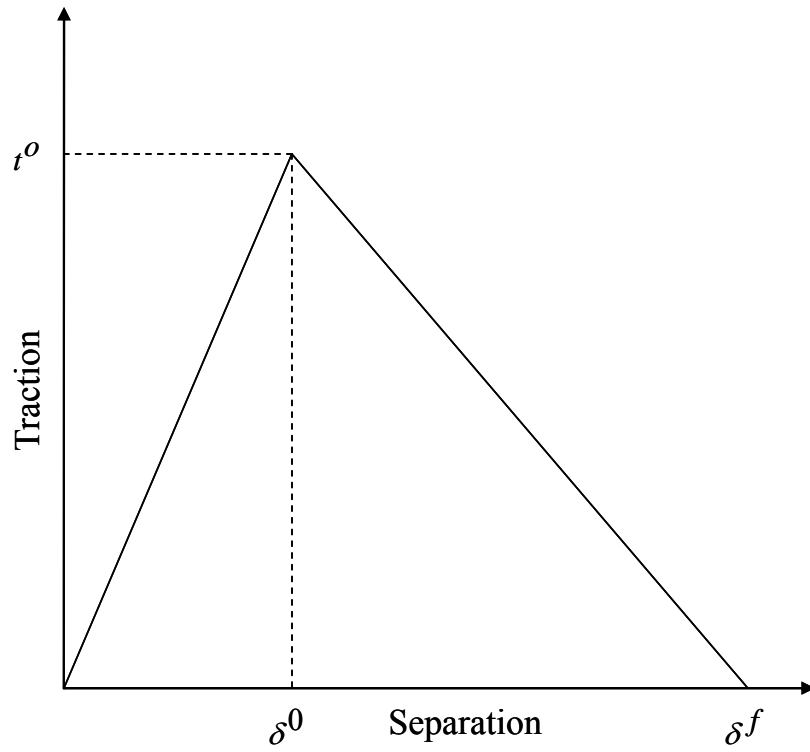


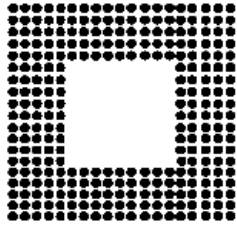
Figure 51 Linear Traction-Separation response for cohesive elements [Abaqus 2006].

5.4 Modeling Approach and Modeling Correlations

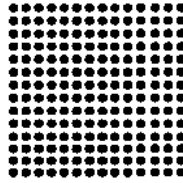
The test board used to study the reliability of chip-scale packages and ball-grid array includes 16mm flex-substrate chip scale packages with 0.5 mm pitch, 280 I/O, 15 mm, 196 I/O PBGA with 1 mm pitch, and 6mm, 64 I/O TABGA packages (Table 20). The dimensions of the test board are 8" × 5.5".

The Conventional-Shell with the Timoshenko-Beam Element model has been employed to create the global PCB assembly model. The PCB in the global model has been modeled using reduced integration shell elements (S4R) available in AbaqusTM. For each different type of element used for the PCB, the various component layers such as the substrate, die attach, silicon die, mold compound have been modeled with reduced integration solid elements (C3D8R). The concrete floor has been modeled using rigid R3D4 elements. Interconnects modeling has been investigated using two element types including the three-dimensional, linear, Timoshenko-beam element (B31) and the eight-node hexahedral reduced integration elements. Three-dimensional beams have six degrees of freedom at each node including, three translational degrees of freedom (1–3) and three rotational degrees of freedom (4–6). The rotational degrees of freedom have been constrained to model interconnect behavior.

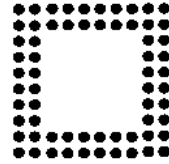
Test Vehicle



16 mm 280 I/O Flex BGA



15 mm 196 I/O PBGA



6 mm 64 I/O TABGA

Figure 52 Interconnect array configuration for Test Vehicle.

Table 20 Test Vehicle.

	16 mm Flex BGA	15 mm PBGA	6 mm TABGA
I/O	280	196	64
Solder Alloy	SAC 405	SAC 405	SAC 405
Ball Alignment	Perimeter	Full Grid	Perimeter
Pitch (mm)	0.8	1	0.5
Die Size (mm)	10	6.35	4
Substrate Thick (mm)	0.36	0.36	0.36
Pad Dia. (mm)	0.30	0.38	0.28
Substrate Pad	NSMD	SMD	NSMD
Ball Dia. (mm)	0.48	0.5	0.32

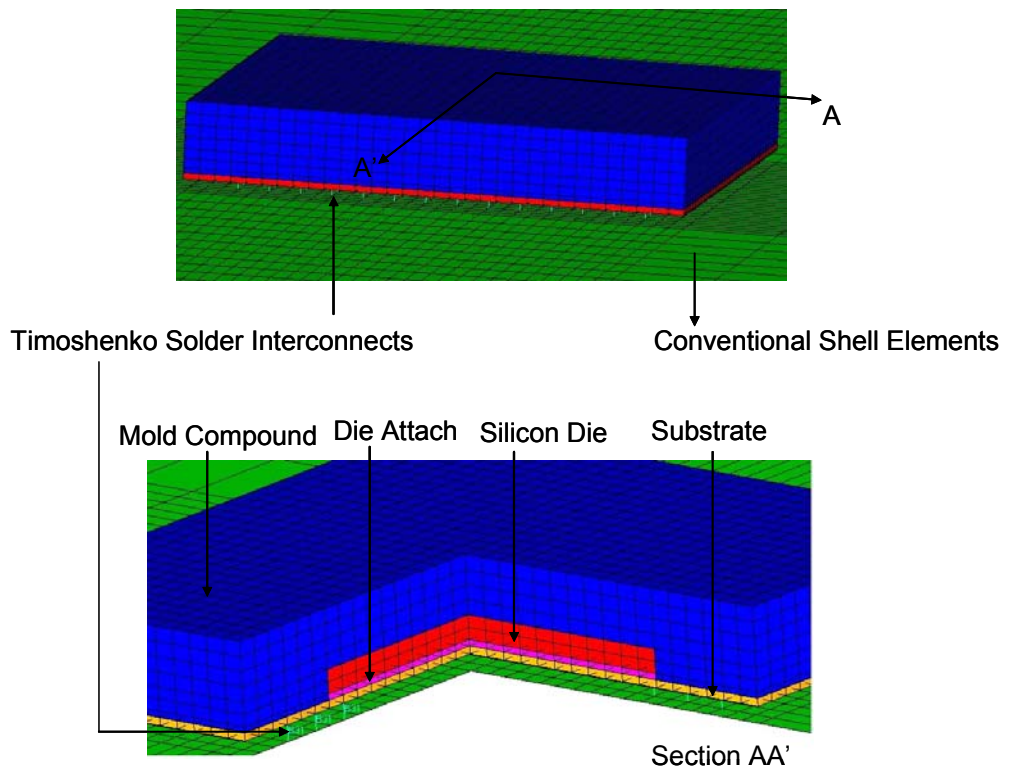


Figure 53 Printed-Circuit Assembly with Timoshenko-Beam Element Interconnects and Conventional Shell-Elements.

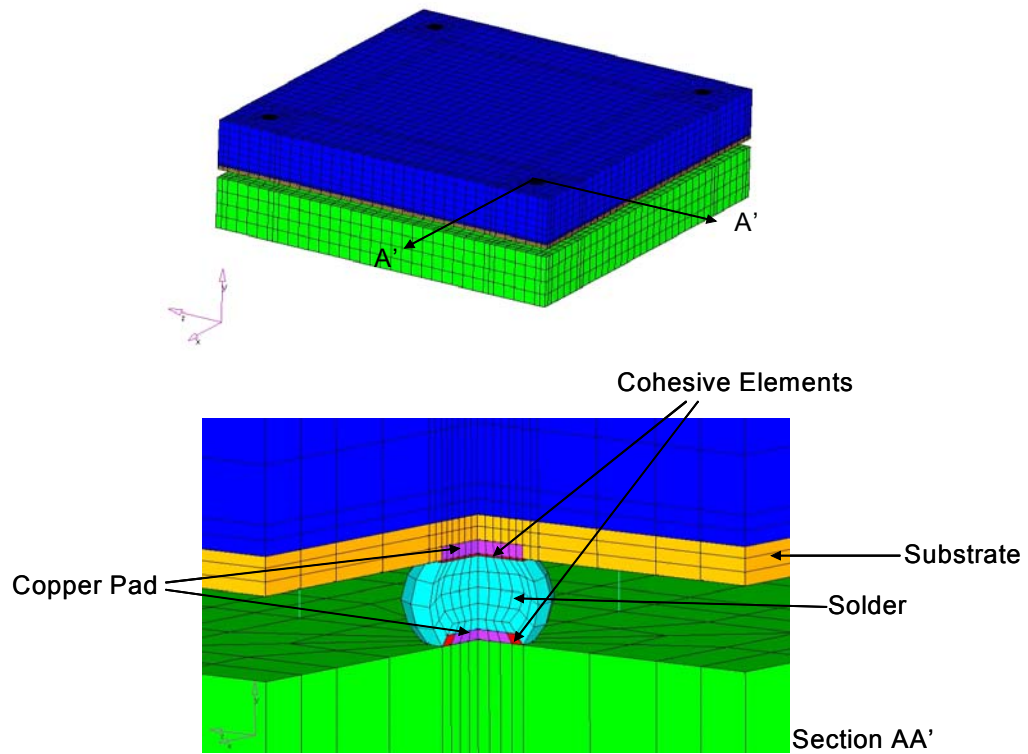


Figure 54 Explicit Sub-Model with Hexahedral-Element Corner Interconnects, Timoshenko-Beam Element Interconnects and PCB meshed with Hexahedral Reduced Integration-Elements with layer of cohesive elements at the solder joint-copper pad interface at both PCB and package side.

The drop orientation has been varied from 0° JEDEC-drop to 90° free vertical drop for the global model drop simulation. In case of free vertical drop, a weight has been attached on the top edge of the board. Node to surface contact has been employed between a reference node on the rigid floor and the impacting surface of the test assembly. Explicit sub-modeling has been accomplished using a local model, in addition to the global model. The explicit sub-model is created using a combination of Timoshenko-beam elements and reduced integration hexahedral elements to represent the corner interconnects. The local model is finely meshed and includes all the individual layers of the CSP and the corresponding PCB portion. The four corner solder interconnections are created using solid elements while the remaining solder joints are modeled using beam elements. A single layer of three dimensional cohesive elements (COH3D8) has been incorporated at the solder joint-copper pad interfaces. The constitutive response of the cohesive elements is based on a traction-separation behavior. Contact has been defined between the surfaces of the surrounding components to avoid potential contact once the cohesive elements have failed. Shell-to-solid sub-modeling technique has been employed to transfer the time history response of the global model to the local model. Displacement degrees of freedom from the global model are interpolated to the local model and applied as boundary conditions. The corresponding initial velocities for the respective drop orientation were assigned to all the components of the sub-model.

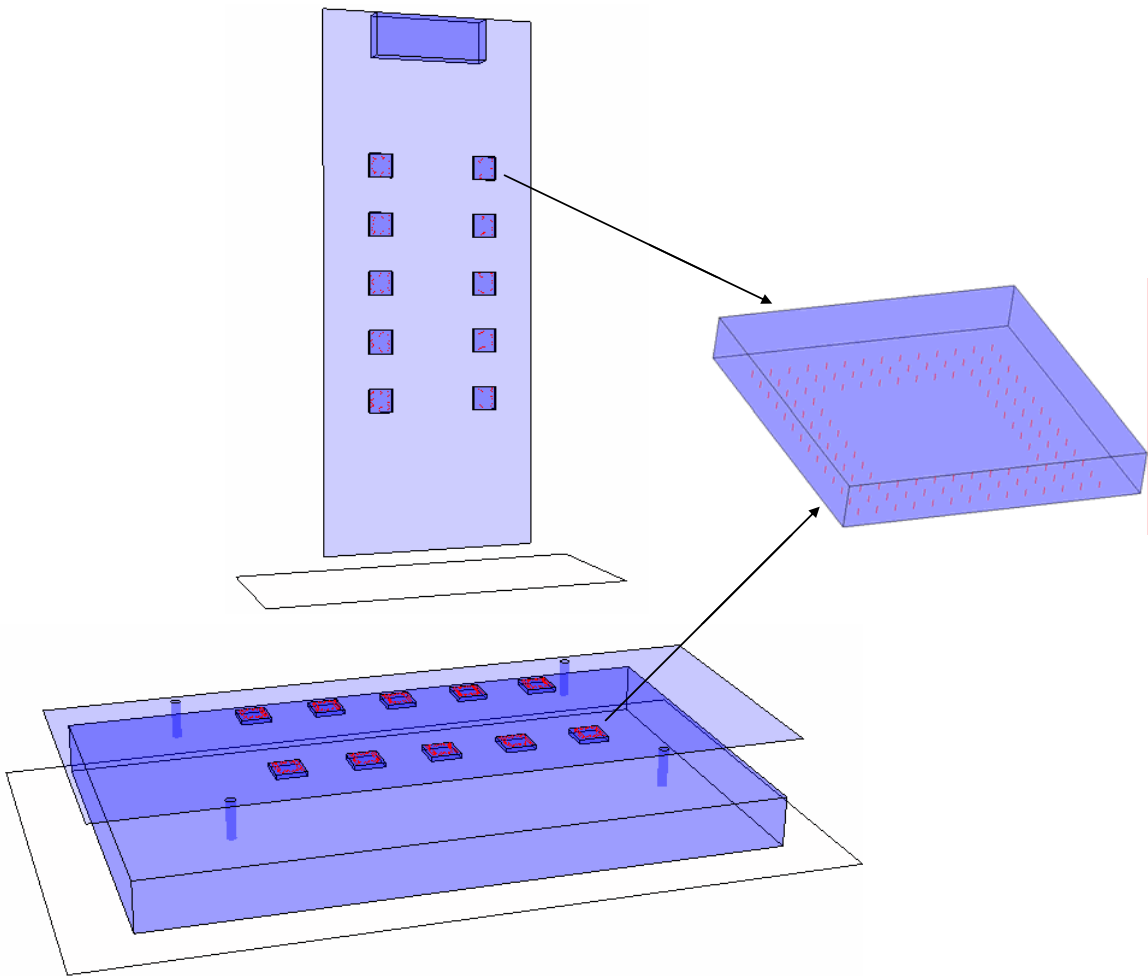
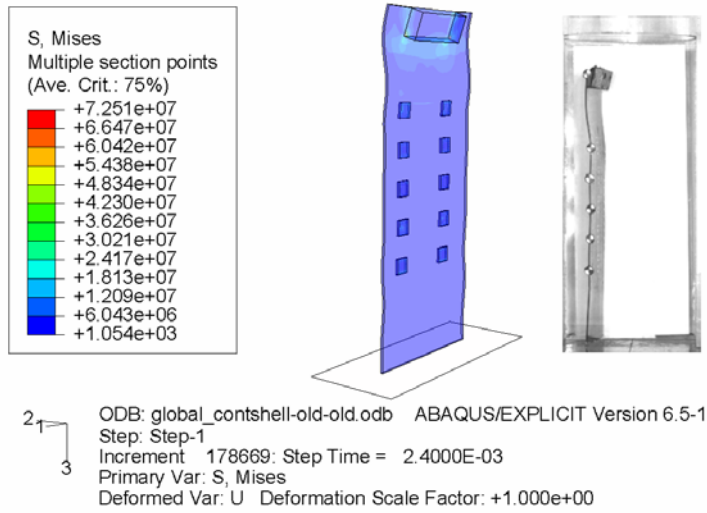


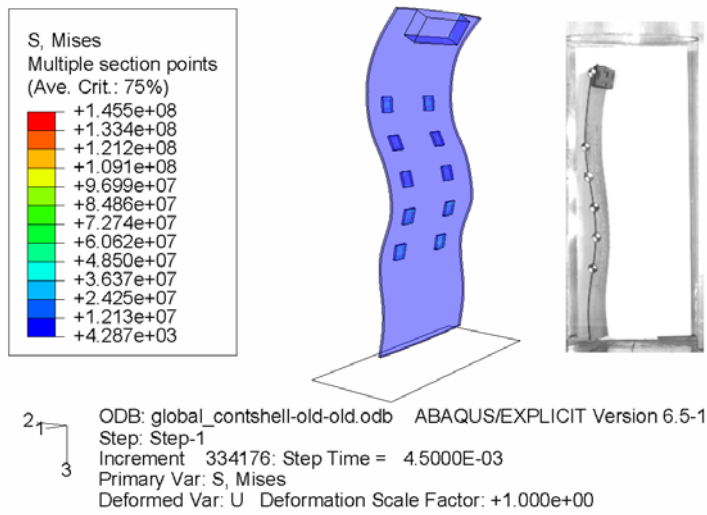
Figure 55 Drop-orientation has been varied from 0° JEDEC-drop to 90° free-drop.

Comparisons of field quantities and their derivatives such as the relative displacement and strain time histories respectively have been carried out between the Timoshenko-Beam Failure finite element model and the experimental data obtained from free drop and JEDEC drop. Additionally, the predicted transient mode shapes of the printed circuit board have been correlated with the observed experimental mode shapes. Figure 56 and Figure 57 show the transient mode shapes of the printed circuit board from high-speed video and explicit finite element simulation after impact for both free vertical drop and the horizontal JEDEC drop. The model predictions show good correlation with the experimentally observed mode shapes. Predicted values of peak relative displacement and peak strain obtained from the Timoshenko-Beam Failure model have been correlated with the experimental data. Results show errors of around 7-15% in the predicted values of peak relative displacement (Table 22) for JEDEC drop while the predicted peak strain values for free vertical drop and JEDEC drop exhibit errors in the region of around 27% and 22% (Table 21 and Table 23).

The predicted failure location in the electronic assembly has also been correlated with the experimentally observed failure location. The failure has been identified by high-speed data acquisition and location verified by cross-sectioning. Experimental data on failure location and model predictions of failure location are shown in Table 24 and Table 25. The dominant failure location in the interconnect array varies with the package location and the drop orientation. CSP location 5 exhibits a dominant failure location in the top left hand corner in JEDEC drop. The dominant failure location changes to top right-hand corner for 90° free drop.

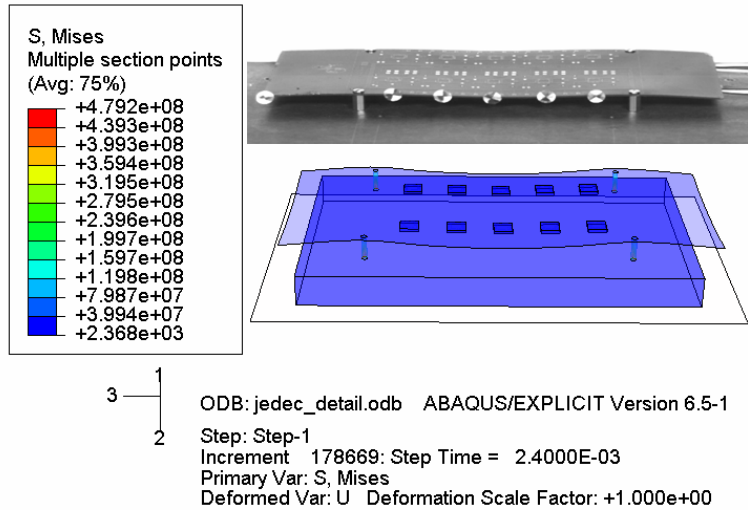


t = 2.4 ms

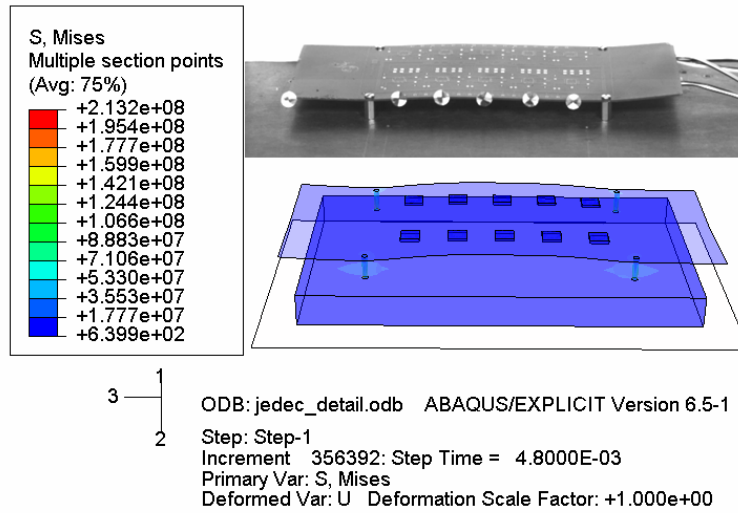


t = 4.5 ms

Figure 56 Correlation of Transient Mode Shapes during Free Drop.



t = 2.4 ms



t = 4.8 ms

Figure 57 Correlation of Transient Mode Shapes during JEDEC Drop.

Table 21 Correlation of Peak-Strain Values from Timoshenko-Beam Failure Model Predictions Versus Experiments for 90-degree Free-Drop.

	Loc	Loc	Loc
	1	3	5
Experiment	1417	2248	1667
Timoshenko-Beam Shell, Failure Model	1758	1628	1750
Error (%)	-24.07	27.58	-4.98

Table 22 Correlation of Peak Relative-Displacement Values with high-speed experimental data in zero-degree JEDEC Drop (mm).

	Loc	Loc	Loc
	1	3	5
Experiment (mm)	3.61	4.47	4.58
Timoshenko-Beam Shell, Failure Model	4.14	4.85	4.25
Error (%)	-14.68	-8.50	7.21

Table 23 Correlation of Peak-Strain Values from Model Predictions Versus Experiments for zero-degree JEDEC-Drop.

	Loc	Loc	Loc
	1	5	10
Experiment	312.5	337.5	331.25
Timoshenko-Beam Shell, Failure Model	245.01	269.45	338.09
Error (%)	21.59	20.16	-2.06

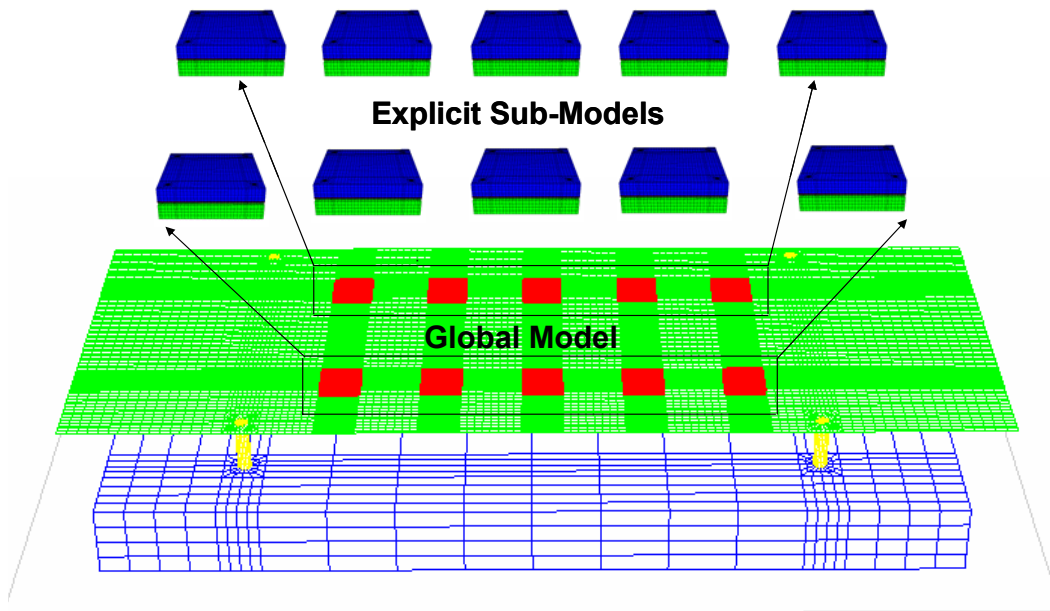


Figure 58 Explicit Sub-modeling technique employed at all component locations.

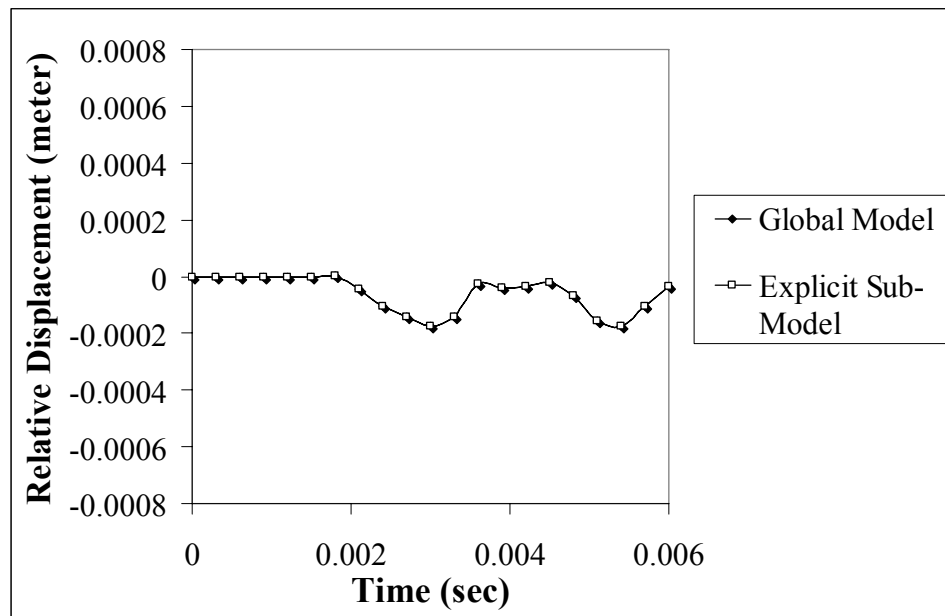


Figure 59 Time History of the displacement at the boundary nodes of the global model and the explicit sub-model.

Table 24 Correlation of Timoshenko-Beam Failure Model Predictions with Experimental data for solder interconnect failure location for JEDEC Drop.

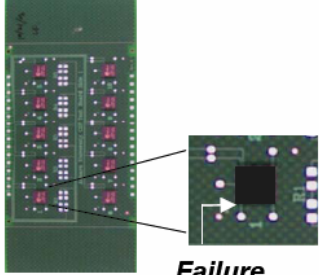
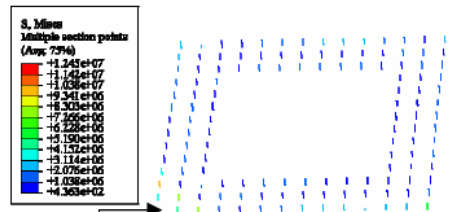
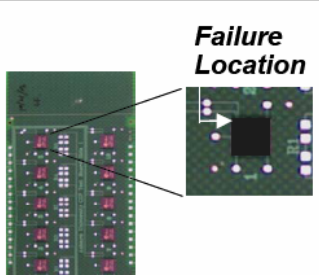
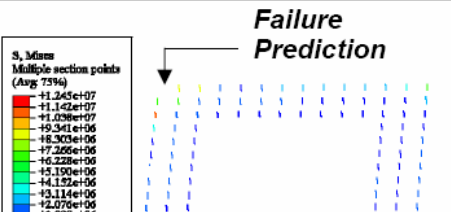
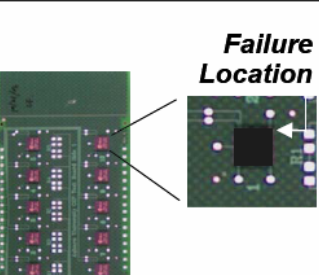
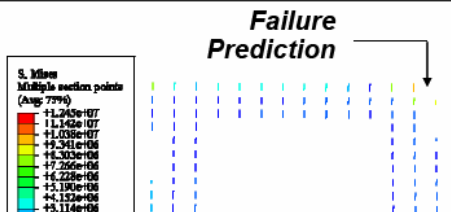
CSP Location	Experimental Location of Failure	Timoshenko Beam Failure Model Prediction
1	 <p>Failure Location</p>	 <p>Failure Prediction</p> <p>ODB: beam_failure.odb ABAQUS/EXPLICIT Version 6.5-1 Step: Step-1 Increment: 445253; Step Time = 6.0000E-03 Primary Var: S, Mises Deformed Var: U Deformation Scale Factor: +1.000e+00</p>
5	 <p>Failure Location</p>	 <p>Failure Prediction</p> <p>ODB: beam_failure.odb ABAQUS/EXPLICIT Version 6.5-1 Step: Step-1 Increment: 445253; Step Time = 6.0000E-03 Primary Var: S, Mises Deformed Var: U Deformation Scale Factor: +1.000e+00</p>
10	 <p>Failure Location</p>	 <p>Failure Prediction</p> <p>ODB: beam_failure.odb ABAQUS/EXPLICIT Version 6.5-1 Step: Step-1 Increment: 445253; Step Time = 6.0000E-03 Primary Var: S, Mises Deformed Var: U Deformation Scale Factor: +1.000e+00</p>

Table 25 Correlation of Timoshenko-Beam Failure Model Predictions with Experimental data for solder interconnect failure location for Free Drop.

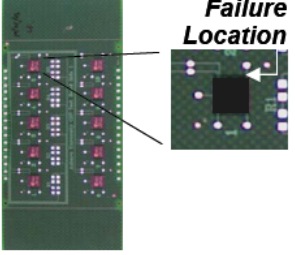
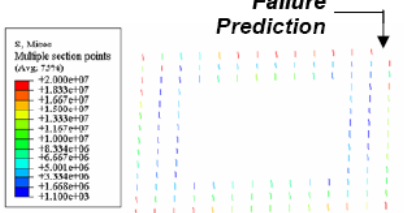
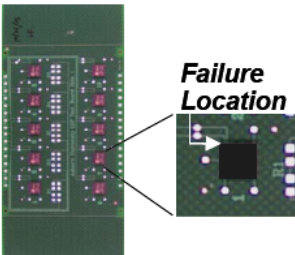
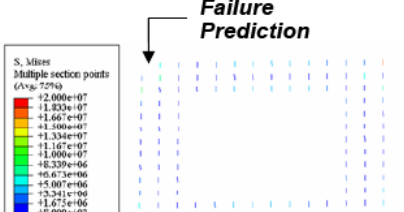
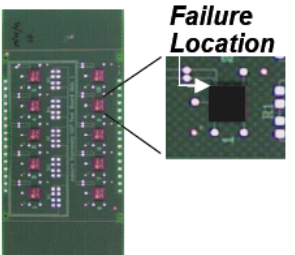
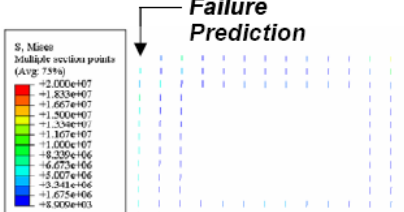
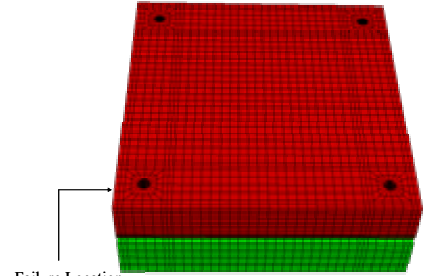
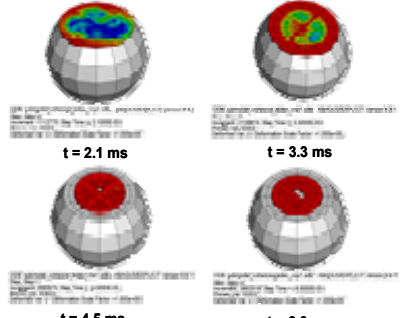
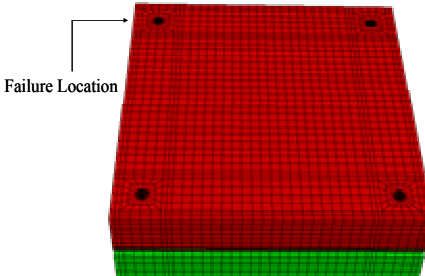
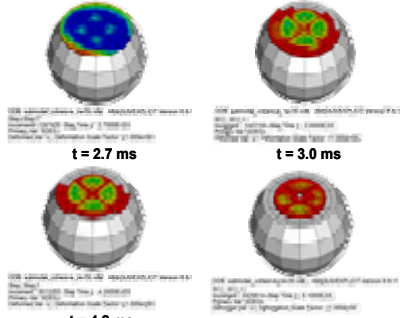
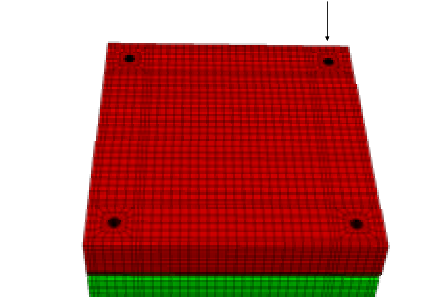
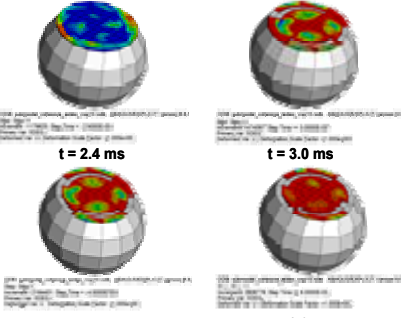
CSP Location	Experimental Location of Failure	Timoshenko Beam Failure Model Prediction
5	 <p>Failure Location</p>	 <p>Failure Prediction</p> <p>S, Mises Multiple section points (Avg: 72%)</p> <ul style="list-style-type: none"> +2.000e+07 +1.833e+07 +1.667e+07 +1.500e+07 +1.333e+07 +1.167e+07 +1.000e+07 +8.334e+06 +6.667e+06 +5.001e+06 +3.334e+06 +1.668e+06 +1.195e+03 <p>ODB: timoshenko_failure_free.odb ABAQUS/EXPLICIT Version 6.6-1 Step: Step-1 Increment: 24315; Step Time = 3.3000E-03 Primary Var: S, Mises Deformed Var: U Deformation Scale Factor: +1.000e+00</p>
7	 <p>Failure Location</p>	 <p>Failure Prediction</p> <p>S, Mises Multiple section points (Avg: 72%)</p> <ul style="list-style-type: none"> +2.000e+07 +1.833e+07 +1.667e+07 +1.500e+07 +1.334e+07 +1.167e+07 +1.000e+07 +8.339e+06 +6.673e+06 +5.007e+06 +3.341e+06 +1.675e+06 +8.909e+03 <p>ODB: timoshenko_failure_free.odb ABAQUS/EXPLICIT Version 6.6-1 Step: Step-1 Increment: 37860; Step Time = 5.1000E-03 Primary Var: S, Mises Deformed Var: U Deformation Scale Factor: +1.000e+00</p>
9	 <p>Failure Location</p>	 <p>Failure Prediction</p> <p>S, Mises Multiple section points (Avg: 73%)</p> <ul style="list-style-type: none"> +2.000e+07 +1.833e+07 +1.667e+07 +1.500e+07 +1.334e+07 +1.167e+07 +1.000e+07 +8.239e+06 +6.673e+06 +5.007e+06 +3.341e+06 +1.675e+06 +8.000e+03 <p>ODB: timoshenko_failure_free.odb ABAQUS/EXPLICIT Version 6.6-1 Step: Step-1 Increment: 37860; Step Time = 5.1000E-03 Primary Var: S, Mises Deformed Var: U Deformation Scale Factor: +1.000e+00</p>

Table 26 Correlation of Explicit Cohesive Sub-Model Predictions with Experimental data for solder interconnect failure location for Free Drop.

CSP Location	Experimental Location of Failure	Cohesive Zone Stress History at Failure Location
1	 <p>Failure Location</p>	 <p>t = 2.1 ms t = 3.3 ms t = 4.5 ms t = 6.0 ms</p>
5	 <p>Failure Location</p>	 <p>t = 2.7 ms t = 3.0 ms t = 4.2 ms t = 5.1 ms</p>
10	 <p>Failure Location</p>	 <p>t = 2.4 ms t = 3.0 ms t = 4.5 ms t = 6.0 ms</p>

In addition, CSP locations 1, 7, 9, 10 exhibit dominant failure locations at different array locations for the same drop orientation. Once the beams fail, they are deleted from the array in the simulation. The location of the missing beams in Table 24 and Table 25 show good correlation with location of failure from cross-sections. For some package location, simulation indicates failure of multiple beams, which also correlates with the cross-section results.

Figure 59 shows the excellent correlation between the displacement time history at the boundary nodes of the global model and the corresponding explicit sub-model thus ensuring that the results from the global model are accurately transferred on to the sub-model. Table 26 shows the progressive deletion of the cohesive elements at the solder joint-copper pad interface on the PCB side at various component locations once the maximum value of the damage variable is reached. This prediction clearly shows the susceptibility to failure of the IMC layer at the solder joint-copper pad interface subject to drop impact. The cohesive elements located at the outer periphery of the interface experience maximum stresses and are deleted first which is in accordance with the observations generally seen during failure analysis of the failed samples in that crack initiation generally starts from the outer boundary and progresses inward. Furthermore, the maximum or the peak value of the Von Mises stress in the cohesive elements predicted by the cohesive zone model approximately varies from 100 MPa to 280 MPa depending on component location and also on where the element is located along the solder joint-copper pad interface. The solder joint array pull experimental test carried out high strain rates also shows the value of the failure stress at the point of interfacial failure

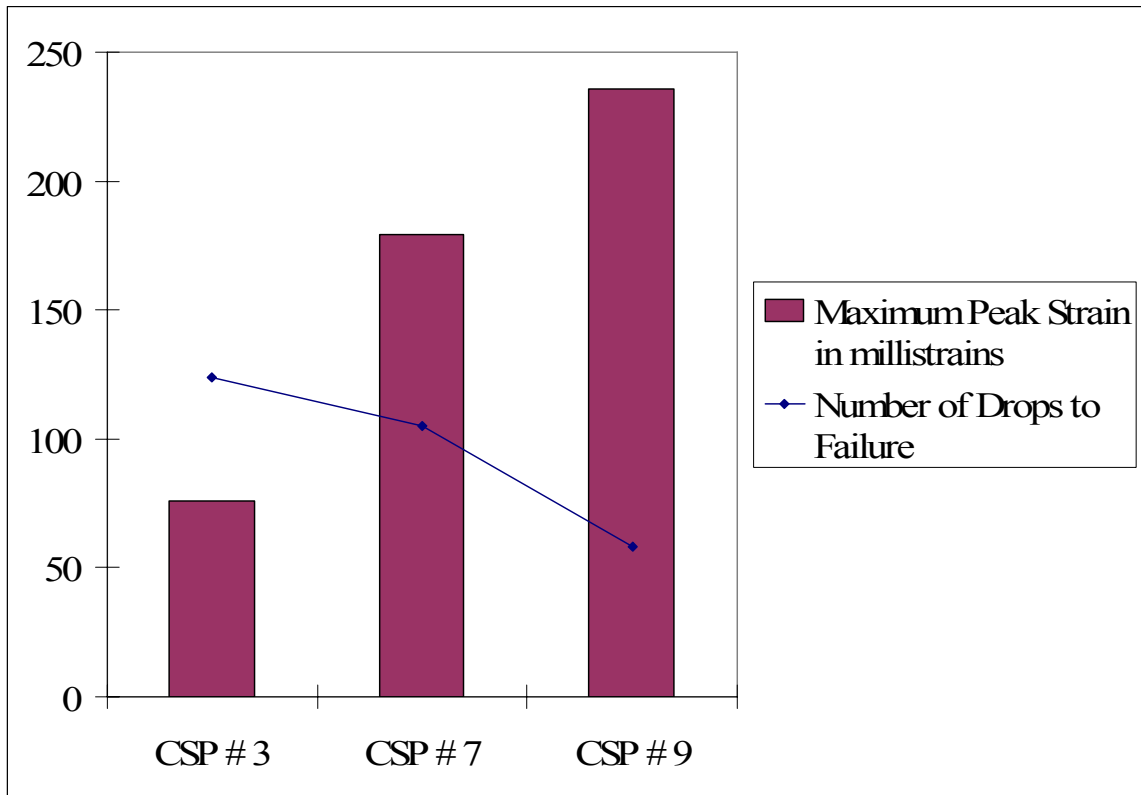


Figure 60 Number of drop to failure as a function of maximum peak strain in the cohesive element at different component locations for JEDEC Drop.

to be around 110-120 MPa [Darveaux et al. 2006] thus providing good correlation with the model predictions. Figure 60 shows the correlation between the magnitude of the peak transient strains in the cohesive elements obtained from simulation and the number of drops to failure at different component locations obtained experimentally by carrying out JEDEC drop. It can be seen that higher strains experienced by the cohesive elements located at the IMC layer of the corner solder joints at different component locations results in earlier failures of the packages due to solder interconnection fracture failure.

CHAPTER 6

SUMMARY AND CONCLUSIONS

In this research effort, the transient dynamic responses of the board level assemblies subject to drop impact have been investigated to enable the prediction of solder joint reliability under shock and vibration environments. Four explicit modeling techniques have been investigated for modeling shock loading of printed circuit board assemblies. The focus of the research effort was on modeling multiple scales from first-level interconnects to assembly-level transient dynamics. Modeling techniques investigated included smeared properties, Timoshenko-beam with Conventional Shell Elements, Timoshenko-Beam with Continuum Shell Elements, and Explicit Sub-modeling. This work extends the state-of-art, which presently focuses on prediction of interconnect stresses based on assumptions of symmetry of geometry and boundary conditions. In this research effort, modeling techniques have been developed to capture system-level dynamics in addition to interconnect transient-stress and transient-strain histories, without any assumption of assembly symmetry. The ability to eliminate symmetry assumptions enables the modeling of asymmetric modes in addition to symmetric modes. The model predictions have been correlated with experimental data from high-speed video, high-speed image analysis and high-speed strain acquisition. Model predictions shows excellent correlation with experimental data in terms of the

relative displacement and transient strain time histories. The various modeling methodologies employed resulted in increased computational efficiency while maintaining a good degree of accuracy. Model predictions also enabled the detection of the location and mode of failure of the critical solder interconnections most susceptible to failure when subject to drop impact.

Two failure prediction models namely the Timoshenko Beam Failure model and the Cohesive Zone Failure model have also been incorporated to predict the location and the mode of failures in the solder interconnections subject to drop impact respectively. The Timoshenko Beam Failure model predicts the location of the most critical solder interconnection susceptible to failure at the high strain rates experienced during drop. The Cohesive Zone failure model, on the other hand, shows the progressive degradation and failure of the cohesive elements located at the IMC layer leading to solder joint brittle interfacial failure. These predictions have shown very good correlation with the experimental drop tests and the observed failures modes observed by carrying out failure analysis.

BIBLIOGRAPHY

Abaqus Documentation, Dynamic Failure Models, Abaqus Analysis User's Manual, Version 6.6, Section 18.2.8, 2006a.

Abaqus Documentation, Cohesive Elements, Abaqus Analysis User's Manual, Version 6.6, Section 26.5, 2006b.

Abaqus Documentation, Finite Elements and Rigid Bodies, Getting Started with Abaqus Explicit: Keywords Version, Version 6.5, Section 4.1, 2005a.

Abaqus Documentation, Beam Element Overview, Abaqus Theory Manual, Version 6.5, Section 3.5.1, 2005b.

Abdul-Baqi, A., Schreurs, P. J. G., Geers, M. G. D., "Fatigue damage modeling in solder interconnects using a cohesive zone approach", International Journal of Solids and Structures, Volume 42, pp. 927-942, 2005.

Bansal, A., Yoon, S., Mahadev, V., “Flexural Strength of BGA Solder Joints with ENIG Substrate Finish using 4-Point Bend Test”, Proceedings of the SMTA Pan Pacific Microelectronics Symposium, pp. 1-8, 2005.

Carroll, D., Zampino, M., Jones, K., “Bending Simulation of BGA SMT Assemblies and Application to System Level Drop Simulation”, Proceedings of IPACK2005, pp. 1-9, 2005.

Chai, T. C., Quek, S., Hnin, W. Y., Wong, E. H., “Drop Level Drop Test Reliability of IC Packages”, Proceedings of the 55th Electronic Components and Technology Conference, pp. 630-636, 2005.

Chong, D. Y. R., Ng, K., Tan, J. Y. N., Low, P. T. H., “Drop Impact Reliability Testing for Lead-Free and Leaded Soldered IC Packages”, Proceedings of the 55th Electronic Components and Technology Conference, pp. 622-629, 2005.

Clech., J-P., “Solder Reliability Solutions: a PC-based Design-for-reliability Tool”, Proceedings of the Surface Mount International Conference, pp. 136-151, 1996.

Clech., J-P., “Flip-chip /CSP Assembly Reliability and Solder Volume Effects”,
Proceedings of the Surface Mount International Conference, pp. 315-324, 1998.

Date, M., Shoji, T., Fujiyoshi, M., Sato, K., Tu, K. N., “Impact Reliability of Solder
Joints”, Proceedings of the 54th Electronic Components and Technology
Conference, pp. 668-674, 2004.

Darveaux, R., Reichman, C., Islam, N., “Interface Failure in Lead Free Solder Joints”,
Electronic Components and Technology Conference, pp. 906-917, 2006.

Erich, R., Coyle, J. R., Wenger, G. M., Primavera, A., “Shear Testing and Failure
Mode Analysis for Evaluation of BGA Ball Attachment”, Proceedings of the
IEEE/CPMT International Electronics Manufacturing Technology Symposium,
pp. 16-22, 1999.

Ferracin, T., Landis, C. M., Delannay, F., Pardoën, T., “On the determination of the
cohesive zone properties of an adhesive layer from the analysis of the wedge-peel
test”, International Journal of Solids and Structures, Volume 40, pp. 2889-2904,
2003.

Harada, K., Baba, S., Wu, Q., Matsushima, H., Matsunaga, T., Uegai, Y., Kimura,
M., “Analysis of Solder Joint Fracture under Mechanical Bending Test”,
Electronic Components and Technology Conference, pp. 1731-1737, 2003.

Geng, P., “Dynamic Test and Modeling Methodology for BGA Solder Joint Shock Reliability Evaluation”, Proceedings of the 55th Electronic Components and Technology Conference, pp. 654-659, 2005.

Gu, J., Lim, C. T., Tay, A. A. Y., “Equivalent Solder Joint and Equivalent Layer Models for the Simulation of Solder Column Failure under Drop Impact”, Proceedings of the 6th Electronic Packaging Technology Conference, pp. 547-552, 2004.

Gu, J., Lim, C. T., Tay, A. A. Y., “Modeling of Solder Joint Failure due to PCB Bending during Drop Impact”, Proceedings of the 6th Electronic Packaging Technology Conference, pp. 678-683, 2004.

Gu, J., Lim, C. T., Tay, A. A. Y., “Simulation of Mechanical Response of Solder Joints under Drop Impact Using Equivalent Layer Models”, Proceedings of the 55th Electronic Components and Technology Conference, pp. 522-529, 2005.

Hanabe, M., Canumalla, S., “Package to Board Interconnection Shear Strength (PBISS) behavior at High Strain Rates Approaching Mechanical Drop”, Proceedings of the 54th Electronic Components and Technology Conference, pp. 1263-1270, 2004.

Hanabe, M., Canumalla, S., Kujala, A., “ Enhancing Drop Test Efficacy for Product Quality Improvement through Interconnection Shear Tests”, Proceedings of the 56th Electronic Components and Technology Conference, pp. 83-88, 2006.

Irving, S., Liu, Y., “Free Drop Test Simulation for Portable IC Package by Implicit Transient Dynamics FEM”, Proceedings of the 54th Electronic Components and Technology Conference, pp. 1062-1066, 2004.

JEDEC Standard IPC/JEDEC-9702, Monotonic Bend Characterization of Board-Level interconnects, 2004.

JEDEC Solid State Technology Association, Board-Level Drop Test Method of Components for Handheld Electronic Products, No. JESD22-B111, 2003.

Lall, P., Choudhary, P., Gupte, S., Suhling, J., “Health Monitoring for Damage Initiation & Progression during Mechanical Shock in Electronic Assemblies”, Proceedings of the 56th Electronic Components and Technology Conference, pp. 96-105, 2006.

Lall, P., Panchagade, D., Choudhary, P., Suhling, J., Gupte, S., “Failure-Envelope Approach to Modeling Shock and Vibration Survivability of Electronic and MEMS Packaging”, Proceedings of the 55th Electronic Components and Technology Conference, pp. 522-529, 2005.

- Lall, P., Panchagade, D., Liu, Y., Johnson, W., Suhling, J., “Models for Reliability Prediction of Fine-Pitch BGAs and CSPs in Shock and Drop Impact”, Proceedings of the 54th Electronic Components and Technology Conference, pp. 1296-1303, 2004.
- Lim, C. T., Ang, C. W., Tan, L. B., Seah, S. K. W., Wong, E.H., “Drop Impact survey of Electronic Products”, Proceedings of the 53rd Electronic Components and Technology Conference, pp. 113-120, 2003.
- Lim, C. T., Low, Y. J., “Investigating the Drop Impact of Portable Electronic Products”, Proceedings of the 52nd Electronic Components and Technology Conference, pp. 1270-1274, 2002.
- Luan, J., Tee, T. Y., “Novel Board Level Drop Test Simulation using Implicit Transient Analysis with Input-G Method”, Proceedings of the 6th Electronic Packaging Technology Conference, pp. 671-677, 2004.
- Marjakami, P., Mattila, T., Kivilahti, J., “Finite Element Analysis of Lead-Free Drop Test Boards”, Proceedings of the 55th Electronic Components and Technology Conference, pp. 462-466, 2005.

- Mishiro, K., Ishikawa, S., Abe, Mitsunori., Kumai, T., Higashiguchi, Y., Tsubone, K.,
“Effect of the drop impact on BGA/CSP package reliability”, Transactions on
Microelectronics Reliability, Vol. 42, pp. 77-82, 2002.
- Needleman, A., “A Continuum Model for Void Nucleation by Inclusion Debonding”,
Journal of Applied Mechanics, Volume 54, pp. 525-531, 1987.
- Needleman, A., “An analysis of decohesion along an imperfect interface”,
International Journal of Fracture, Volume 42, pp. 21-40, 1990.
- Newman, K., “BGA Brittle Fracture - Alternative Solder Joint Integrity Test
Methods”, Electronic Components and Technology Conference, pp. 1194-1201,
2005.
- Ong, Y. C., Shim, V.P.W., Chai, T.C., Lim, C.T., “Comparison of Mechanical
Response of PCBs Subjected to Product-Level and Board-Level Drop Impact
Tests”, Proceedings of the 5th Electronic Packaging Technology Conference, pp.
223-227, 2003.
- Ong, K. C., Tan, V. B. C., Lim, C. T., Wong, E. H., Zhang, X. W., “Dynamic
Materials Testing and Modeling of Solder Interconnects”, Proceedings of the 54th
Electronic Components and Technology Conference, pp. 1075-1079, 2005.

- Pang, J. H. L., Che, F. X., “ Drop Impact Analysis of Sn-Ag-Cu Solder Joints Using Dynamic High-Strain Rate Plastic Strain as the Impact Damage Driving Force”, Proceedings of the 56th Electronic Components and Technology Conference, pp. 49-54, 2006.
- Pang, J. H. L., Che, F. X., Low, T. H., “Vibration Fatigue Analysis For FCOB Solder Joints”, Proceedings of the 54th Electronic Components and Technology Conference, pp. 1055-1061, 2004.
- Pitarressi, J., Roggeman, B., Chaparala, S., “Mechanical Shock Testing and Modeling of PC Motherboards”, Proceedings of the 54th Electronic Components and Technology Conference, pp. 1047-1054, 2004.
- Ren, W., Wang, J., “Shell-Based Simplified Electronic Package Model Development and Its Application for Reliability Analysis”, Proceedings of the 5th Electronic Packaging Technology Conference, pp. 217-222, 2003.
- Ren, W., Wang, J., Reinikainen, T., “Application of ABAQUS/Explicit Submodeling Technique in Drop Simulation of System Assembly”, Proceedings of the 6th Electronic Packaging Technology Conference, pp. 541-546, 2004.
- Scheider, I., “Cohesive model for crack propagation analyses of structures with elastic–plastic material behavior”, GKSS research center, Geesthacht, 2001.

Schwalbe, K.-H., Cornec, A., “Modeling crack growth using local process zones”
Technical report, GKSS research centre, Geesthacht, 1994.

Shah, K. R., Mello M., “Ball Grid Array Solder Joint Failure Envelope Development for Dynamic Loading”, Proceedings of the 54th Electronic Components and Technology Conference, pp. 1067-1074, 2004.

Shetty, S., Reinikainen, T., “Three- and Four-Point Bend Testing for Electronic Packages”, Transactions of the ASME, pp. 556-561, 2003.

Syed, A., “Predicting Solder Joint Reliability for Thermal, Power, & Bend Cycle within 25% Accuracy”, Proceedings of the 51st Electronic Components and Technology Conference, pp. 522-529, 2001.

Syed, A., Kim, S. M., Lin, W., Khim, J. Y., Song, E. S., Shin, J. H., Panczak, T., “A Methodology for Dropp Performance Prediction and Application for Design Optimization of Chip Scale Packages”, Proceedings of the 55th Electronic Components and Technology Conference, pp. 472-479, 2005.

Tan, V. B. C., Tong, M. X., Lim, K. M., Lim, C. T., “Finite Element Modeling of Electronic Packages Subjected to Drop Impact”, IEEE Transactions on Components and Packaging Technologies, pp. 111-222, 2005.

- Tee, T. Y., Luan, J., Ng, H. S., “Development and Application of Innovational Drop Impact Modeling Techniques”, Proceedings of the 55th Electronic Components and Technology Conference, pp. 615-623, 2005.
- Tee, Y. T., Luan, J., Pek, E., Lim, C. T., Zhong, Z., “Advanced Experimental and Simulation Techniques for Analysis of Dynamic Responses during Drop Impact”, Proceedings of the 54th Electronic Components and Technology Conference, pp. 1088-1094, 2004.
- Tee, T. Y., Ng, H. S., Lim, C.T., Pek, E., “Drop Impact and Impact Life Prediction Model for QFN Packages”, Journal of SMT, Volume 16, Issue 3, pp. 31-39, 2003.
- Tee, T. Y., Luan, J., Pek, E., Lim, C. T., Zhong, Z, “Novel Numerical and Experimental Analysis of Dynamic Responses under Board Level Drop Test”, Proceedings of the 5th International Conference on Thermal and Mechanical Simulation and Experiments in Micro-electronics and Micro-Systems, pp. 133-140, 2004.
- Towashiraporn, P., Subbarayan, G., Desai, C. S., “A hybrid model for computationally efficient fatigue fracture simulations at microelectronic assembly interfaces”, International Journal of Solids and Structures, Volume 42, pp. 4468-4483, 2005.

- Towashiraporn, P., Xie, C., “Cohesive Modeling of Solder Interconnect Failure in Board Level Drop Test”, Proceedings of the IThERM, pp. 817-825, 2006.
- Tvergaard, V., Hutchinson, J.W., The relation between crack growth resistance and fracture process parameters in elastic-plastic solids, Journal of the Mechanics and Physics of Solids, Volume 40, pp. 1337–1397, 1992.
- Wang, Y.Q., Low, K.H., Che, F.X., Pang, H.L.J., Yeo, S.P., “Modeling and Simulation of Printed Circuit Board Drop Test”, Proceedings of the 5th Electronic Packaging Technology Conference, pp. 263-268, 2003.
- Wang, Y. Y., Wang, F., Chai, T. C., “Finite Element Modeling of CSP Package Subjected to Board Level Drop Test”, Proceedings of the 6th Electronic Packaging Technology Conference, pp. 684-688, 2004.
- Wong, E. H., Lim, C. T., Field, J. E., Tan, V. B. C., Shim, V. P. W., Lim, K. M., Seah, S. K. W., “Tackling the Drop Impact Reliability of Electronic Packaging”, Proceedings of IPACK05 International Electronic Packaging Technical Conference and Exhibition, pp. 1-7, 2005.
- Wong, E. H., Lim, K. M., Lee, N., Seah, S., Hoe, C., Wang, J., “Drop Impact Test – Mechanics & Physics of Failure”, Proceedings of the 4th Electronic Packaging Technology Conference, pp. 327-333, 2002.

Wong, E. H., Rajoo, R., Mai, Y. W., Seah, S. K. W., Tsai, K. T., Yap, L. M., “Drop Impact: Fundamentals & Impact Characteristics of Solder Joints”, Proceedings of the 55th Electronic Components and Technology Conference, pp. 1202-1209, 2005.

Wu, J., Song, G., Yeh, C., Wyatt, K., “Drop/Impact Simulation and Test Validation of Telecommunication Products”, Proceedings of the InterSociety Conference on Thermal Phenomena, pp. 330-336, 1998.

Xie, D., Arra, M., Yi, S., Rooney, D., “Solder Joint Behavior of Area Array Packages in Board Level Drop for Handheld Devices”, Proceedings of the 53rd Electronic Components and Technology Conference, pp. 130-135, 2003.

Yu, Q., Kikuchi, H., Ikeda, S., Shiratori, M., Kakino, M., Fujiwara N., “Dynamic Behavior of Electronics Package and Impact Reliability of BGA Solder Joints”, Proceedings of the Inter Society Conference on Thermal Phenomena, pp. 953-960, 2002.

Zahn, B. A., “Solder Joint Fatigue Life Model Methodology for 63Sn37Pb and 95.5Sn4Ag0.5Cu Materials”, Proceedings of the 53th Electronic Components and Technology Conference, pp. 83-94, 2003.

Zhao, J., Garner, L. J., “Mechanical Modeling and Analysis of Board Level Drop Test of Electronic Package”, Proceedings of the 56th Electronic Components and Technology Conference, pp. 547-553, 2006.

Zhu, L., “Modeling Technique for Reliability Assessment of Portable Electronic Product Subjected to Drop Impact Loads”, Proceedings of the 53rd Electronic Components and Technology Conference, pp. 100-104, 2003.

Zhu, L., Marcinkiewicz, W., “Drop Impact Reliability Analysis of CSP Packages at Board and Product System Levels Through Modeling Approaches”, Proceedings of the Inter Society Conference on Thermal Phenomena, pp. 296-303, 2004.

Zhu, J., Quander, S., Reinikainen, T., “Global/Local Modeling for PWB Mechanical Loading”, Proceedings of the 51st Electronic Components and Technology Conference, pp. 130-135, 2001.